Technische Universität Graz

Diploma Thesis

Friction Stir Welding of Multilayered Steel

accomplished at

Institute for Materials Science and Welding, TU Graz

and

Department of Materials Engineering, The University of Tokyo

written by

Johannes Tändl

supervised by

Assoc.-Prof. Dipl.-Ing. Dr.techn. Norbert Enzinger

and

Assoc.-Prof. Junya Inoue

and

Prof. Toshihiko Koseki

Preface

During the work on this project I was guided and supported by a number of people and institutions I would like to thank.

First of all I want to thank the director of the Institute for Materials Science and Welding (IWS) of Graz University of Technology, *Univ.-Prof. Dipl.-Ing. Dr.techn. Priv.-Doz. Christof Sommitsch*, for the opportunity to accomplish my thesis at his institute and for the financial support during my stay in Tokyo. In addition, I want to thank him for the great cooperation during my work as a student assistant over the last years.

In the same breath I want to thank the former head of IWS, *Em.Univ.-Prof. Dipl.-Ing. Dr.mont. Horst H. Cerjak*, for taking me aboard as a member of IWS. In particular, I want to thank him for setting the basis for my stay at The Univeristy of Tokyo by starting a cooperation with this insitution during his leadership.

Special thanks are directed to the whole team of IWS, especially to the supervisor of this thesis in Graz, *Assoc.-Prof. Dipl.-Ing. Dr.techn. Norbert Enzinger*, who entrusted me with a great and challenging task, and supported me in a not usually expected way.

I cordially want to thank my advisors *Prof. Toshihiko Koseki* and *Assoc.-Prof. Junya Inoue* of The University of Tokyo for their great help, financial support, and for the incredible experiences I was allowed to gain during my stay. Special thanks are directed to all members of Koseki/Inoue laboratory for accepting me as a member of the team and for including me in all activites.

The greatest thanks, however, are directed to my family and to my girlfriend Anna who supported me in every possible way during my years of study and my whole life. I wish once I will be able to repay all the trust I was given. Thank you for everything!

Johannes Tändl

Abstract

Laminated compound materials consisting of ductile austenitic steel and brittle martensitic steel are characterized by a combination of high strength and ductility which is unreachable with monolithic steels. These material properties are essential for the development of prospective lightweight, fuel-efficient, and crash-safe vehicles. As the modern production process in automotive industries consists of a number of different production steps, including various welding methods, proper weldability has become an indispensible material characteristic. In case of high strength/ductility multilayered steel, however, no successful welding has been reported so far.

This study investigates the mechanical properties and the microstructure of friction stir butt welded multilayered steel consisting of 15 alternating layers of SUS301 austenitic stainless steel (8 layers) and SUS420J2 martensitic stainless steel (7 layers) with a total thickness of 1.2mm. The mechanical properties of the welds were assessed using tensile testing and hardness testing, the microstructure evolution was analyzed with different microscopic techniques, including light optical microscopy (LOM), scanning electron microscopy (SEM), electron backscatter diffraction (EBSD), and transmission electron microscopy (TEM).

The multilayered material has an ultimate tensile strength (UTS) of 1370 MPa and a fracture elongation of 26 %, which results in an energy absorbtion capacity that equals about 5 times that of a DP 590 which is currently used for structural parts in vehicles. In this study, defect free welds were accomplished with optimized welding parameters leading to an UTS of 1240 MPa and a fracture elongation of 13 %. This corresponds to a joint efficiency of 90 %. In this case fracture occurred in the heat affected zone (HAZ) as a result of a very pronounced hardness drop in the martensitic layers resulting from the formation of a large amount of grain boundary precipitates. By applying a post weld heat treatment (PWHT) the hardness drop in the martensitic layers was removed and the tensile properties were enhanced to an UTS of 1310 MPa (95 % joint efficiency) and a fracture elongation of 22 %.

Contents

1 Introduction **1**

2 Definition of Task **2**

3 Literature Review **4**

3.1 Stainless Steels 4
3.1.1 Classification of Stainless Steels 4
3.1.2 Metallurgy of Stainless Steels 5
3.1.2.1 Iron-Chromium System 5
3.1.2.2 Iron-Chromium-Carbon System 5
3.1.2.3 Carbide Formation 7
3.1.2.4 Iron-Chromium-Nickel System 8
3.1.2.5 Schaeffler Diagram 10
3.1.3 SUS301 Austenitic Stainless Steel 10
3.1.3.1 Metallurgical Properties 10
3.1.3.2 Weldability 12
3.1.4 SUS420J2 Martensitic Stainless Steel 13
3.1.4.1 Metallurgical Properties 13
3.1.4.2 Weldability 15
3.2 Multilayered Materials 16
3.3 Friction Stir Welding Process 18
3.3.1 Weld Sections 19
3.3.1.1 Unaffected Parent Material 19
3.3.1.2 Heat Affected Zone 20
3.3.1.3 Thermomechanically Affected Zone 20
3.3.1.4 Stir Zone 20
3.3.2 FSW Parameters 20
3.3.2.1 Tool Rotation Speed and Welding Speed 21
3.3.2.2 Tilt Angle 22
3.3.2.3 Insertion Depth and Down Force 22

3.3.3 Friction Stir Welding Tools . . . 23
3.3.3.1 Tool Materials . . . 23
3.3.3.1.1 Tool Steel . . . 24
3.3.3.1.2 Refractory Materials . . . 24
3.3.3.1.3 Carbides and Metal-Matrix Composites . . . 24
3.3.3.1.4 Polycrystalline cubic boron nitride (pcBN) . . . 24
3.3.3.2 Tool Geometries . . . 24
3.3.3.2.1 Shoulder Geometry . . . 25
3.3.3.2.2 Probe Geometry . . . 26
3.3.4 Friction Stir Welding Applications . . . 28
3.3.4.1 Friction Stir Welding of Steel . . . 28

4 Experimental **31**
4.1 Multilayered Steel . . . 31
4.1.1 Production Process . . . 31
4.1.2 Microstructure . . . 32
4.1.3 Mechanical Properties . . . 35
4.2 Used Equipment . . . 36
4.2.1 Friction Stir Welding Machine . . . 36
4.2.2 Clamping . . . 36
4.2.3 FSW-Tool . . . 37
4.3 Experimental Procedure . . . 38
4.3.1 Temperature Measurement Setup . . . 41
4.3.2 Assessment of Mechanical Properties . . . 41
4.3.2.1 Tensile Testing . . . 41
4.3.2.2 Hardness Testing . . . 41
4.3.3 Metallurgical Investigations . . . 41
4.3.3.1 Light Optical Microscopy . . . 42
4.3.3.2 Scanning Electron Microscopy . . . 42
4.3.3.3 Electron Backscatter Diffraction . . . 43
4.3.3.4 Transmission Electron Microscopy . . . 43
4.3.4 Post Weld Heat Treatment . . . 43

5 Results and Discussion **45**
5.1 Feasibility Study and Process Optimization . . . 45
5.1.1 Eligibility of Different Backing Plates . . . 46
5.1.1.1 Oxide-Coated Steel Plate . . . 46
5.1.1.2 WC-Co Plate . . . 47
5.1.1.3 Nickel-Base Plate . . . 47

5.2 Temperature Measurement . . . 48
5.2.1 Influence of the Revolutionpitch on the Temperature Pattern . . . 48
5.2.2 Influence of the Down Force on the Temperature Pattern . . . 50
5.3 Mechanical Properties . . . 50
5.3.1 Tensile Properties . . . 50
5.3.1.1 Influence of the Revolutionpitch on the Tensile Properties 51
5.3.1.2 Influence of the Down Force on the Tensile Properties . 51
5.3.1.3 Range of Optimized Parameters . . . 53
5.3.2 Hardness Measurements . . . 56
5.4 Metallography . . . 59
5.4.1 Low Heat Input Welds . . . 59
5.4.2 High Heat Input Welds . . . 62
5.4.3 Optimized Parameters Welds . . . 66
5.4.3.1 Parent Material . . . 68
5.4.3.2 Heat Affected Zone . . . 69
5.4.3.3 Thermomechanically Affected Zone . . . 73
5.4.3.4 Stir Zone . . . 76
5.4.3.5 Fracture Behavior . . . 79
5.5 Post Weld Heat Treatment . . . 83
5.5.1 Mechanical Properties . . . 83
5.5.2 Fracture Behavior . . . 85
5.5.3 Metallography . . . 89

6 Summary **91**

7 Outlook **93**

List of Figures **95**

List of Tables **98**

Bibliography **99**

Appendix **104**

1 Introduction

As car manufacturers nowadays are faced with stricter and stricter, partially contradictory regulations concerning fuel consumption, CO_2 emission, and crash safety, they are forced to use advanced materials for structural parts and car body parts in order to comply with required standards and - not least - to satisfy the customer wishes for low running expenses, high safety standards and green technologies.

As a consequence, different approaches such as the combined use of steel and lightweight aluminum- and magnesium-alloys have been followed in the recent past in order to reduce weight. For high end sports cars even carbon-fiber reinforced plastics were used as a car body material by some premium manufacturers, even though this approach was considered as mainly aiming for performance improvement rather than for fuel saving. However, despite the recent progress in the given field many problems such as joinability of the different materials or complex design requirements due to different stiffnesses of the materials remained and kept the development costs high.

Most recently a very promising steel-based approach emerged that perfectly combines the possibilities of reduced fuel consumption and enhanced crash safety by avoiding design problems resulting from low stiffness. In this work, a multilayered material consisting of alternating layers of ductile austenitic steel and brittle martensitic steel was developed, which is characterized by the combination of high strength and ductility at a level which is just unreachable for monolithic materials. In other words, even at reduced wall thicknesses, and therewith reduced weight, this material is capable of absorbing more energy than any other material with comparable strength. Consequentially, a reduction in fuel consumption, CO_2 emission, and an improvement in crash safety could be reached by using the multilayered steel as a material for car components.

Unfortunately, despite all those advantages and despite the fact that this material is indeed considered as a possible solution to given problems, one big challenge remains: No successful welding of this special material has been reported so far.

2 Definition of Task

The main task of this study was the creation and analysis of friction stir welds of a modern multilayered steel consisting of 15 alternating layers of SUS301 austenitic stainless steel (8 layers) and SUS420J2 martensitic stainless steel (7 layers). Since no welding of this special high strength material, neither with conventional fusion methods nor with solid state friction welding, has been reported so far, a general feasibility study as well as fundamental investigations had to be performed. Based on the gained knowledge on a fundamental level it was aimed for a better understanding of the behavior of the material by conducting detailed investigations. The final task certainly was the determination of a systematic connection between the mechanical properties, the metallographic behavior, and the welding parameters.

Since this study was an outcome of a cooperation between the Institute for Materials Science and Welding of Graz University of Technology and the Department of Materials Engineering of The University of Tokyo, it was aimed for a targeted use of synergies by focusing on the strengths of both cooperation partners. Accordingly, the work was carried out at both locations, whereas welding and basic investigations were performed in Graz and detailed investigations were accomplished in Tokyo, in the laboratory of the inventors of the multilayered steel. Figure 2.1 illustrates the sub-tasks and their temporal sequence. As demonstrated, the majority of the work focused on friction stir welding in butt configuration, while only a small portion of time was used to investigate overlap welding. Accordingly, this study mainly deals with the results of butt welding, whereas the outcome of the overlap welding experiments will only be mentioned in the appendix of this thesis. Detailed results concerning overlap welding will be presented elsewhere.

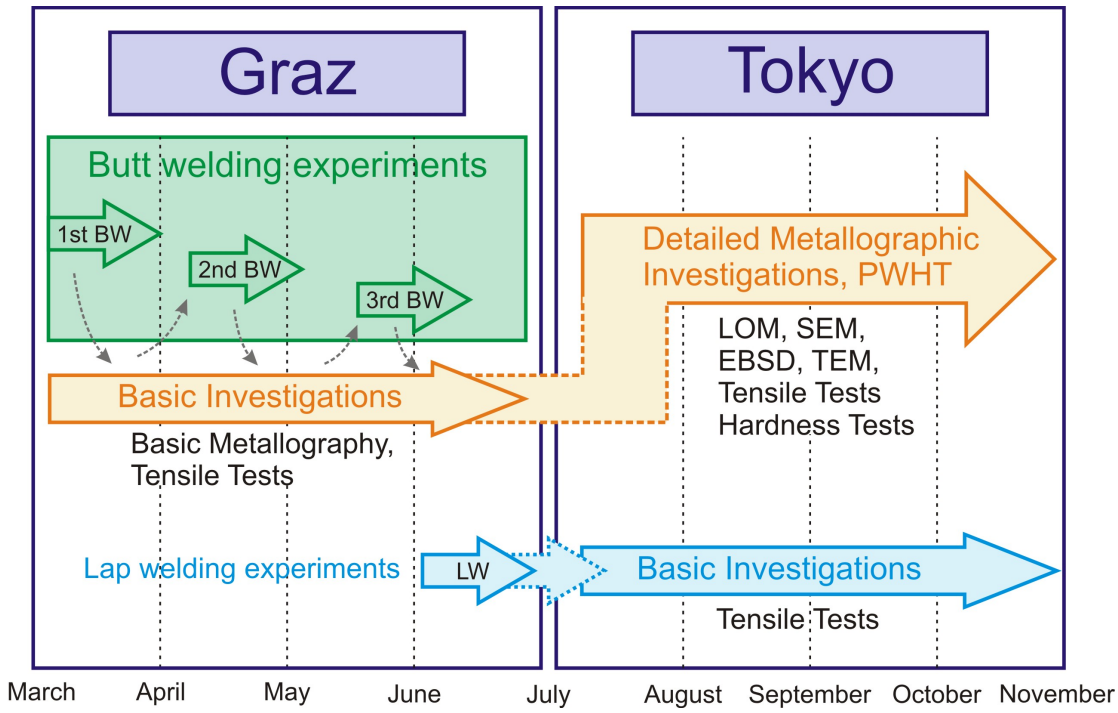

Figure 2.1: Timeline of action: March - November 2011

Tasks in Graz

- Friction stir butt welding feasibility study and process optimization
- Basic light optical microscopy, general assessment of the weld quality
- Basic investigations on the mechanical properties
- Optimization of the FSW parameters
- Accomplishment of welds in overlap configuration

Tasks in Tokyo

- Implementation and evaluation of a post weld heat treatment
- Investigation of the fracture behavior of the tensile test samples
- Detailed evaluation of the mechanical properties
- Detailed metallographic investigations using various methods
- Assessment of the basic mechanical properties of the overlap joints

3 Literature Review

3.1 Stainless Steels

Stainless steels form an important group within the large family of steels. Due to the combination of excellent corrosion resistance with a wide range of strength levels including strength retention at elevated temperatures, the use of those steels has tremendously increased over the last years. Today the range of applications reaches from simple kitchen ware to critical piping components in boiling water nuclear reactors.[1]

From a metallurgical point of view stainless steels can be defined as iron-base alloys that contain a minimum of approximately 11 % Cr in order to prevent the formation of rust in normal atmosphere. These stainless characteristics are achieved through the formation of an invisible passive chromium-rich oxide film on the surface.[1,2]

3.1.1 Classification of Stainless Steels

According to the American Welding Society (AWS) [2] stainless steels are classified in five categories:

1. Austenitic type with a face-centered cubic (fcc) structure
2. Ferritic type with a body-centered cubic (bcc) structure
3. Martensitic type with a body-centered tetragonal (bct) structure
4. Duplex alloys containing two of the upper mentioned structures
5. Precipitation-hardening (PH) alloys

In short, the classification is based on the crystal structure at room temperature (1-4) and additionally on a possible precipitation hardening process (5). Since the crystal structure, and consequentially the mechanical properties strongly depend on the chemical composition of the material, it is important to understand the metallurgical effects of different alloying elements.

3.1.2 Metallurgy of Stainless Steels

The most important alloying elements in stainless steels are chromium, nickel, and carbon. Certainly, the presence of other elements such as manganese, silicon, and molybdenum can not be neglected, but in order to understand the basic mechanisms a detailed discussion of the most important elements is sufficient.[1] The influence of other elements on the microstructure will be presented at the end of this section.

3.1.2.1 Iron-Chromium System

Figure 3.1 shows a binary Fe-Cr equilibrium phase diagram. In the Fe-Cr system full solubility is given and solidification of all alloys occurs as ferritic structure (bcc). At rather low chromium concentrations a loop of austenite, often referred to as gamma loop, exists in the temperature range from $912°C$ to $1394°C$. Alloys with a Cr-content greater 12.7 % will be fully ferritic in solid state at any temperature, while alloys with a Cr-concentration below 12.7 % will exhibit a ferritic-austenitic-ferritic transformation during cooling. The resulting microstructure at room temperature in the latter case is known as α-ferrite, whereas in case of higher Cr-content the final microstructure is commonly referred to as δ-ferrite. In case of sufficiently rapid cooling of alloys with about 12 % Cr or less from the gamma loop, a martensitic transformation occurs. In contrast, due to the absence of a prior austenitization, a martensitic transformation is not possible for greater Cr-content resulting in a fully δ-ferritic microstructure for any cooling rate.[3]

At chromium levels around 45 %, the brittle intermetallic σ-phase with a composition near FeCr precipitates from ferrite below $830°C$. The formation of the unfavorable σ-phase normally results in loss of toughness and corrosion resistance because it removes Cr from the surrounding matrix.[2]

3.1.2.2 Iron-Chromium-Carbon System

The addition of carbon as a very strong austenite promoter significantly changes the appearance of the Fe-Cr system. By alloying C, the gamma loop is expanded in a way that austenite becomes stable at elevated temperatures at much higher Cr-concentrations than in the binary Fe-Cr system. This behavior is illustrated in Figure 3.2, where the influence of different C-contents on the size of the gamma loop is demonstrated. It can be noted, that even very small amounts of carbon dramatically extend the austenite phase field. Consequentially, at increased carbon contents, a martensitic transformation can occur for alloys with higher Cr-content, whereas the stability of δ-ferrite is shifted to rather high Cr-concentrations.[3]

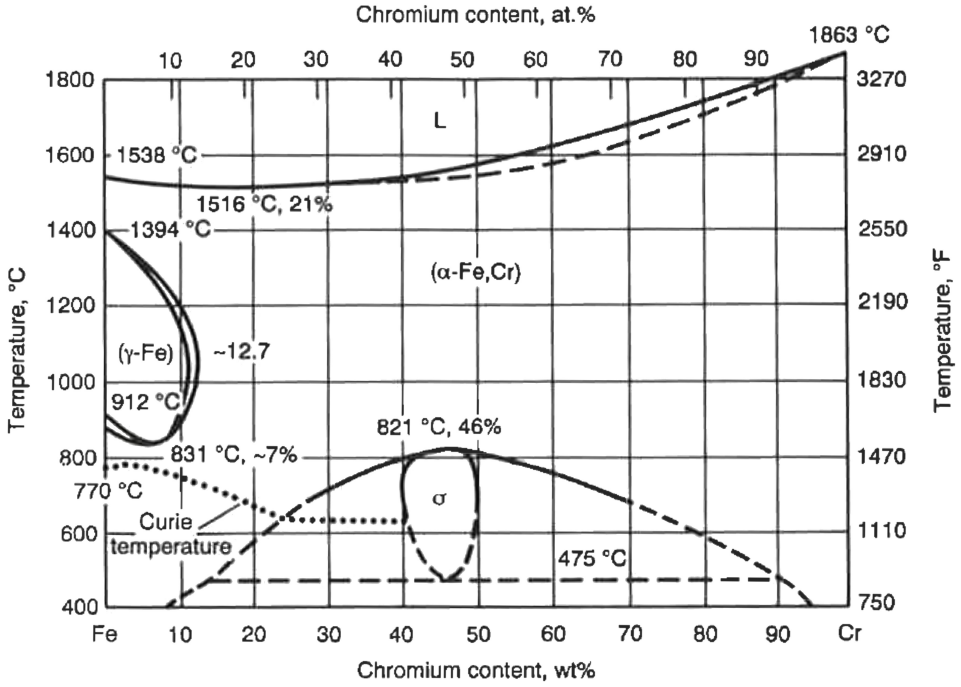

Figure 3.1: Iron-chromium equilibrium phase diagram [1]

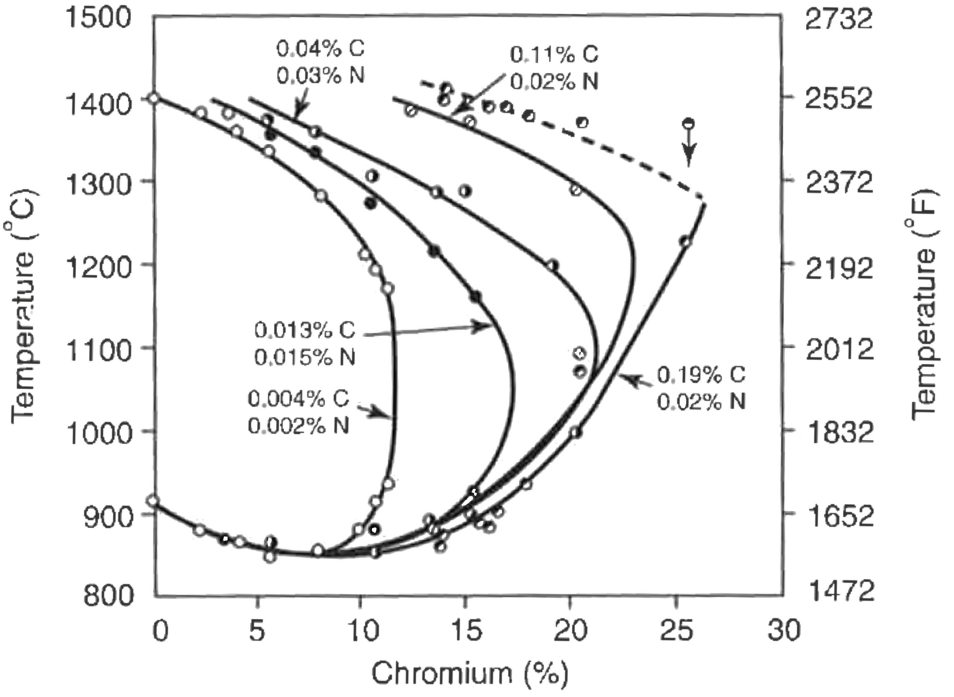

Figure 3.2: Influence of carbon on the expansion of the gamma loop [3]

3.1.2.3 Carbide Formation

Beside the expansion of the gamma loop, another effect occurs when alloying carbon to the Fe-Cr system. Precipitations of mixed Fe-Cr carbides are formed when the solubility limit for carbon in the matrix is exceeded: M_3C, $M_{23}C_6$, and M_7C_3, where M represents a mixture of metal atoms. Figure 3.3 shows two Fe-Cr phase diagrams at constant C-concentrations of 0.05 % (a) and 0.4 % (b). Apparently, with increasing carbon content the gamma loop is expanded and the diagram gets in general more complex. However, there is one important similarity, that is, at Cr-contents greater 10 % only face-centered cubic $M_{23}C_6$ is stable at room temperature and therefore is the most common carbide in many stainless steels. Depending on the overall chemical composition of the alloy, the formation of large amounts of those precipitates can significantly affect the corrosion behavior by depleting considerable amounts of Cr from the matrix. A loss in local corrosion resistance due to Cr-depletion is commonly referred to as sensitization.[2,4]

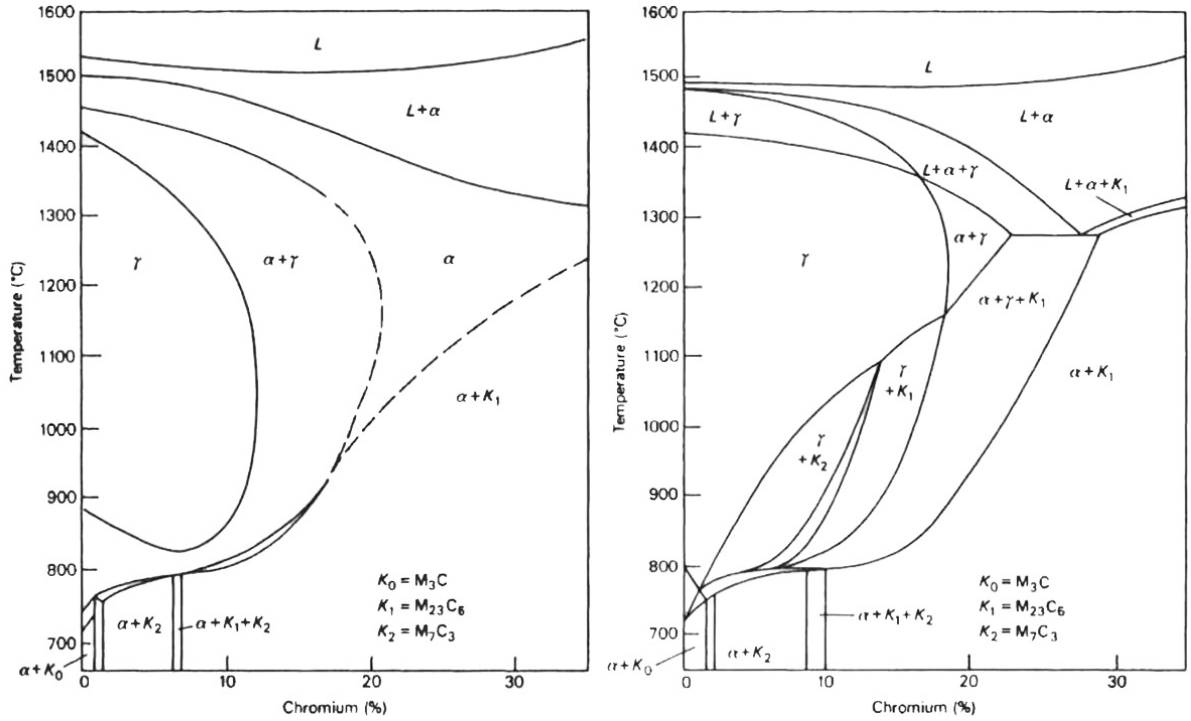

(a) 0.05 % C (b) 0.4 % C

Figure 3.3: Carbide formation in Fe-Cr system at constant C content [4]

3.1.2.4 Iron-Chromium-Nickel System

Addition of nickel to the Fe-Cr system expands the austenite phase field to higher Cr-concentrations and lower temperatures. The influence of different nickel contents on the size and shape of the gamma loop is demonstrated in Figure 3.4. With 6 % Ni, the gamma loop extends to 22 % Cr and the $\gamma \rightarrow \alpha$ transformation drops to $700°C$. With even greater Ni-content it is possible to expand the field of stable austenite down to room temperature, thus setting the metallurgical basis for austenitic stainless steels. Furthermore, as illustrated in the pseudobinary section of the Fe-Cr-Ni ternary system in Figure 3.5, a specific balance between Cr and Ni at a constant Fe-concentration will lead to the formation of austenite and ferrite, thus setting the basis for the production of $\delta + \gamma$ duplex stainless steels.[2,3]

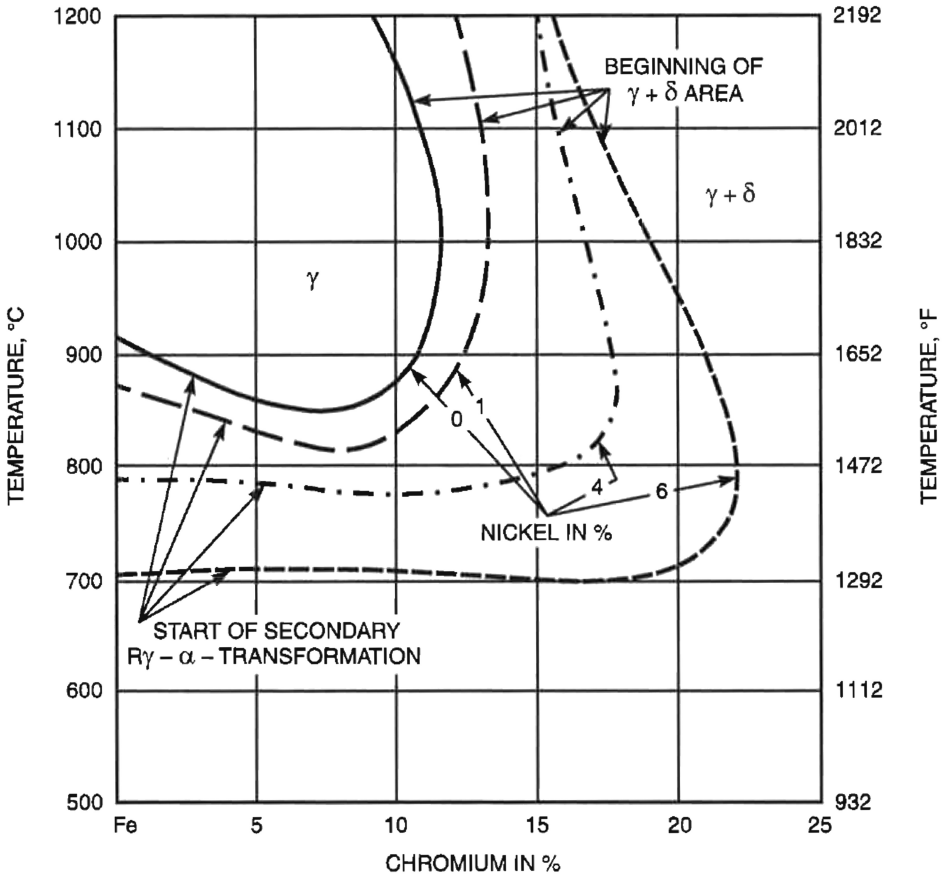

Figure 3.4: Influence of nickel on the expansion of the gamma loop [2]

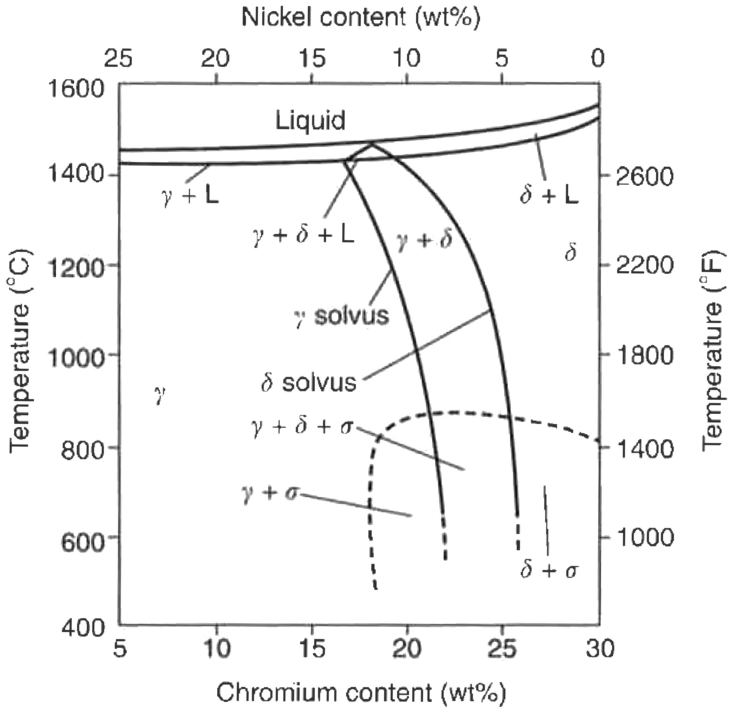

Figure 3.5: Pseudobinary section of the Fe-Cr-Ni system at 70 % Fe [3]

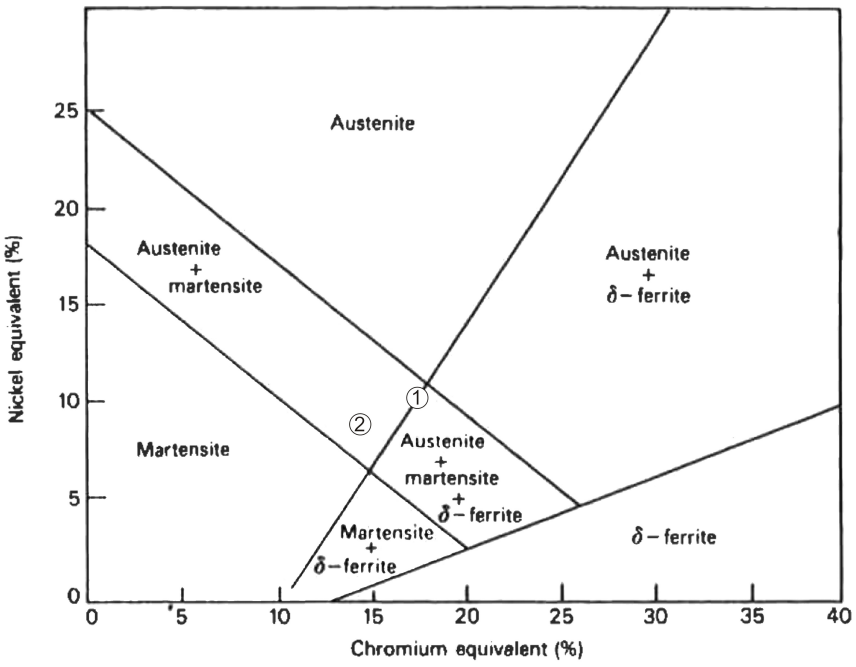

Figure 3.6: Schaeffler diagram.[4] ① SUS301, ② SUS420J2

3.1.2.5 Schaeffler Diagram

As already mentioned in the beginning of this section Cr, Ni, and C are the most important alloying elements for stainless steels because they are the strongest ferrite (Cr) or austenite (Ni, C) promoters. However, due to the complex chemical composition of many stainless steels the influence of other elements can not be neglected.

One of the most convenient ways of representing the effect of various elements on the microstructure of stainless steels is the Schaeffler diagram. It combines the influence of ferrite promoters in the chromium equivalent (Equation 3.1) and the effect of austenite promoters in the nickel equivalent (Equation 3.2) by empirical equations. As illustrated in Figure 3.6, the Schaeffler diagram plots the compositional limits at room temperature of austenite, ferrite and martensite, and thus giving a strong tool to estimate the solidification microstructure of stainless steels.[4] The positions of two specific stainless steel grades, austenitic SUS301 and martensitic SUS420J2, are demonstrated in the diagram.

$$Cr_{equ} = Cr + 2Si + 1.5Mo + 5V + 5.5Al + 1.75Nb + 1.5Ti + 0.75W \tag{3.1}$$

$$Ni_{equ} = Ni + Co + 0.5Mn + 0.3Cu + 25N + 30C \tag{3.2}$$

3.1.3 SUS301 Austenitic Stainless Steel

The steel grade SUS301 is a member of the group of 18Cr-8Ni austenitic stainless steels. According to Key to Steel database the SUS301 standard corresponds quite exactly to material number 1.4310 or DIN EN X10CrNi18-8, more precisely the former DIN EN X12CrNi17-7. In Table 3.1 the standard chemical composition (mass%) of SUS301 is demonstrated. In summary, the major alloying elements beside Fe are a maximum of 0.15 % carbon, 16 to 18 % chromium and 6 to 8 % nickel.[5]

3.1.3.1 Metallurgical Properties

Figure 3.7 shows a pseudobinary phase diagram for an Fe-18Cr-8Ni alloy with varying carbon content. At C-contents below 0.03 % the equilibrium microstructure contains ferrite and $M_{23}C_6$ carbide at room temperature. In alloys containing between 0.03 and 0.7 % C, the equilibrium structure should contain austenite, ferrite, and $M_{23}C_6$ carbide.

	C	Si	Mn	P	S	Cr	Ni
min	-	-	-	-	-	16.00	6.00
max	0.15	1.00	2.00	0.045	0.030	18.00	8.00

Table 3.1: Standard chemical composition of SUS301 [5]

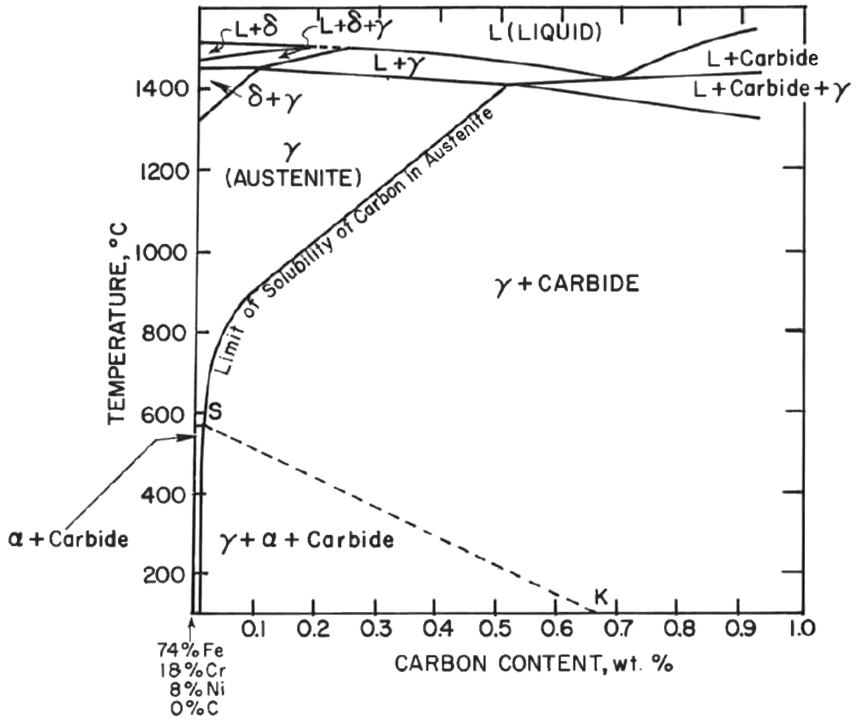

Figure 3.7: Pseudobinary phase diagram. Fe-18Cr-8Ni alloy with varying C-content [6]

However, in commercial alloys such as SUS301, the reaction $\gamma+M_{23}C_6 \rightarrow \gamma+\alpha+M_{23}C_6$ is too sluggish to take place at practical cooling rates resulting in a ferrite-free microstructure at ambient temperature. During relatively rapid cooling also the precipitation of carbides is partially suppressed, leading to a supersaturated austenite. If this supersaturated austenite is reheated to temperatures within the $\gamma + M_{23}C_6$ field, further precipitation of $M_{23}C_6$ will occur at the austenite grain boundaries. As a consequence of an excessive formation of Cr-rich carbides due to slow cooling or heat treatment, sensitization may occur.[6]

Similar to other austenitic stainless steels, the SUS301 can be hardened by cold working but not by heat treatment, is nonmagnetic in annealed condition, and has good corrosion resistance and formability. Due to the relatively low Ni-content compared to other austenitic stainless steel grades, SUS301 exhibits increased work hardening on deformation than other types, resulting in greater yield and ultimate tensile strength.[7]

In contrast to stable austenites, in which the martensite start temperature M_s is clearly lower than room temperature, for low-carbon 18Cr-8Ni austenitic steels M_s is just below room temperature. Therefore, alloys such as SUS301 will transform to martensite by cooling in liquid nitrogen or similar refrigeration. Austenitic steels that show this kind of behavior are commonly known as metastable austenites.[4]

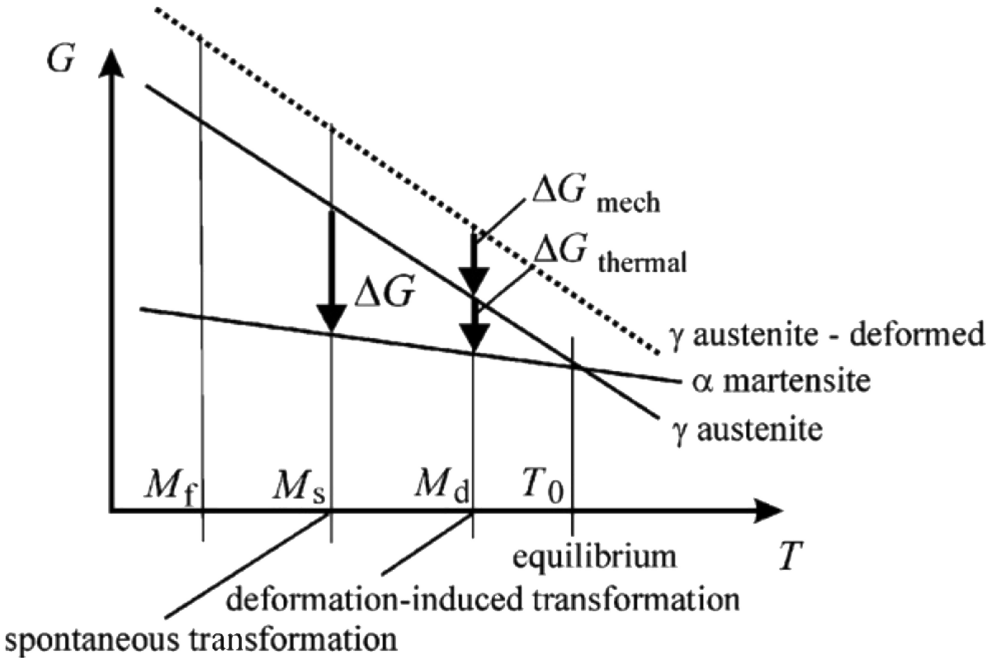

Figure 3.8: Influence of deformation on the austenite-to-martensite transformation [8]

Beside from rapid cooling below room temperature, also the application of plastic deformation at room temperature may lead to the formation of martensite in metastable austenites. Figure 3.8 demonstrates the contribution of mechanical deformation energy ΔG_{mech} to the driving force for austenite-to-martensite transformation. The critical free energy change ΔG for spontaneous transformation at M_s can be reached already at higher temperatures by the deformation energy contribution ΔG_{mech} adding to the thermal energy contribution ΔG_{therm}. As a consequence, the martensitic transformation for a certain deformation already occurs at a higher temperature M_d.[8]

3.1.3.2 Weldability

Amongst all types of stainless steels the austenitic grades are the most weldable. The most commonly used welding processes are shield metal arc welding (SMAW) and gas tungsten arc welding (GTAW). Preheating is not required and also post-heating is only necessary in case of precipitates that may have formed at elevated temperatures during the welding process need to be redissolved. However, some problems may arise during welding if proper precautions are not taken. For example, due to the higher coefficient of expansion compared to carbon steels, the heat input should be minimized to reduce thermal contraction and distortion. Furthermore, lower heat input results in faster cooling rates that help to overcome the problem of sensitization, and as a consequence, the problem of intergranular corrosion and stress-corrosion cracking.[7,9]

The most serious problems associated with welding of austenitic stainless steels, besides a possible reduction in corrosion resistance, are weld solidification cracking and liquation cracking. Weld solidification cracking is mainly a function of composition where fully austenitic structures, such as SUS301, tend to be the most susceptible to defects. The general theory of solidification cracking is that solidified grains covered by thin liquid films are ruptured at elevated temperatures by tensile stresses arising from thermal contraction. Liquation cracking can occur either in the weld metal in case of multipass welding or in the partially melted zone within HAZ. Similar to solidification cracking, liquation cracking occurs due to formation of liquid films from low melting phases along grain boundaries.[3,10]

3.1.4 SUS420J2 Martensitic Stainless Steel

The steel grade SUS420J2 is a martensitic stainless steel. The standard SUS420J2 refers to material number 1.4028 or to the standard X30Cr13, respectively. In Table 3.2 the standard chemical composition (mass%) of SUS420J2 is demonstrated. According to that, the major alloying elements beside Fe are 0.26 to 0.40 % C and 12 to 14 % Cr.[5]

3.1.4.1 Metallurgical Properties

Figure 3.9 shows a pseudobinary phase diagram of an alloy consisting of Fe and 13 % Cr at varying C-contents. At very low C-contents the alloys are fully ferritic at elevated temperatures. If cooled rapidly enough, those alloys will remain primarily ferritic, thus setting the metallurgical basis for low-chromium ferritic steels. At C-contents above 0.1 %, austenite will form at elevated temperatures over a large range of C-contents. During cooling of a 0.3 % C alloy for example, the austenite phase is stable in a temperature range from around 1350 to 1050°C. Below 1050°C, $M_{23}C_6$ carbides (C_1) will precipitate from the austenite and subsequently, at around 800°C, the austenite will transfrom into ferrite. Consequentially, the equilibrium microstructure at room temperature of an alloy of 13 % Cr and 0.3 % C contains ferrite and $M_{23}C_6$ carbides.[3]

In Figure 3.10 a continuous cooling transformation (CCT) diagram of a 13 % Cr martensitic stainless steel with a chemical composition very similar to SUS420J2 is given. As illustrated, the austenite will transform into martensite during cooling at virtually any practical cooling rate. Similar to most other martensitic stainless steels, SUS420J2

	C	Si	Mn	P	S	Cr	Ni
min	0.26	-	-	-	-	12.00	-
max	0.40	1.00	1.00	0.040	0.030	14.00	0.60

Table 3.2: Standard chemical composition of SUS420J2 [5]

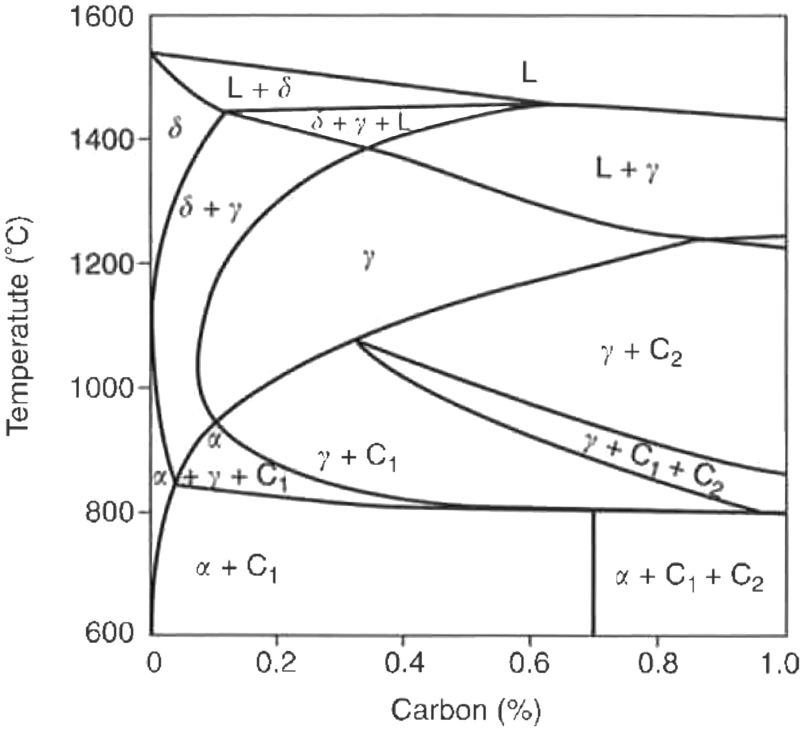

Figure 3.9: Pseudobinary phase diagram. Fe-13Cr alloy with varying C-content [3]

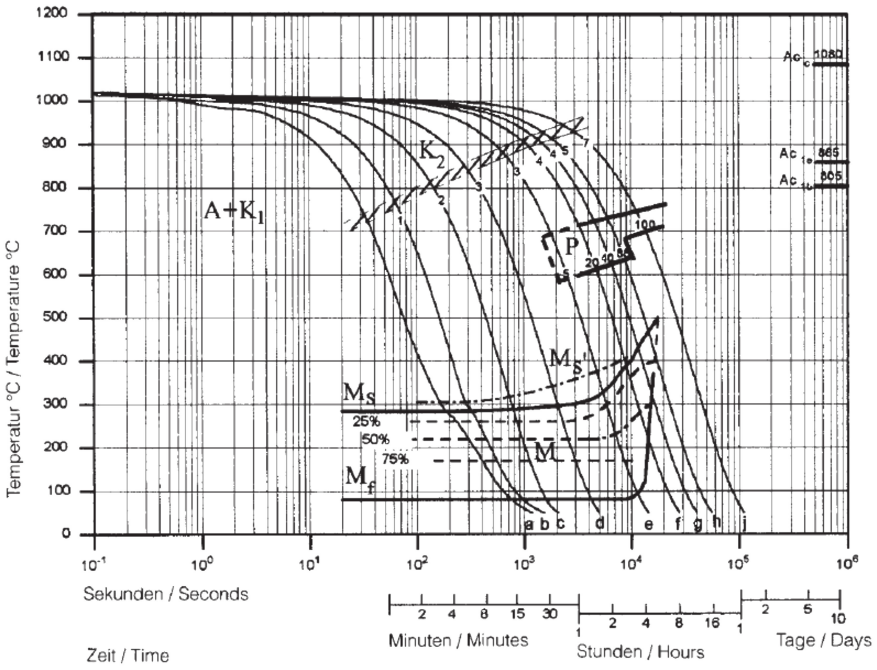

K_1...Carbides not dissolved during austenitization
K_2...Start of carbide precipitation during cooling

Figure 3.10: CCT diagram for an Fe-13Cr alloy with 0.35 % C [11]

therefore is termed *air hardening*, as cooling in still air is sufficiently rapid to produce martensite. Martensite start temperature M_s is around $300°C$, and martensite finish temperature M_f is clearly above room temperature, at around $100°C$.[3,11]

Similar to other martensitic stainless steels, SUS420J2 is magnetic and, due to the comparably low Cr-content, less corrosion resistant than most other stainless steels. Due to the relatively high C-content of 0.3 %, the SUS420J2 grade has a very high hardness, resulting in a poor workability and machinability. As a consequence, this grade is normally supplied in hardened and tempered condition. In order to facilitate machining or cold working, many martensitic stainless steels are annealed at temperatures ranging from about 650 to $760°C$. Certainly, this heat treatment influences the microstructure by facilitating precipitation of equilibrium phases such as $M_{23}C_6$ and also ferrite from the martensitic microstructure. The amount of precipitation strongly depends on tempering time and temperature. Furthermore, tempering influences the corrosion behavior in a way that as-quenched microstructures typically have greater corrosion resistance compared to tempered alloys caused by the formation of Cr-rich carbides in the latter case.[1,2,7]

3.1.4.2 Weldability

Amongst all types of stainless steels the martensitic grades are generally considered the least weldable. While welding of martensitic grades with a C-content of about 0.06 % is relatively unproblematic, welding of types with 0.3 % C and more causes serious problems. The reason therefore is that in high carbon steels, very hard and brittle martensite occurs after welding, that is prone to hydrogen induced cracking or cold cracking. For those cracking mechanisms the presence of hydrogen, high tensile stresses (residual or applied), susceptible microstructure (brittle martensite), and relatively low temperature must be given at a time. If these factors can be controlled, cracking can be avoided. As a consequence, welding of grades such as SUS420J2 is only possible with special welding procedures.[3,10]

In order to realize defect-free welds, preheating and post weld heat treatment (PWHT) are indispensible. By preheating at a temperature of around 200 to $300°C$, the cooling rate after welding will be slower, leading to a less brittle martensitic microstructure and more time for hydrogen diffusion from the weld zone. A PWHT at around $260°C$ will temper the martensite in order to increase toughness and decrease residual stresses associated with welding. The hydrogen potential can be minimized by using inert-gas welding processes such as GTAW or GMAW as well as by drying and baking consumables.[1,7]

3.2 Multilayered Materials

Laminated composite materials consisting of alternating metal or metal containing layers dramatically improve many mechanical properties of the single constituents including fracture toughness, fatigue behavior, impact behavior, wear, corrosion, damping capacity, and even deformability.[12] In previous studies, laminated composites made of ultrahigh carbon steel and brass [13] as well as compounds made of ultrahigh carbon steel and mild steel [14] have been subject to different investigations. Recently, the microstructure and the mechanical properties of a lightweight multilayered compound material consisting of commercial 1060 Al and AZ31 magnesium alloy has been analyzed.[15] However, the present study focuses on investigations on laminated composites consisting of austenitic and martensitic steel.

Multilayered steel with enhanced deformation behavior and tensile properties consisting of alternating layers of ductile austenitic steel and brittle martensitic steel, similar to that shown in Figure 3.11, has been subject to various investigations.[16–20] Inoue *et al* [16] showed a transition of the fracture behavior of the martensitic layer from brittle cleavage to ductile shear just by reducing the layer thickness in a hot rolled laminate. In a different study, the elongation of as-quenched martensite under tensile loading was increased from 6 % in monolithic material to more than 50 % using a laminated composite consisting of conventional martensitic and austenitic steel.[17] Nambu *et al* [18] demonstrated tremendous improvement in tensile ductility by increasing the bonding strength in a brittle/ductile multilayered structure. Furthermore, detailed investigations concerning strain field computation [19] and microtexture development for different cold-rolling reductions [20] were carried out for a composite consisting of martensitic and austenitic layers.

Summarizing that, it can be deduced that the major advantage of compound materials consisting of layers of austenitic and martensitic steel over conventional steels is the combination of strength and ductility which is just unreachable with monolithic materials, as illustrated in Figure 3.12. The outstanding mechanical properties of those materials are in particular, but not exclusively, interesting for car manufacturers.

The use of a certain material as a structural material for car body parts or any other application usually requires a number of processing steps that have to be passed through including casting, stamping, forming, joining, machining and others.[21]

Amongst those processing steps one of the most important certainly is joining, or more precisely welding. In the case of multilayered steels, however, no successful welding has been reported so far.

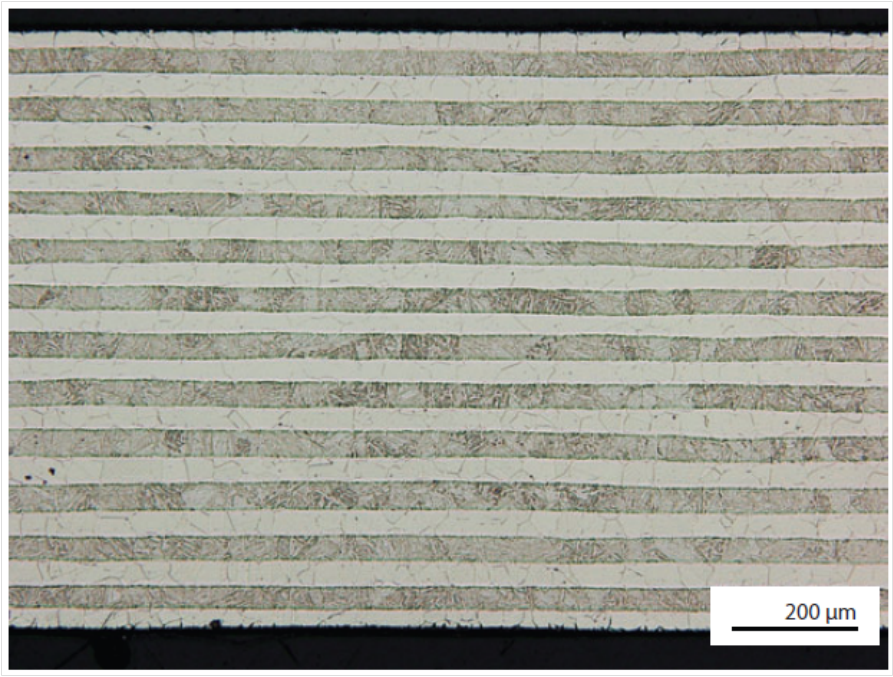

Figure 3.11: Multilayered steel composite [22]

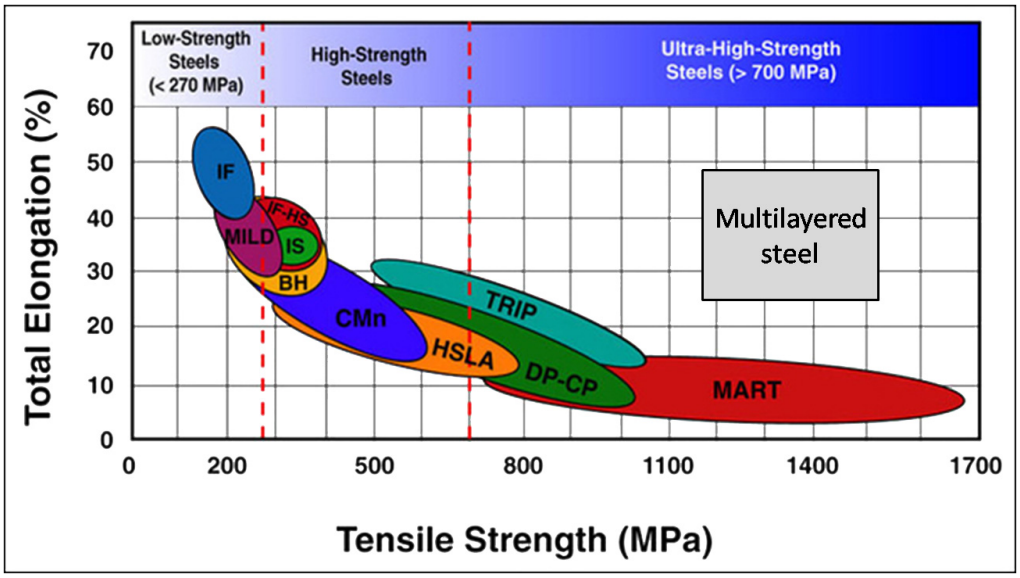

Figure 3.12: Overview of the mechanical properties of different steel types [23]

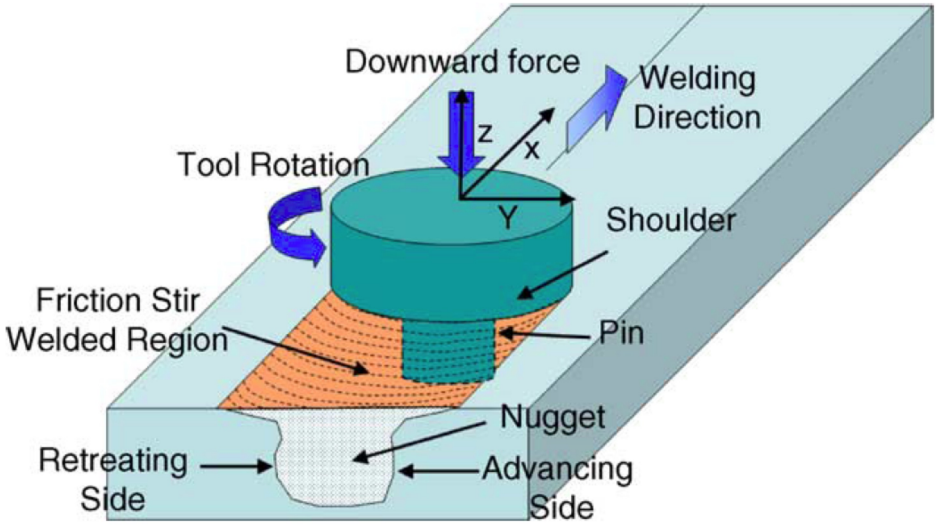

Figure 3.13: Schematic illustration of the FSW process [29]

3.3 Friction Stir Welding Process

Friction stir welding (FSW) is a solid state welding process invented at The Welding Institute (TWI) in Cambridge, GB in 1991.[24] The initial purpose of the innovation was the improvement of the weldability of several aluminum-alloys which were in general classified as non-weldable. Due to the success of the process for aluminum, today the applicability of FSW is investigated for a large variety of materials including copper, magnesium, titanium, steel, and even polymers.[25] Furthermore, it has turned out that FSW is especially suitable for dissimilar welding, as successful welding has been reported for various materials combinations including Al-Steel [26], Cu-Al [27], and Mg-Steel [28].

Figure 3.13 schematically illustrates the FSW process. The basic process concept provides a rotating tool with a specially designed probe (pin) and shoulder that is inserted in the abutting edges of plates to be joined and traversed along the joint line in order to heat up the material and generate a material flow to produce the joint. The heat is generated during the process by friction between the tool and workpiece and by plastic deformation in the workpiece.[29]

In contrast to most fusion welding processes, where the weld seam is in general symmetrical in relation to the weld center, in friction stir welding an asymmetrical weld seam emerges caused by the combination of a translational and rotatorial movement of the tool (Figure 3.13). In this context it is important to differentiate between the advancing side (AS), where the tool rotation direction is the same as the tool travel direction, and the retreating side (RS), where the tool rotation is opposite the tool travel direction.[30]

In short, unlike with conventional fusion welding methods, where the material is molten due to external heat input, the workpiece is plastified during FSW due to the interaction of the material and the rotationg tool. As a consequence, the joint is in general created in solid state, whereas only in special cases a low melting liquid phase may appear, as demonstrated by Schneider *et al.*[28] Selections of advantages and disadvantages of the FSW-process are listed below.

Advantages [30]

- Solid-phase process
- Low distortion
- Excellent mechanical properties in the joint area
- Fine recrystallized microstructure
- Absence of solidification cracking

Disadvantages [31]

- Firm and rigid clamping of the workpieces is necessary
- End of run hole can not be avoided
- Generally lower welding speed compared to other methods
- Tool wear for materials with high melting temperature

3.3.1 Weld Sections

In order to classify and describe the friction stir welded microstructure, four different microstructural zones are identified considering heat input and exposure to plastic deformation. Figure 3.14 shows a welded cross section and the different weld regions, that are *Unaffected Parent Material (A)*, *Heat Affected Zone (B)*, *Thermomechanically Affected Zone (C)*, and *Stir Zone* or *Nugget (D)*.[32]

3.3.1.1 Unaffected Parent Material

As the name implies, the material remote from the weld is unaffected by heat or deformation, hence the term *Unaffected Parent Material (PM)*. This weld region may experience a certain thermal cycle, yet any influence on microstructure or mechanical properties is hardly measurable.[30,32]

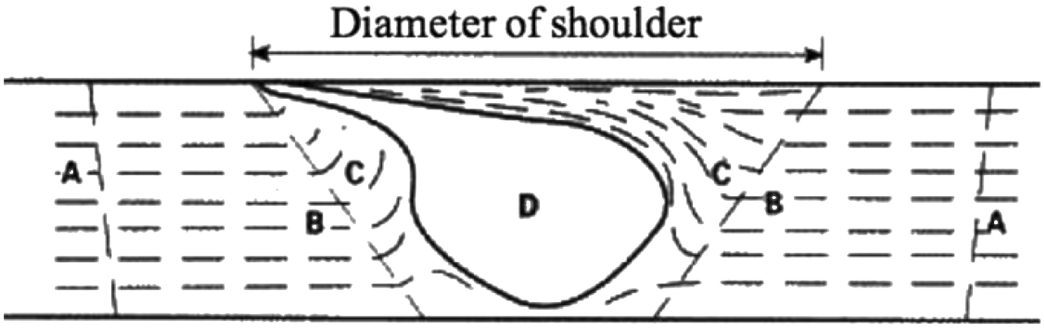

Figure 3.14: Microstructural regions in a friction stir weld [25]

3.3.1.2 Heat Affected Zone

The inner adjacent zone to *PM* is the *Heat Affected Zone (HAZ)*. In this region the material experiences a thermal cycle that modifies the microstructure and the mechanical properties. No plastic deformation occurs in this area.[30,32]

3.3.1.3 Thermomechanically Affected Zone

In contrast to *PM* and *HAZ*, the microstructure in the *Thermomechanically Affected Zone (TMAZ)* is strongly influenced by plastic deformation and elevated temperature. The width of this zone usually corresponds with the width of the tool shoulder on the upper surface, and the probe diameter at the root. In some materials this region may not be completely recrystallized.[30,32]

3.3.1.4 Stir Zone

The *Stir Zone (SZ)* experiences the highest degree of plastic deformation and the highest process temperatures occur. This fully recrystallized zone, sometimes called *Weld Nugget* or *Dynamically Recrystallized Zone*, refers to the zone previously occupied by the tool probe.[30,32]

3.3.2 FSW Parameters

The most influential parameters for FSW are *Tool Rotation Speed* $\omega\,[rpm]$, *Welding Speed* $v\,[mm\,min^{-1}]$, *Tilt Angle* $\alpha\,[°]$, and *Insertion Depth* or *Down Force* $F\,[kN]$. The parameters are illustrated in Figure 3.15. In order to create sound welds, it is indispensible to coordinate all four parameters in the most suitable way.[29]

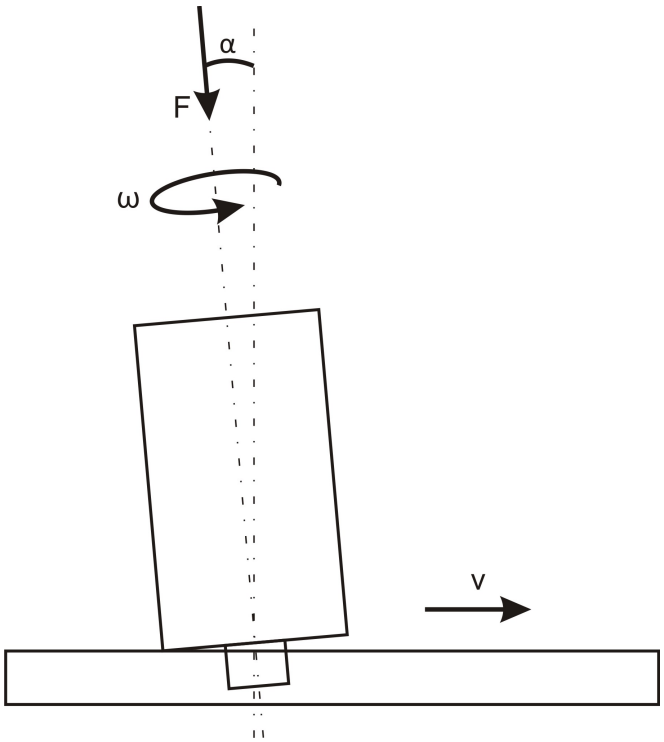

Figure 3.15: Sketch of the most important welding parameters

3.3.2.1 Tool Rotation Speed and Welding Speed

Amongst the four main parameters, the most important ones are tool rotation speed and welding speed. Due to the rotation of the tool, material is stirred and mixed around the probe and heat is generated by friction between the tool shoulder and the workpiece. Accordingly, higher tool rotation speed at constant welding speed generates more intense stirring and higher temperatures because of higher friction heating. The translation of the tool moves the stirred material from the front to the back of the probe.[25,29]

It has been reported [33] that the heat input is related to the revolutionpitch $[mm\,rev^{-1}]$ and thereby on the ratio of welding speed and tool rotation speed, as demonstrated in Equation 3.3. In other words, the revolutionpitch denotes the number of millimeters that the tool proceeds in welding direction during one revolution. Consequentially it can be noted, that the lower the revolutionpitch, the higher the heat input.

$$revolutionpitch\left[\frac{mm}{rev}\right] = \frac{welding\,speed\,\left[\frac{mm}{min}\right]}{tool\,rotation\,speed\,\left[\frac{rev}{min}\right]} \tag{3.3}$$

The analysis of the influence of the revolutionpitch has been subject to different investigations.[33,34] Matsushita *et al* [33] clarified the welding condition range for high strength

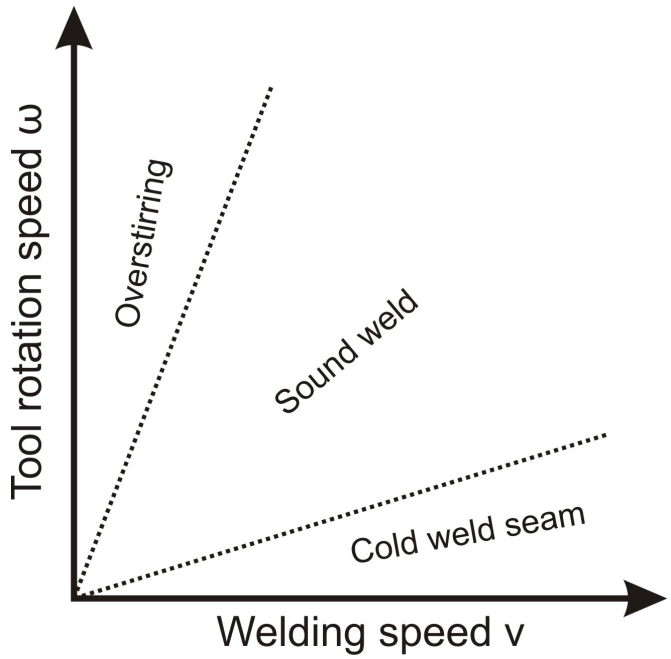

Figure 3.16: Weld quality as a function of the revolutionpitch [34]

steel sheets, Dubourg *et al* [34] summarized the effect of different revolutionpitches on the properties of Al-alloy friction stir welds. The outcome of the latter investigation is illustrated in Figure 3.16. With low revolutionpitches overstirring occurs, which can lead to the formation of two nuggets or, in extreme conditions, to the formation of wormholes on top of the weld seam. In case of too high revolutionpitches on the other hand, wormhole type defects occur at the weld bottom. In between those boundaries sound welds can be produced.

3.3.2.2 Tilt Angle

The tilt angle describes an inclination of the vertical axis, as shown in Figure 3.15. A suitable tilt of the spindle towards trailing direction ensures that the shoulder of the tool holds the stirred material in the proper position.[29]

According to different studies, tilt angles in a range from 1 to 3° are suitable for friction stir welding of steel.[33,35,36]

3.3.2.3 Insertion Depth and Down Force

The insertion depth is associated with the probe height. When the insertion depth is too shallow, the shoulder of the tool does not contact the workpiece surface resulting in unsatisfactory heat input and material movement. When the insertion depth is too

deep, the shoulder penetrates the workpiece, leading to the formation of excessive flash. In both cases, the outcome of the weld will be unfavorable.[29]

Most modern friction stir welding machines provide two different possibilites to control the insertion depth. One is displacement control, the other is force control. The former sets a constant vertical position of the tool, the latter one sets a constant vertical force. In previous investigations on friction stir welding of steel the insertion depth, and thereby the friction between shoulder and workpiece, was force controlled with a vertical force ranging from 9 to $31kN$ depending on tool geometry and material.[35,37,38]

3.3.3 Friction Stir Welding Tools

Friction stir welding is not possible without a FSW-tool, as it produces the thermo-mechanical deformation and workpiece frictional heating associated with the process. Consequentially, the tool is a critical component to the success of the process. For initial FSW-studies on aluminum, a cylindrical threaded pin and a concave shoulder made from tool steel were used. Since that time, FSW was applied to significantly harder materials such as steels and titanium alloys, which caused a tremendous increase of thermal and mechanical loads on the tool. As a consequence, complex tools made from exotic materials have been developed that are able to withstand severe stresses and high temperatures.[39,40]

3.3.3.1 Tool Materials

Friction stir welding tools have to fulfill a number of criteria concerning physical properties and also practical considerations. Some of the most important are listet below.[39]

- Ambient and elevated temperature strength
- Elevated temperature stability
- Wear resistance
- Low tool reactivity
- Fracture toughness
- Availability of materials
- Machinability

3.3.3.1.1 Tool Steel

Tool steel is the most common tool material used in friction stir welding because of its suitability for materials with relatively low melting temperature such as aluminum and magnesium alloys. Some advantages compared to other tool materials are obvious, such as easy availability and machinability, low costs, and established material characteristics. Often air-hardening, hot or cold worked high-carbon chromium-molybdenum steels are used because they are known for good elevated-temperature strength, thermal fatigue resistance, and wear resistance. Depending on the composition the maximum-use temperature for tool steels ranges from 500 to 600°C.[39,40]

3.3.3.1.2 Refractory Materials

Refractory metals including tungsten (W), molybdenum (Mo), niobium (Nb), and tantalum (Ta), are used for their high-temperature capabilities and high densities. As a single phase, their strength is maintained to nearly the melting-point temperature, which makes them part of the strongest alloys between 1000 and 1500°C. The huge disadvantages are limited material availability, high costs, and difficult machining. The primary production method is powder processing. Amongst the refractory metals, tungsten-base alloys such as W, W-25%Re, Densimet, and W-1%LaO_2, are most commonly used as tool materials for nickel-aluminum bronze, titanium-alloys, and steels.[39]

3.3.3.1.3 Carbides and Metal-Matrix Composites

Tungsten carbide (WC) based tools such as WC-Co are used due to their excellent toughness and insensitivity to sudden changes in temperature and load for friction stir welding of steel and Ti-alloys. Metalmatrix composites using TiC as the reinforcing phase such as TiC:Ni:W are used for welding Cu.[39,40]

3.3.3.1.4 Polycrystalline cubic boron nitride (pcBN)

Polycrystalline cubic boron nitride is a preferred tool material for FSW of hard alloys. Outstanding high temperature properties are facing negative aspects such as low fracture toughness and particularly high manufacturing costs. As a consequence, pcBN is only used for welding steels and Ti-alloys with small thickness.[40]

3.3.3.2 Tool Geometries

Tool geometry has an important impact on the FSW-process by directly influencing heat generation, traverse force, torque, and the thermomechanical environment experienced by the tool, as well as the flow of the workpiece material and the motion of the tool.

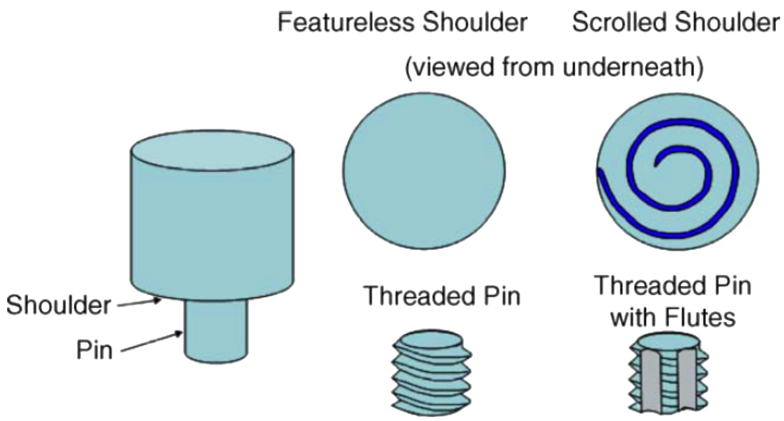

Figure 3.17: Sketch of the most important FSW-tool features [29]

The most important features, shoulder diameter, shoulder surface, and probe geometry, are illustrated in Figure 3.17 and dicussed in this section.[40]

3.3.3.2.1 Shoulder Geometry

The tool shoulder geometry can be described by two main factors, the shoulder diameter and the shoulder features.

Shoulder Diameter

The diameter of the tool shoulder is important because the shoulder generates most of the heat and largely established the material flow field.[40] At the early days of FSW an optimal ratio of shoulder diameter to probe diameter was suggested between 2.5 to 1 and 3 to 1, depending on the workpiece material and sheet thickness.[39] Recently a new approach was proposed that focussed on the optimization of the sticking and sliding components of torque, whereas it was suggested that the optimum shoulder diameter should correspond to the maximum sticking torque for a given set of welding parameters and workpiece material.[41]

Shoulder Features

Beside the shoulder diameter, also the nature of the shoulder surface is very important for heat generation and material flow.[39]

The first shoulder design was the concave shoulder with an angle of 6 to 10° between the edge of the shoulder and the probe. The concavity of the shoulder serves as a reservoir from which material is pushed into the flow of the pin during the forging action of the shoulder. Concave shoulders require a certain tilt angle to maintain the reservoir and to enable a compressive forging force of the trailing edge of the shoulder.[39]

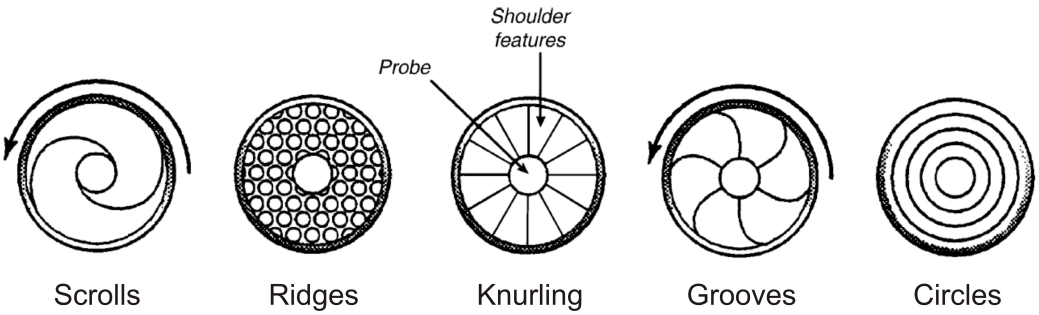

Figure 3.18: Different tool shoulder geometries [29]

Shoulder features such as scrolls, ridges, knurling, grooves, and concentric circles (from left to right in Figure 3.18) can increase the amount of material deformation produced by the shoulder. The advantage of the more complex scrolled shoulders over simple concave shoulders are feasibility of nonlinear welds due to removing of the tool tilt, greater welding speeds, and reduction of flash.[39]

Convex shoulders are only successfully used when combined with a scrolled shoulder in a way that material is moved from the outside of the shoulder toward the probe. The advantage of this design is that the outer edge of the tool does not need to be engaged with the workpiece to produce sound welds which allows for a larger flexibility in the contact area and improves the joint mismatch tolerance.[39]

3.3.3.2.2 Probe Geometry

The probe or pin produces heat by friction and plastic deformation. In order to optimize those features a number of different designs has been developed over the years. Some of which are illustrated in Figure 3.19. A round-bottom cylindrical pin (Figure 3.19 a) was initially used by the inventors of FSW. The round bottom reduces tool wear during plunging, threads are used to transport material from the shoulder down to the bottom of the pin. The flat-bottom cylindrical pin, given in Figure 3.19 (b), today is the most widely used design due to its advantage over the round-bottom pin in terms of material flow. A further improvement is the truncated cone pin illustrated in Figure 3.19 (c) which is used for welding thick aluminum plates. This design has lower transverse loads and the largest moment load occurs at the base of the cone, where it is the strongest. In order to improve the material flow and reduce loads, even more complex tools such as the MX Triflute pin (Figure 3.19 d) have been developed over the years. However, in specific applications, for example highly abrasive composite alloys, threadless probes are useful because thread features would not survive without fracture or excessive wear.[39]

(a) Threaded cylindrical

(b) Threaded cylindrical

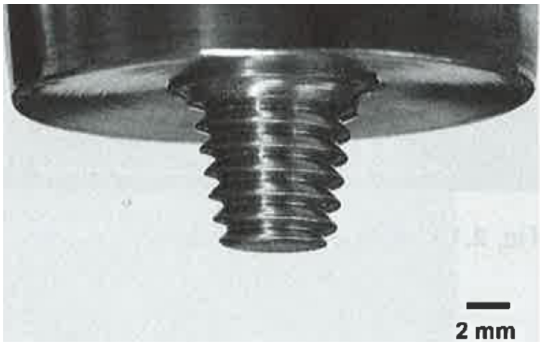

(c) Threaded conical

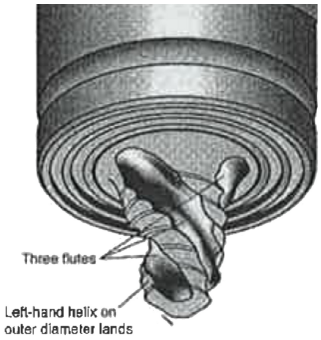

(d) MX Triflute pin

Figure 3.19: Different tool probe designs [39]

3.3.4 Friction Stir Welding Applications

In 1997, Thomas and Nicholas [42] described the potential fields of application for friction stir welding. In this study, the applicability of friction stir welding of materials such as aluminum, copper alloys, lead, titanium, and zinc for different branches in the transportation industries was discussed. According to the authors, the applications would include the following:

- Airframes, fuel tanks, skins in airspace industries
- Sheet, bodywork, engine frames for automotive industries
- Railway wagon, coachwork, bulk carrier tanks in railway industries
- Hulls, decks, internal structures for shipbuilding industries

In 2009, Threadgill *et al* [43] published an article on friction stir welding of aluminum alloys, including a review of commercial applications. It was reported that, at least for Al-alloys, the number of FSW applications had significantly increased over the years. In marine industries MIG welding has been replaced by FSW for welding huge superstructures of cruise ships that contain many kilometres of welds. In high speed vessels the bulkheads and decks were welded using FSW. In aerospace industries a large number of fasteners such as rivets has been replaced by high quality friction stir welds in line with process improvement and cost savings. Figure 3.20 shows an Airbus central wing box that has been successfully redesigned from a rivet-design to a FSW-design. High speed aluminum railcars with up to $25\,m$ long welds were considered as an ideal application for FSW in railway industries. In automotive industries the FSW technology was improved towards friction stir spot welding and robotic FSW which resulted in growing acceptance in this field.

3.3.4.1 Friction Stir Welding of Steel

As explained, today there are various fields of application for friction stir welding of relatively soft materials. Consequentially, the technology readiness level (TRL) is high, especially for Al-alloys. The reason therefore is the combination of high weld quality with a reduction in production costs.[46]

Steels represent by far the largest group of materials in structural applications, which is mainly attributed to their strength, versatility, and cost efficiency. When it comes to FSW, those properties, especially the high strength, can cause serious problems. Figure 3.21 illustrates the temperature dependence of the strength of Al-alloys and steels. Apparently, the strength of steels is much higher even at elevated temperatures.

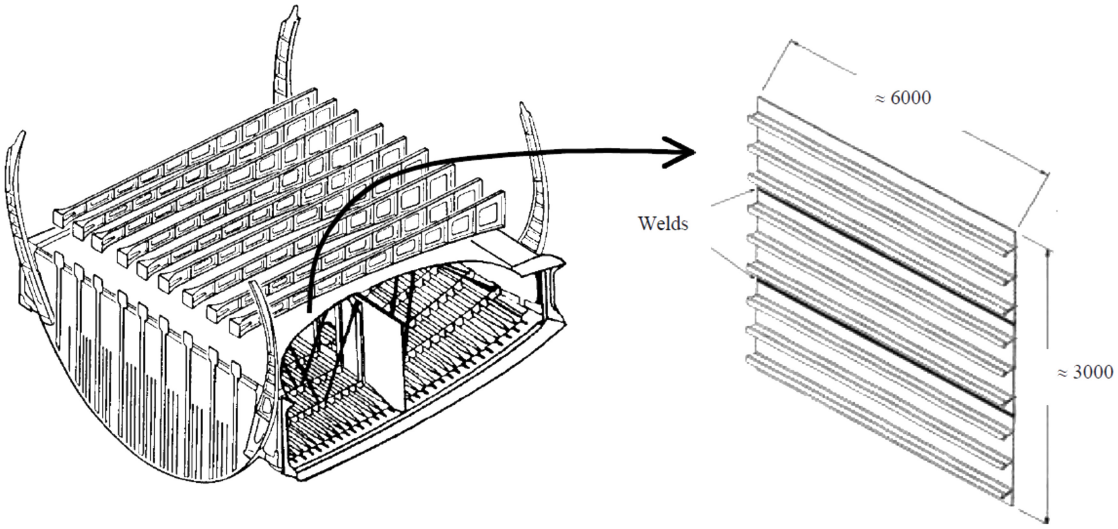

Figure 3.20: Friction stir welded Airbus central wing box [44]

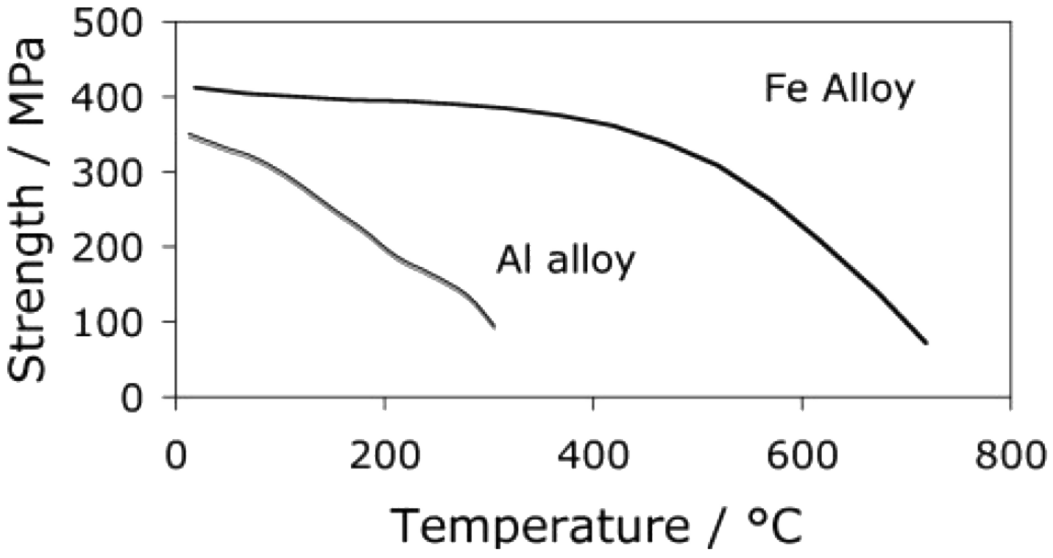

Figure 3.21: Temperature dependence of strength of Al-alloys and steels [45]

As a consequence, higher process temperatures up to $1200°C$ need to be reached in order to fully plasticize the material.[45] However, despite the high temperatures and process forces there have been various reports of successfully friction stir welded steel sheets such as advanced high strength steels (AHSS) for automotive industries [33], martensitic precipitation hardening 15-5PH [35], and martensitic-ferritic DP 590 [37]. In most cases the mechanical properties of the welds were excellent. Hence, the reason for the application deficit of friction stir welding of steel is definitely not the eligiblity of the material itself.

The main barrier for an industrial breakthrough of friction stir welding of steel is the lacking of cost efficient tools that can handle the high process temperatures and forces. At the moment, the tools with required properties can not be reasonably reused which results in a very cost-inefficient production process. In case of mass production therefore, the development of reliable and long lasting tools is considered the most important step. However, another opportunity of implementing FSW to steel is given when identifying a joining problem which can not be solved with conventional techniques. Such a niche problem would certainly deal with high-end components and materials in order to justify the costs.[45]

Since the excellent tensile properties of multilayered steel are attributed to the laminated composition, the deterioration of the structure during a welding process is preferably low. Conventional fusion welding methods would certainly destroy the laminated structure due to melting by creating a rather undefined alloy.[47] The FSW-process, as explained, provides solid state welding and thus less impact on the joining material. Consequentially, FSW was considered as the only suitable welding technique for joining high strength/ductility multilayered steel sheets.

4 Experimental

In this study, sheets of a laminated composite material consisting of alternating layers of SUS301 austenitic stainless steel and SUS420J2 martensitic stainless steel were welded in butt configuration using FSW. The weldability and the influence of different welding parameters on the mechanical properties and on the microstructure were investigated. Moreover, the effects of a post weld heat treatment were evaluated. This chapter deals with the friction stir welding experiments that were carried out, whereas the basic contents are a detailed description of the welded steel sheets, an overview of the used materials, and an explaination of the experimental setup and procedure.

4.1 Multilayered Steel

The material used in the present study was a multilayered steel composite consisting of 15 alternating layers of SUS301 austenitic stainless steel (8 γ-layers) and SUS420J2 martensitic stainless steel (7 α-layers). The chemical compositions (mass%) and initial layer thicknesses of the single constituent materials are shown in Table 4.1.

4.1.1 Production Process

Figure 4.1 shows the steps in the production process of the multilayered steel sheets. In order to fabricate the composite, the steel sheets were stacked and sealed at the edge by tungsten arc welding prior to hot rolling at $1100°C$ to a thickness of $1.6\,mm$ (I). After a subsequent annealing heat treatment at $680°C$ for 10 minutes (II) the multilayered composite was cold rolled to a final thickness of $1.2\,mm$ (III) and finally heat treated at $1000°C$ for 2 minutes followed by cooling in N_2 gas with a cooling rate of $5°C$ per second (IV). The aim of the complex production process was the adjustment of the microstructure in a way that the most favorable mechanical properties were achieved.

Material	C	Si	Mn	P	S	Cr	Ni	bal	Thickness [mm]
SUS301	0.1	0.51	0.78	0.028	0.001	16.80	6.54	Fe	1
SUS420J2	0.29	0.61	0.44	0.023	0.003	13.13	0.22	Fe	1

Table 4.1: Chemical composition of the constituent steels

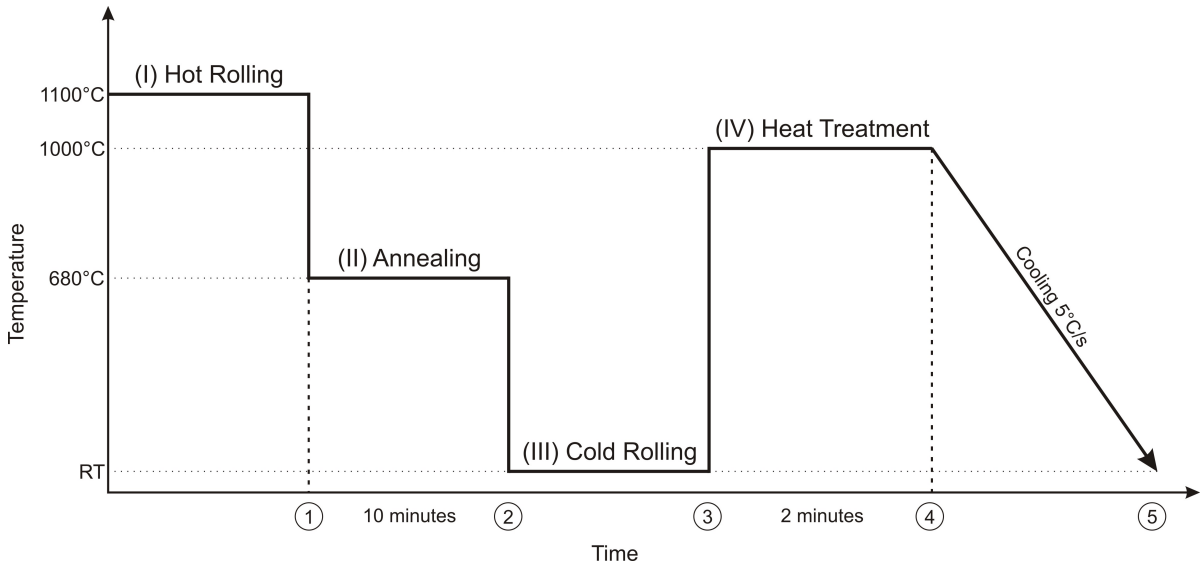

Figure 4.1: Production process of multilayered steel

4.1.2 Microstructure

As a consequence of hot rolling and cold rolling processing combined with various heat treatments, the SUS301 layers showed a microstructure composed of mainly austenite, some deformation induced martensite, and a large number of Cr-rich precipitates at the grain boundaries, whereas the SUS420J2 layers showed a mainly martensitic microstructure with some ferrite. Figure 4.2 shows an overview of the structure in the multilayered compound, Figures 4.3 and 4.4 demonstrate EBSD images of the microstructure within the single layers. As in all EBSD images in this study, green grains refer to fcc-structure, while red grains represent bcc-structure. Accordingly, in Figure 4.3 austenitic grains appear green, whereas grains of deformation induced martensite are visualized by red color. In Figure 4.4 the martensitic/ferritic microstructure in SUS420J2 layers is given. Since ferritic and martensitic grains are both present in bcc-structure, they are both represented by red color which complicates differentiation. However, due to the different shapes of the grains, lath type microstructure can be identified as martensite whereas roundish grains represent ferrite. Furthermore, some green spots were observed within the α-layers, which could be identified as cubic face centered Cr-rich $M_{23}C_6$ particles by applying an EDS line scan (Figure 4.5) through the precipitates. Due to the low incidence of precipitates in α-layers, their influence on the mechanical properties was considered as negligible. Figure 4.6 demonstrates the interface between an austenitic and martensitic layer in detail. Apparently, with high magnification a large number of precipitates at austenite grain boundaries became visible, as illustrated in Figure 4.6 (b). Also these particles could be identified as Cr-rich, most likely $M_{23}C_6$, by apply-

ing an EDS line scan across the interface directly through a precipitate (Figure 4.7). Incidentally, the EDS analysis showed good correlation to the chemical compositions of the constituent materials, demonstrated by the increase in Cr- and Ni-content by approaching the upper SUS301 layer from SUS420J2.

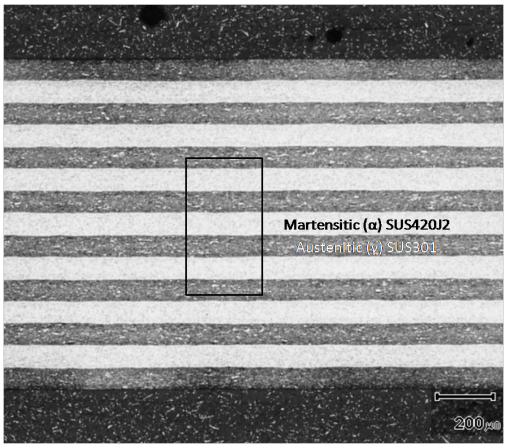

(a) Optical micrograph

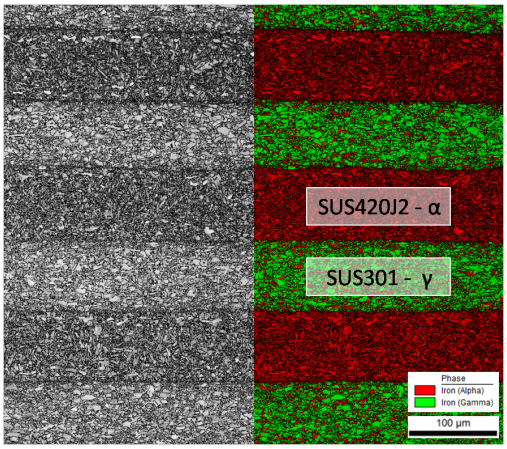

(b) EBSD image

Figure 4.2: Microstructure in multilayered steel consisting of SUS301 and SUS420J2

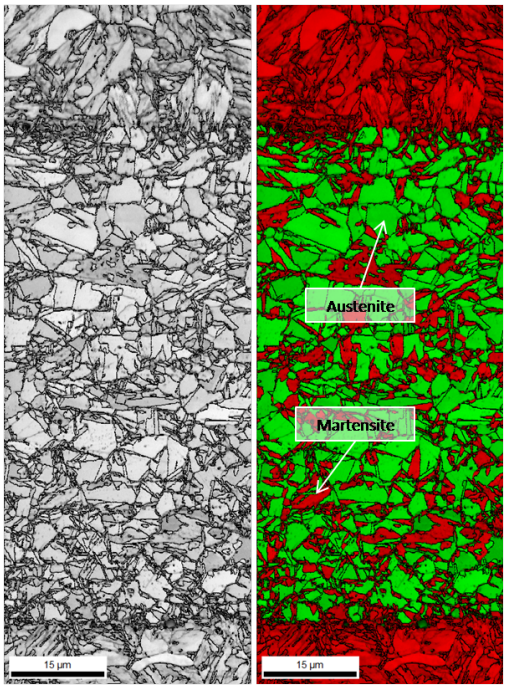

Figure 4.3: Structure in SUS301

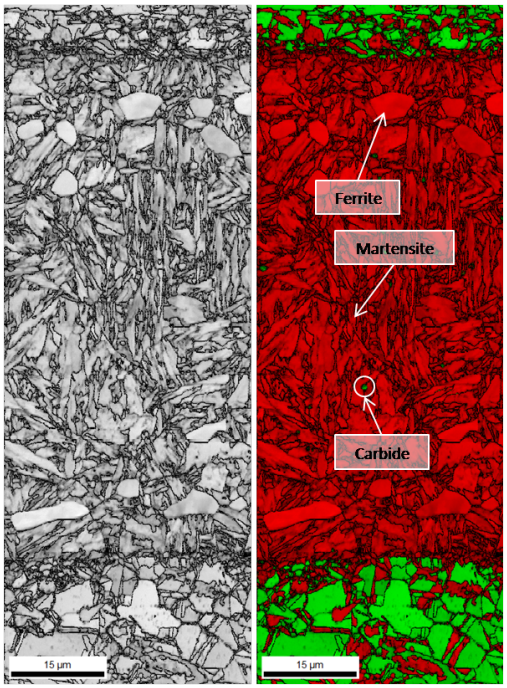

Figure 4.4: Structure in SUS420J2

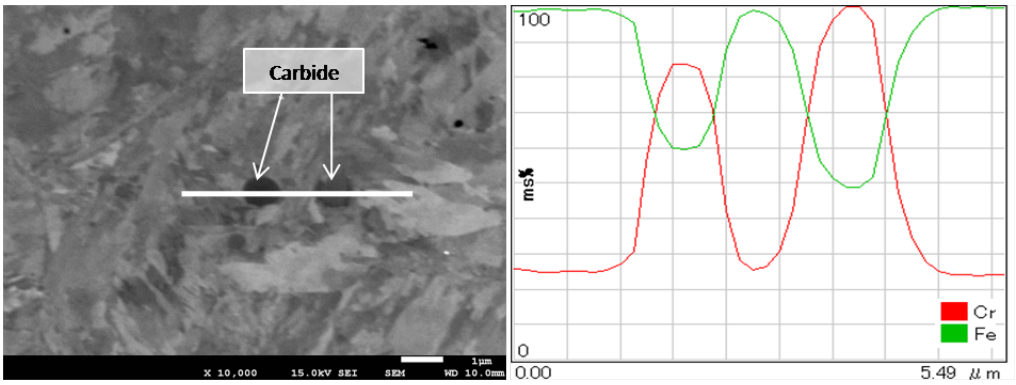

Figure 4.5: EDS line scan through Cr-rich precipitates in an α-layer

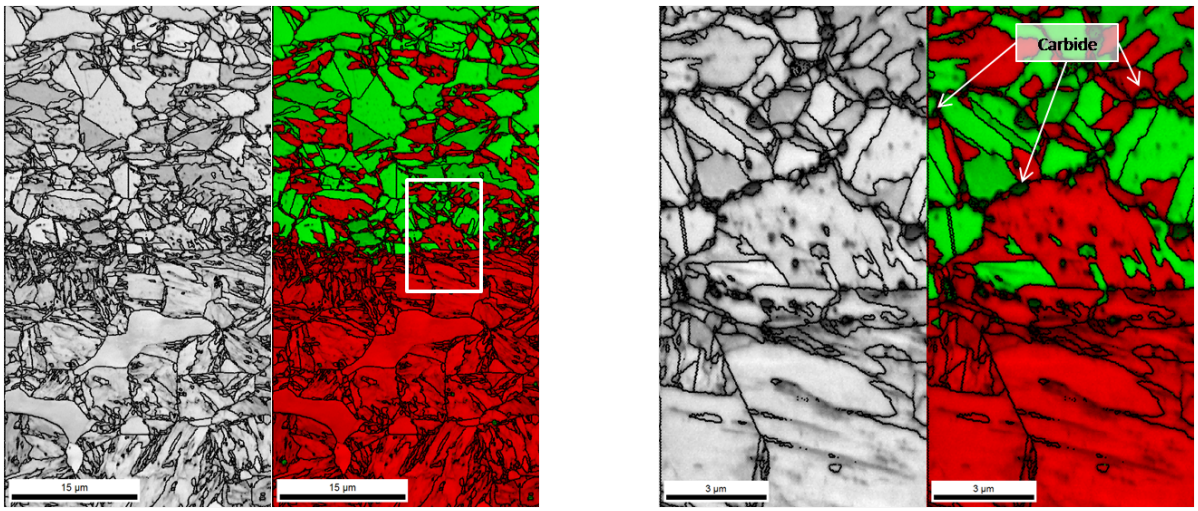

(a) Layer interface

(b) Interface in detail. 10000 x

Figure 4.6: Microstructure of the interface between SUS301 and SUS420J2

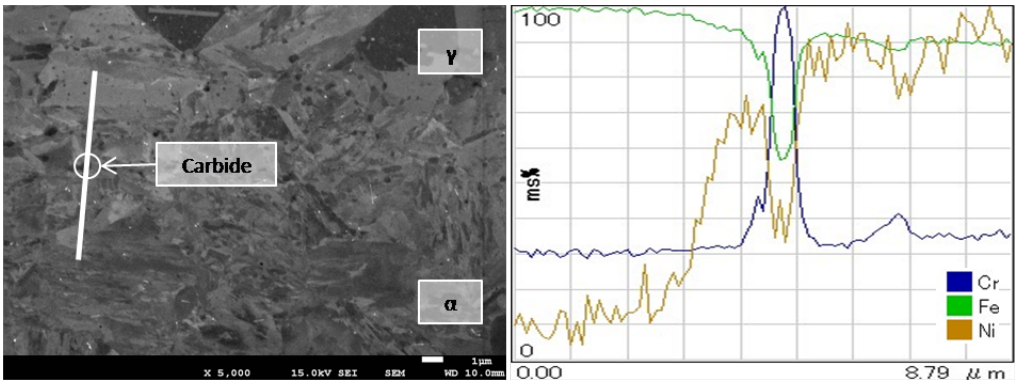

Figure 4.7: EDS line scan across the interface through a Cr-rich precipitate

4.1.3 Mechanical Properties

A comparison of the tensile properties of the single monolithic constituent materials to that of the multilayered composite is given in Table 4.2. As desired, the multilayered material showed outstanding tensile properties by combining high strength and ductility. In tensile testing an ultimate tensile strength (UTS) of 1370 MPa and a fracture elongation of 26 % were reached. Consequentially, the multilayered steel had a tremendous energy absorbtion capacity, as demonstrated in Figure 4.8. Bending tests have been performed for a simple geometry of both multilayered steel and DP 590 martensitic-ferritic dual phase steel which is currently used for structural parts in automotive industries. It was shown that the energy absorbtion capacity of the multilayered steel exceeded that of DP 590 steel by a factor of 5.

Material	UTS [MPa]	Elongation [%]
SUS301	1145	44
SUS420J2	1750	3.5
Multilayered Steel	1370	26

Table 4.2: Tensile properties of SUS301, SUS420J2 and multilayered steel

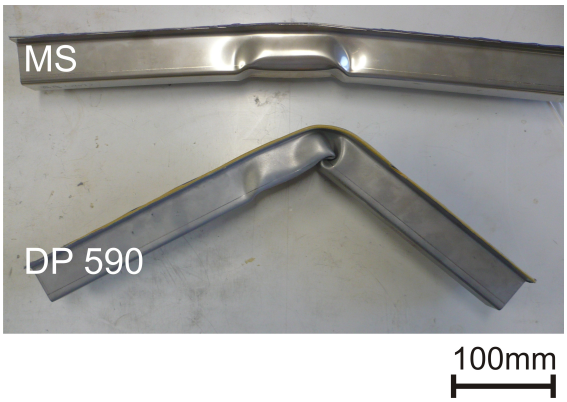

(a) Same deformation energy

(b) Same deformation: 1400J - 270J

Figure 4.8: Deformation behavior of multilayered steel (MS) compared to DP 590

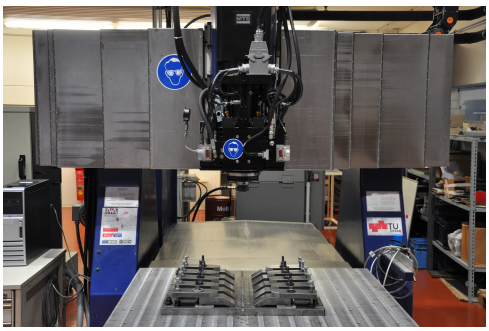

Figure 4.9: MTS FSW machine

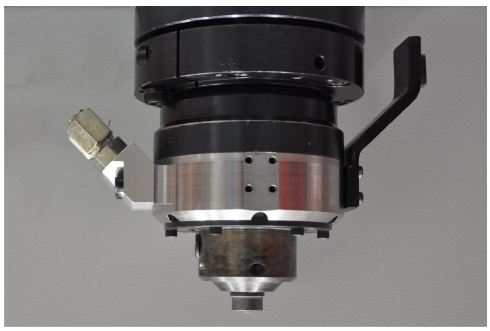

Figure 4.10: Water cooled head

4.2 Used Equipment

4.2.1 Friction Stir Welding Machine

All FSW experiments were conducted using the MTS ISTIR BR4 machine located at the welding laboratory of the Institute for Materials Science and Welding of Graz University of Technology (Figure 4.9). The capabilities of the machine are listet below. The machine was especially designed for research and therefore was equipped with a considerable measuring system. That facilitated proper automatic control and gave the opportunity to verify the process stability by evaluating the process parameters. Due to the enormous heat generation during friction stir welding steel a special water cooled head was used (Figure 4.10).

- Working area: $2450\,\mathrm{x}\,1250\,mm$
- Maximum welding speed: $6350\,mm\,min^{-1}$
- Maximum tool rotation speed: $3200\,rev\,min^{-1}$
- Maximum torque: $180\,Nm$
- Maximum down force: $35.6\,kN$

4.2.2 Clamping

Due to the application of very high forces and torques during the process the blanks had to be clamped rigidly to the working area of the machine. Since only very tight tolerances concerning gap width were allowed, rigid clamping alone was not sufficient. Also very accurate positioning of the blanks had to be ensured. For all experiments a mechanical clamping device as shown in Figures 4.11 and 4.12 was used. The flexible

Figure 4.11: Mechanical clamping

Figure 4.12: FSW process setup

usability of the device gave the opportunity to guarantee appropriate clamping also in case of highly distorted blanks.

Backing Plates

The use of an appropriate backing plate is very important in friction stir welding, especially when it comes to welding thin steel sheets in butt configuration. Due to the combination of high temperature and pressure caused by the process itself sticking of the sheets to the backing plate can hardly be avoided. Of course the impact of the backing plate on the welding result should be preferably low. Therefore the eligibility of three different types of backing plates, as listet below, was investigated.

- Oxide-coated steel plate
- WC-Co plate
- Ni-base alloy plate

4.2.3 FSW-Tool

Due to the high strength of the multilayered steel sheets a very hard and strong but also quite tough tool needed to be used in order to keep tool wear as low as possible and in addition avoid sudden probe fracture. A tool that has those properties was developed at the Institute for Materials Science and Welding within the project JOIN B7 in cooperation with the company Boehlerit. The nitride coated tool was made of a sintered matrix consisting of 92 $wt\%$ tungsten carbide and 8 $wt\%$ cobalt. The hardness equaled 1275 $HV30$. The tool consisted of a concave shoulder with a diameter of 17 mm and a conical probe with a tip diameter of 5.5 mm and a length of 0.85 mm.[48] The rather simple tool design is sketched in Figure 4.13. A complete drawing is attached to the Appendix of this document. Figure 4.14 shows the tool from different views.

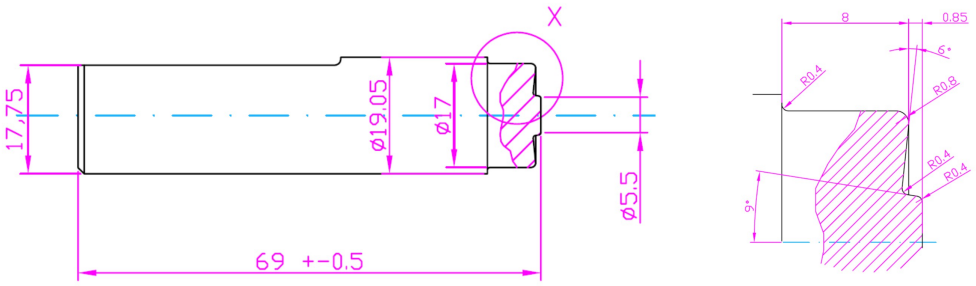

Figure 4.13: Sketch of the WC-Co FSW-tool

(a) Side View (b) Front View (c) Probe and Shoulder

Figure 4.14: Sintered tungsten carbide - cobalt FSW-tool

4.3 Experimental Procedure

The multilayered steel sheets were cut to a size of 500 x 120 mm and friction stir welded in rolling direction. For every weld setup four welds with varying parameters and a length of 100 mm each were accomplished. Figure 4.15 gives a sketch of the welding configuration. All welds were made in force control mode at a constant tilt angle of 1.5° between the tool rotation axis and the vertical axis. The down force varied between 19 kN and 24 kN, whereas the majority of welds was accomplished at a down force of 19 kN and was only increased to 24 kN in special cases. The tool rotation speed ranged from 300 to 1200 $rev\,min^{-1}$ and the welding speed ranged from 50 to 500 $mm\,min^{-1}$. A summary of all used welding parameters is given in Table 4.3.

In order to assess the quality and the properties of the weldings, a number of analyses and investigations was carried out. Individual measurements instead of statistical evaluations were performed, since for each parameter combination only one weld could be produced. In Figure 4.16 the sampling locations for different investigations are illustrated. Temperature measurements were accomplished, the mechanical properties were assessed by using tensile testing and hardness testing, and the microstructure was investigated with light optical microscopy (LOM), scanning electron microscopy (SEM), electron backscatter diffraction (EBSD), and transmission electron microscopy (TEM).

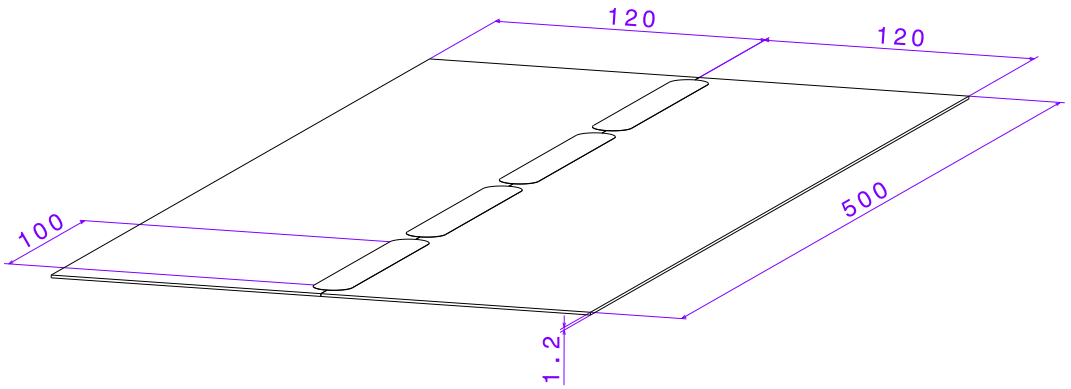

Figure 4.15: Welding configuration

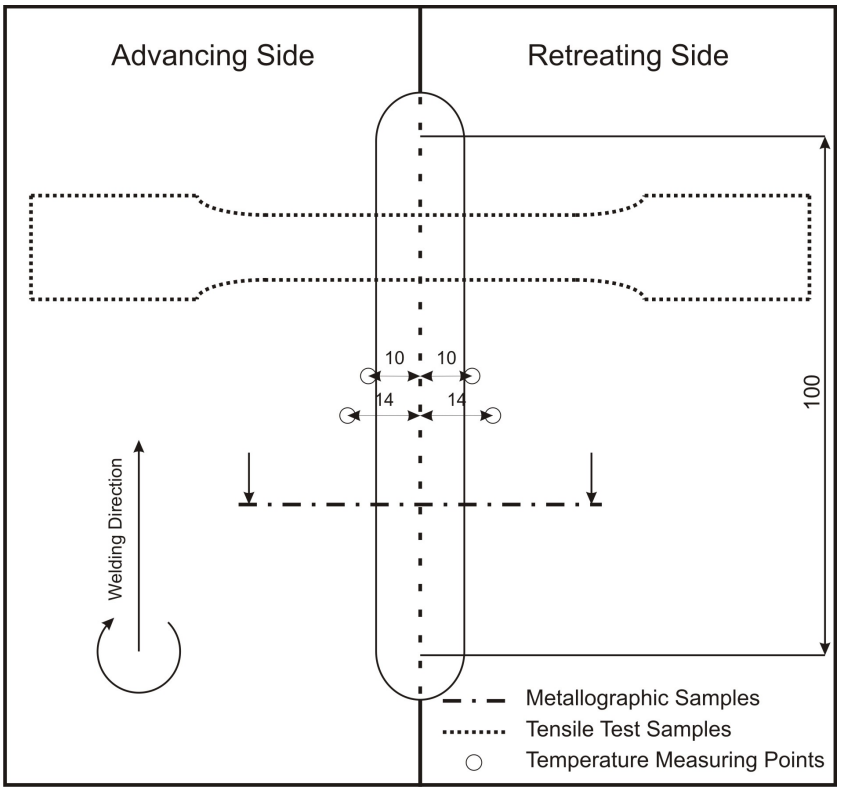

Figure 4.16: Sampling setup

Tilt angle [°]	Down Force [kN]	Spindle Speed [rpm]	Weld Speed [mm/min]
1.5	19	300	100
			150
		400	100
			150
			200
		550	50
			80
			100
			150
			200
			300
		700	200
			300
		800	200
			300
		1200	300
			500
	24	300	100
			150
		400	100
			150
			200
			300

Table 4.3: Welding parameters overview

4.3.1 Temperature Measurement Setup

Temperature measurements using K-type thermocouples were accomplished on top of the welded steel sheets at a distance of $10\,mm$ and $14\,mm$ from the weld center both on the advancing side (AS) and on the retreating side (RS) due to expected temperature asymmetries.[25] The thermocouples were fixed on the sheets by resistance spot welding.

4.3.2 Assessment of Mechanical Properties

The mechanical properties were investigated using tensile testing in transverse to welding direction and hardness measurements across the weld seam.

4.3.2.1 Tensile Testing

Tensile tests at room temperature were performed transverse to welding direction in order to assess the most important mechanical properties, that are tensile strength and fracture elongation. The dimensions of the tensile specimen were $12.5\,mm$ in width, around $1.2\,mm$ in thickness, and $50\,mm$ in gauge length according to the standard EN $10002-1:2001$.[49] The samples were left in as-welded shape, ridges and flashes were not milled off before testing. Tensile tests were carried out at Graz University of Technology using a RMC-100 tensile tester with a maximum load of $100\,kN$ on the one hand, and at The University of Tokyo using a Shimadzu Autograph with a maximum load of $50\,kN$ on the other hand.

4.3.2.2 Hardness Testing

Hardness measurements were accomplished in both SUS301 and SUS420J2 layers in order to create hardness profiles across the weld seam. A resolution of about $200\,\mu m$ was considered to be sufficiently accurate to get proper patterns. The used hardness measurement method was HV0.1 Vickers hardness with a load of $0.981\,N$. A Shimadzu HMV Micro Hardness Tester was used for the investigations at The University of Tokyo.

4.3.3 Metallurgical Investigations

Detailed investigations on the microstructural response to different welding parameters were carried out in different welding regions. Depending on the desired magnification and resolution more or less sophisticated approaches were followed. Sample preparation was similar for all investigations apart from TEM, as the main steps are listet below:

1. Embedding the sample in a Nickel containing material (necessary for SEM)
2. Flatten the sample surface by grinding

3. Diamond polishing ($1\mu m$) until no scratches were visible

4. Al_2O_3 polishing ($0.06\,\mu m$) until no scratches were visible in an optical microscope

4.3.3.1 Light Optical Microscopy

Light optical microscopy (LOM) was mainly used for illustrations on a macroscopic level and for rather low magnifications. For LOM samples, the above mentioned steps in sample preparation were extended by one final step, that was adjusting a desired contrast by etching. Due to the differences between SUS301 and SUS420J2 in resistance against the etching attack of certain media it was almost impossible to properly etch both constituent materials at the same time. However, two different etchants were considered as quite suitable for the multilayered steel.

V2A etchant

Chemical etching using the V2A etchant [50] was performed, whereas the attack in martensitic material was in general stronger than in austenitic regions. Consequentially, the martensitic layers appeared darker in the optical micrographs than the austenitic layers. Before using, the etchant was heated up to temperatures around $100°C$ in order to increase the aggresivity. In that condition the etching duration was only about 10 seconds.

Oxalic acid etchant

The second approach was electro-chemical etching using an oxalic acid. By using this method the austenite grain boundaries were most strongly attacked. In contrast to V2A etchings therefore, in electro-chemically etched micrographs the austenitic layers appeared darker than the martensitic layers. Electric settings were used as follows: The positive pole was connected to the sample, the negative pole was connected to a Cu-electrode which plunged into the liquid etchant. At a voltage of $10\,V$ and a currency of $2\,A$, the etching duration was only 3 to 10 seconds.

4.3.3.2 Scanning Electron Microscopy

Scanning electron microscopy (SEM) was performed to generate high quality images of the weld cross sections on the one hand, and fracture surface images after tensile testing on the other hand. Furthermore, SEM was used for energy-dispersive X-ray spectroscopy (EDS) analysis to investigate the chemical composition in different regions. The used device was a JEOL JSM-7001FA Field Emission Scanning Electron Microscope, located at the Department of Materials Engineering at Tokyo University.

For SEM the basic sample preparation was extended by polishing with a slightly acidic colloidal silica polishing suspension [51] with a pH-value of 9.8. After 30 - 60 minutes

of polishing, this treatment led to a very nice and shiny sample surface and a slight contrast between α- and γ-layers.

4.3.3.3 Electron Backscatter Diffraction

Electron backscatter diffraction (EBSD) is a technique that has become almost universally used for characterizing the local crystallography of materials and for obtaining microtexture data. EBSD is an add-on package to scanning electron microscopy (SEM) and thus gives crystallographic data and imaging with a resolution in nanometer range combined with the advantages of an SEM such as capacity of large specimens.[52,53]

In the present study, EBSD was in particular used for microstructure characterization in different weld regions at a magnification range from 100 x to 10 000 x. For EBSD the sample preparation was finalized in the same way as for SEM, by buffing with silica polishing suspension for 30 - 60 minutes.

4.3.3.4 Transmission Electron Microscopy

Transmission electron microscopy (TEM) was carried out in order to visualize very small microstructure components in nanometer range at magnification levels from 30 000 x to 100 000 x. A Hitachi H800 transmission electron microscope located at the Department of Materials Engineering of Tokyo University was used.

As mentioned above, the sample preparation for TEM differed significantly from that for all other investigations. At first samples with dimensions of about $8 \times 8\,mm$ were ground to a thickness of only $60 - 80\,\mu m$, followed by a mechanical piercing process to produce standardized round samples with a diameter of $3\,mm$. Finally the samples were thinned to foils with a thickness of less than $100\,nm$ by using electrochemical twin jet polishing. A schematic sketch of a finished TEM sample is given in Figure 4.17.

4.3.4 Post Weld Heat Treatment

The influence of a post weld heat treatment (PWHT) on the mechanical properties and on the microstructure was assessed by applying a similar heat treatment after welding as in the last step of the production process of the multilayered steel. More precisely, the PWHT included holding at a temperature of $1000°C$ for 2 minutes followed by air cooling (Figure 4.18). The differences between PWHT samples and as-welded samples were investigated using the same methods as mentioned above in this chapter.

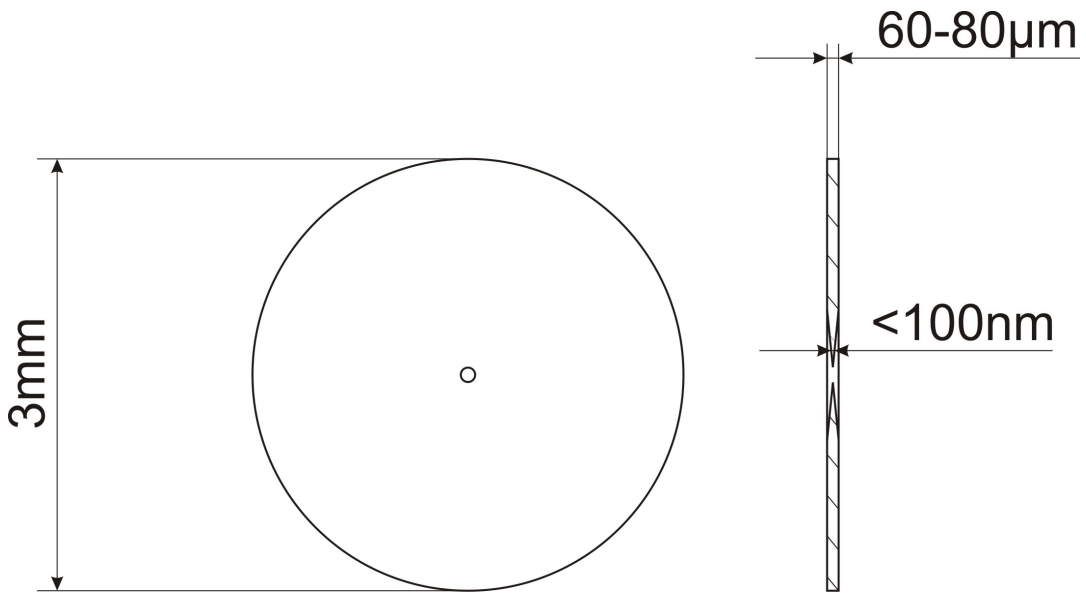

Figure 4.17: Schematic sketch of a TEM sample

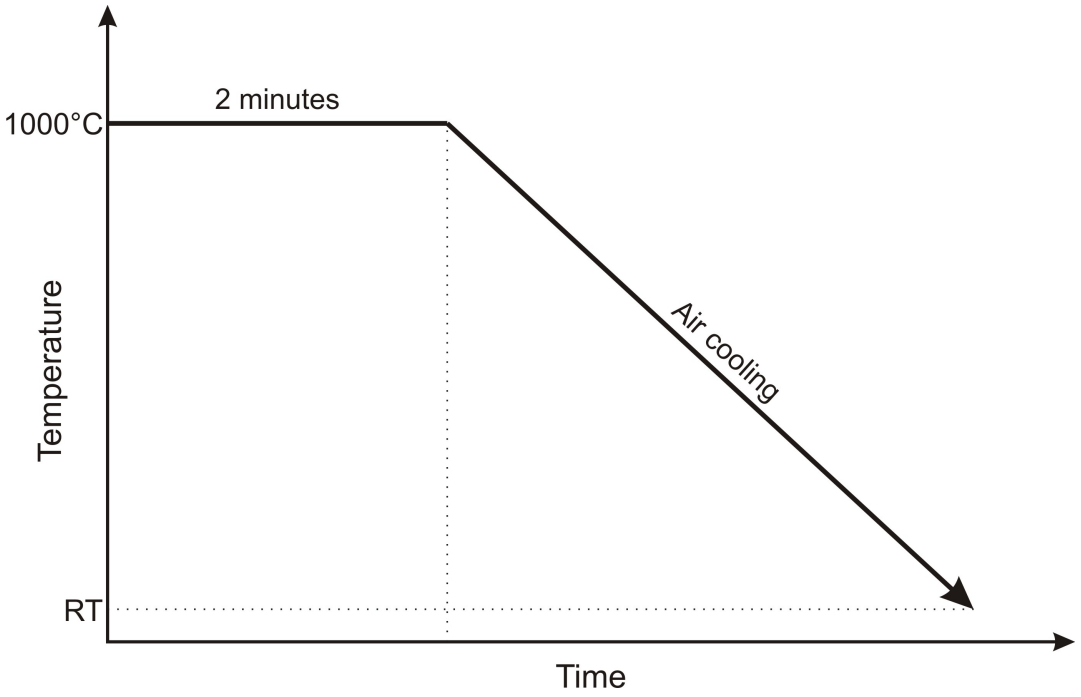

Figure 4.18: Temperature profile during PWHT

5 Results and Discussion

In this chapter, the results of performed analyses and investigations are presented. Temperature measurements, tensile testing, and LOM were performed for every single parameter set. Hardness testing and detailed metallographic investigations were only carried out for selected samples. Due to the much smaller range of investigated parameter combinations at $24\,kN$, systematic analyses are certainly limited to welds accomplished at $19\,kN$. Hence, the influence of an increase in down force for certain parameter combinations is only presented superficially.

5.1 Feasibility Study and Process Optimization

In order to create process stability a certain basic parameter setup needed to be found. Based on the parameters from previous studies [35,37], a qualified trial and error approach led to the desired stability. Figure 5.1 illustrates the improvement during the first welding experiments. It turned out that a displacement controlled process did not lead to the desired results since the plunge phase could not be controlled properly. As a consequence, the process was either stopped manually due to penetration of the shoulder caused by overheating, or the process was interrupted by the machine controller due to a sudden increase in vertical force as soon as the feed started. Figure 5.1(b) demonstrates the progress of the process parameters *Spindle speed* and *Down force* plottet over the process time in case of machine stop due to exceeding the maximum force of $35\,kN$.

However, in force controlled mode a proper parameter basis was found, whereas it turned out that a short plunging phase was crucial for the stability of the whole process. In order to avoid overheating, a plunging depth of only $0.55\,mm$ in combination with a high tool rotation speed of $1200\,rev\,min^{-1}$ kept this critical phase as short as possible. Subsequently, as soon as the feed started, the tool rotation speed was adjusted to the desired value and the shoulder was pushed on the sheet surface with the predefined force. Figure 5.2 illustrates the outcome of a stable welding process with a tool rotation speed of $800\,rev\,min^{-1}$ and a down force of $19\,kN$.

Figure 5.3(a) shows a weld cross section after process optimization. The right side refers to the advancing side (AS), the left side refers to the retreating side (RS). The position of the tool and the classification of the welding regions in parent material (PM), heat

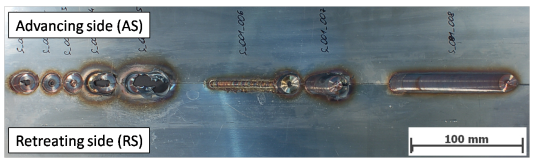

(a) First welded blanks

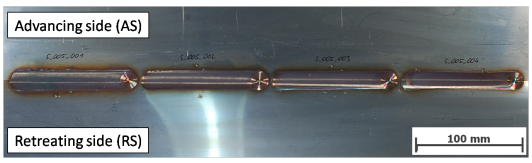

(a) Optimized welds

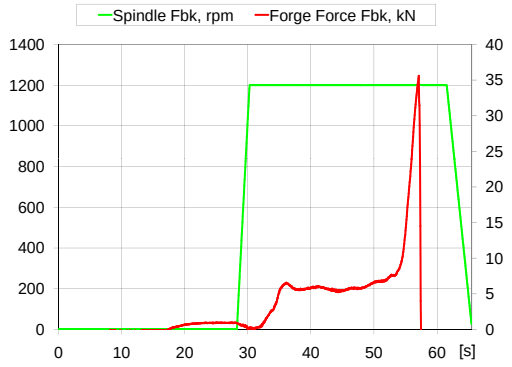

(b) First welding parameters

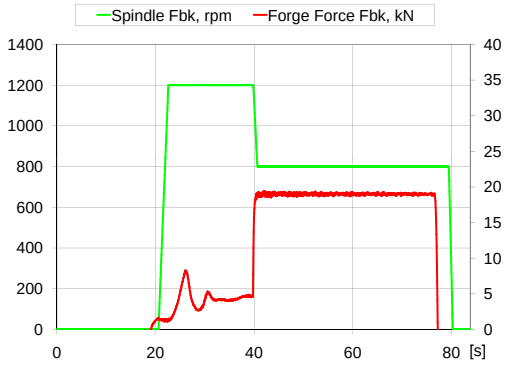

(b) Optimized parameters

Figure 5.1: First FSW experiments

Figure 5.2: Optimized FSW process

affected zone (HAZ), thermomechanically affected zone (TMAZ), and stir zone (SZ) are illustrated in Figure 5.3(b). As expected, the layered structure was mainly sustained, partial deterioration was only observed in the stir zone. In the weld region a process related slight reduction of the sheet thickness was noticed. With the optimized process no major problems concerning process stability were observed and complete welding was feasible with an appropriate parameters setup.

5.1.1 Eligibility of Different Backing Plates

In the course of process optimization also the eligibility of the three different backing plates was assessed. Detailed investigations were omitted since the classification of the backing plates only resulted from observations during the experiments.

5.1.1.1 Oxide-Coated Steel Plate

A conventional steel plate of 20 mm thickness with a ceramic coating of TiO_2 and Al_2O_3 was used as a backing plate. Unfortunaly, the desired effect of non-sticking due to the ceramic cover was not achieved. Rather, the coating was ripped off the steel plate when removing the welded sheets from the plate or parts of the weld remained on top of the plate, as shown in Figure 5.4 (a).

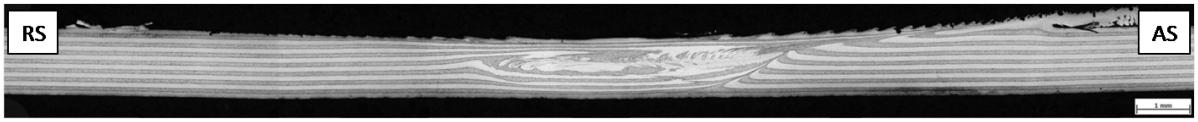

(a) Optical macrograph of a weld cross section

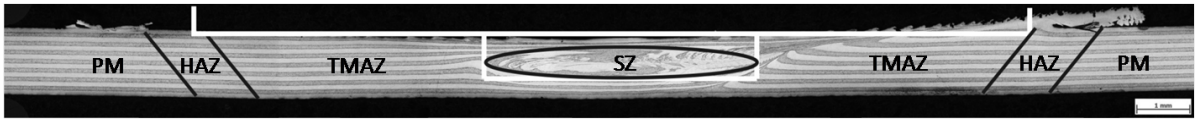

(b) Illustration of the tool position and the weld zones

Figure 5.3: Macrograph of a weld cross section after process optimization

(a) Coated steel plate

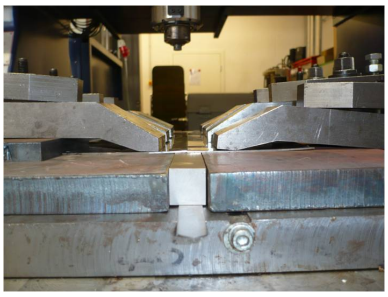

(b) WC-Co plate

(c) Ni-base plate

Figure 5.4: Overview of the used backing plates

5.1.1.2 WC-Co Plate

A different promising approach was the use of backing plates made of similar material as the FSW-tool (Figure 5.4 b). More precisely, the backing plates with dimensions of $20\,\mathrm{x}\,20\,\mathrm{x}\,250\,mm$ were made of a sintered material consisting of 90.5 % tungsten carbide and 9.5 % cobalt. Indeed, the sticking effect was reduced compared to the coated steel plate, instead the brittleness of the material turned out to be a big problem leading to sudden fracture under high loads during the FSW-process.

5.1.1.3 Nickel-Base Plate

Finally, backing plates made of a Ni-base alloy named Nicrofer 7216 [54] turned out to be most suitable for the FSW-process. The alloy mainly consistet of 75 % Ni, 14 - 17 % Cr, and 6 - 10 % Fe. Certainly, sticking to the plates could not be prevented completely, but the removal of the welded sheets was quite easy and did not endanger the welds. Furthermore, severe sticking was limited to high heat input welds, whereas the sticking effect was significantly reduced compared to the other plates when operating in lower heat input range. Figure 5.4 (c) shows a Nicrofer 7216 alloy plate in clamped position.

5.2 Temperature Measurement

As the heat input is directly linked to the revolutionpitch (Equation 3.3) and the down force, it was considered meaningful to analyse the temperature distribution as a function of those two parameters.

In the first part of this section therefore, the influence of different revolutionpitches on the temperature evolution on top of the welded sheets was assessed. The revolutionpitches ranged from a high heat input level of 0.09 to a low heat input level of $0.55\,rev\,min^{-1}$. In the second part, the influence of an increase in down force from 19 to $24\,kN$ was evaluated.

5.2.1 Influence of the Revolutionpitch on the Temperature Pattern

Figure 5.5 shows temperature cycles for different revolutionpitches measured on top of the welded steel sheets at a distance of 10 and $14\,mm$ both on the advancing side (AS) and on the retreating side (RS) for a down force of $19\,kN$. Apparently, the temperature on the advancing side was in general higher than on the retreating side due to an overlap of tool rotation speed and welding speed resulting in higher friction and plastic deformation. This fact showed good correlation to previous studies [35,55]. As expected, the maximum temperatures increased with decreasing revolutionpitch in every single measuring point. Total maxima were reached at $10\,mm$ distance on the advancing side. The maximum temperatures at every measuring point for different revolutionpitches are summarized in Table 5.1. Figure 5.6 illustrates the data from the table showing a graph of the peak temperatures reached at different distances from the weld center plotted over the revolutionpitch. It could be deduced, that the gradient of the curves decreased with increasing revolutionpitch.

Revpitch $\left[\frac{mm}{rev}\right]$	AS $10\,mm\,[°C]$	AS $14\,mm\,[°C]$	RS $10\,mm\,[°C]$	RS $14\,mm\,[°C]$
0.55	393	208	263	174
0.36	416	266	304	197
0.25	477	330	367	227
0.09	765	480	660	399

Table 5.1: Maximum temperatures at different revolutionpitches. $F_z = 19\,kN$

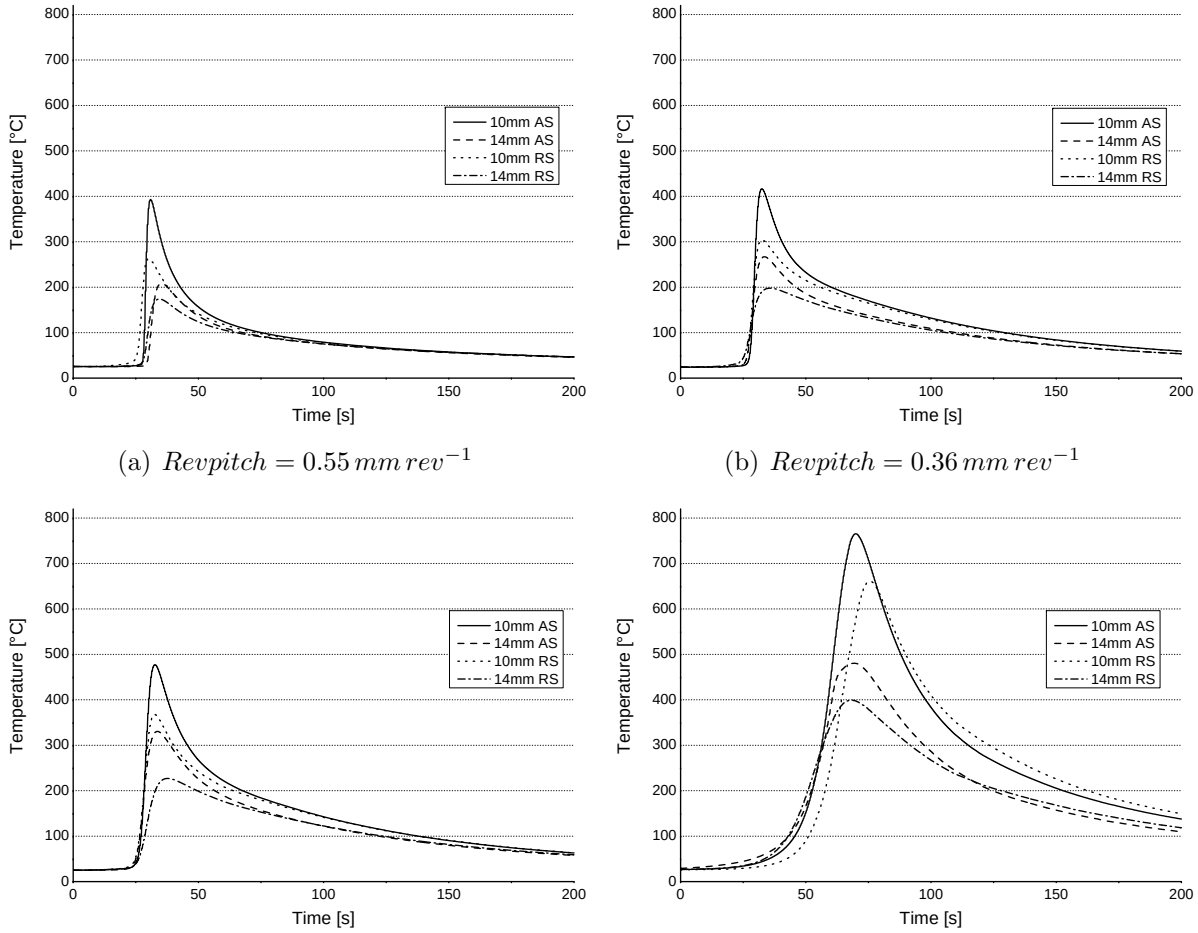

(a) $Revpitch = 0.55\,mm\,rev^{-1}$ (b) $Revpitch = 0.36\,mm\,rev^{-1}$

(c) $Revpitch = 0.25\,mm\,rev^{-1}$ (d) $Revpitch = 0.09\,mm\,rev^{-1}$

Figure 5.5: Influence of the revolutionpitch on the temperature distribution

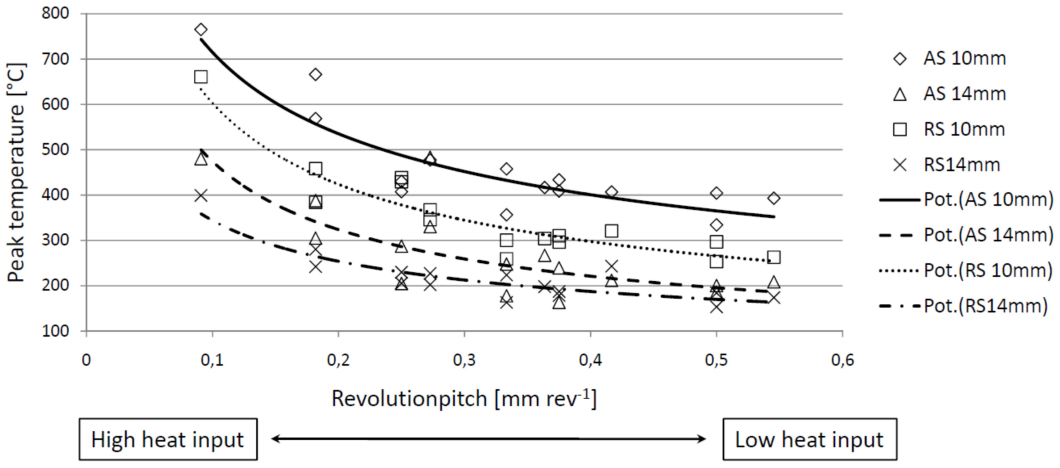

Figure 5.6: Peak temperatures plottet over revolutionpitches. $F_z = 19\,kN$

5.2.2 Influence of the Down Force on the Temperature Pattern

As shown in Table 4.3 only a few welds were performed both at $19kN$ and $24kN$ with other parameters being identical. Thus, only a limited statement for a rather narrow parameters range could be made for the influence of different down forces. However, a trend certainly was observed. The results of the temperature measurements for different revolutionpitches and down forces are summarized in Tables 5.2 and 5.3. In any case the temperatures increased significantly by increasing the down force from 19 to $24\,kN$ due to higher friction. It is not surprising therefore, that the highest temperature was measured for the lower revolutionpitch at the higher down force on advancing side close to the weld.

Force $[kN]$	AS $10\,mm\,[°C]$	AS $14\,mm\,[°C]$	RS $10\,mm\,[°C]$	RS $14\,mm\,[°C]$
19	393	208	263	174
24	555	308	279	199

Table 5.2: Maximum temperatures at different forces. $Revpitch = 0.5\,mm\,rev^{-1}$

Force $[kN]$	AS $10\,mm\,[°C]$	AS $14\,mm\,[°C]$	RS $10\,mm\,[°C]$	RS $14\,mm\,[°C]$
19	404	200	296	184
24	696	403	588	364

Table 5.3: Maximum temperatures at different forces. $Revpitch = 0.25\,mm\,rev^{-1}$

5.3 Mechanical Properties

The mechanical properties were assessed by using tensile testing and hardness mesurements. While tensile testing was conducted for each parameter set, hardness testing was only carried out for selected samples.

5.3.1 Tensile Properties

The main target of tensile testing was the determination of a range of welding parameters that led to welds with most favorable mechanical properties. This parameter optimization was carried out for a down force of $19\,kN$ over a wide range of tool rotation speeds and welding speeds. Furthermore, the general influence of different revolutionpitches on the tensile properties as well the influence of an increase in down force were investigated.

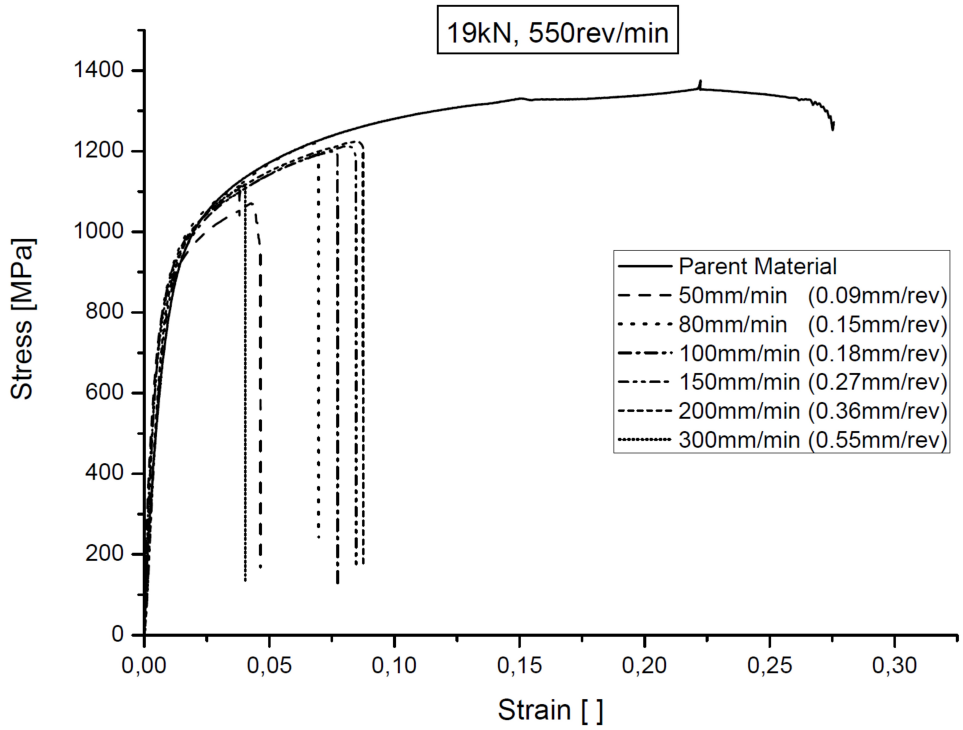

Figure 5.7: Influence of the revolutionpitch on the tensile properties

5.3.1.1 Influence of the Revolutionpitch on the Tensile Properties

Figure 5.7 shows the results of tensile tests for different welding speeds at a constant tool rotation speed of $550\,rev\,min^{-1}$ and a steady down force of $19\,kN$. For the lowest welding speed of $50\,mm\,min^{-1}$ $(0.09\,mm\,rev^{-1})$* a tensile strength of $1070\,MPa$ and a fracture elongation of at least $4.7\,\%$ were reached. By increasing the welding speed, the tensile properties were improved, having their maximum at a welding speed of $200\,mm\,min^{-1}$ resulting in a tensile strength of $1220\,MPa$ and a fracture elongation of $8.5\,\%$. However, by further increasing the welding speed to $300\,mm\,min^{-1}$ $(0.55\,mm\,rev^{-1})$ the strength and ductility of the joint dropped to $1100\,MPa$ in ultimate tensile strength and $4\,\%$ in maximum elongation. In short, it was demonstrated that the welding speed, respectively the revolutionpitch, played a dominant role for the weld quality by directly influencing the heat input.

5.3.1.2 Influence of the Down Force on the Tensile Properties

Figure 5.8 shows the results of tensile tests for different welding speeds at down forces of $19\,kN$ and $24\,kN$ at a constant tool rotation speed of $400\,rev\,min^{-1}$. For a down force of $19\,kN$ the results were twofold. At a welding speed of $100\,mm\,min^{-1}$ $(0.25\,mm\,rev^{-1})$

*Numbers in brackets refer to the revolutionpitch

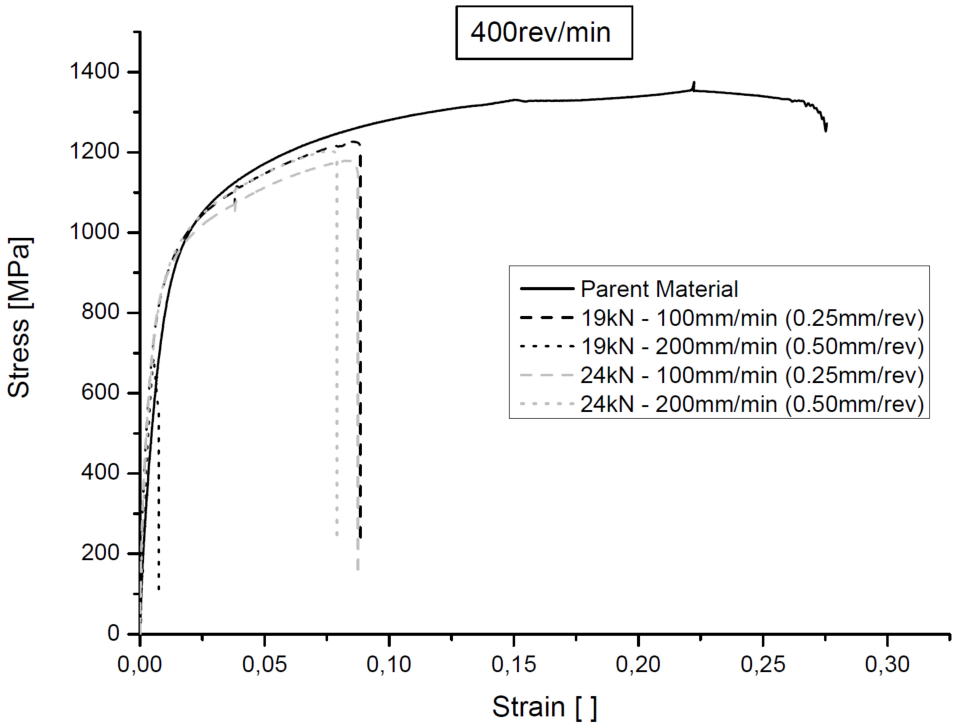

Figure 5.8: Influence of the down force on the tensile properties

an ultimate tensile strength of 1220 MPa and a fracture elongation of about 8.8 % were reached, whereas for an increased welding speed of 200 $mm\,min^{-1}$ (0.5 $mm\,rev^{-1}$) the tensile properties dropped to 720 MPa in tensile strength and 1.5 % in maximum elongation. Compared to that, at a down force of 24 kN the tensile properties were slightly reduced for a welding speed of 100 $mm\,min^{-1}$, while they were significantly improved for a welding speed of 200 $mm\,min^{-1}$ leading to a tensile strength of 1190 MPa and a fracture elongation of 7.5 %.

Owing to that, it could be deduced that not only the revolutionpitch but also the down force played an important role for the weld quality, especially when it came to welds with a high revolutionpitch. This consideration was confirmed when comparing the macrostructures of welds with a revolutionpitch of 0.5 $mm\,rev^{-1}$ at different down forces, as illustrated in Figures 5.9 and 5.10. The combination of a high revolutionpitch and a rather low down force apparently led to a large number of weld defects within the stir zone. However, by applying a higher forging force and thereby increasing the process temperatures the pores that occurred for a down force of 19 kN could be avoided resulting in enhanced mechanical properties.

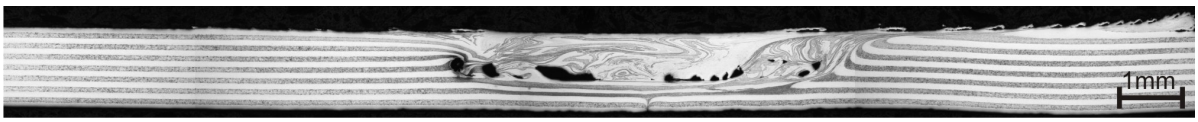

Figure 5.9: Weld cross section. $Revpitch = 0.5\,mm\,rev^{-1}$, $F_z = 19\,kN$

Figure 5.10: Weld cross section. $Revpitch = 0.5\,mm\,rev^{-1}$, $F_z = 24\,kN$

5.3.1.3 Range of Optimized Parameters

In Figure 5.11 a summary of the results of tensile tests for all investigated parameter combinations is given. The tensile properties ranged from a low level of 690 MPa in tensile strength and 1.5 % fracture elongation to a maximum level of 1240 MPa in tensile strength and 13 % elongation. Samples that fractured at stress levels higher 1175 MPa and at elongations exceeding 8 % are represented by filled diamonds, all others are represented by empty diamonds. Ultimate tensile strengths exceeding 1175 MPa refer to an excellent joint efficiency higher 85 %, as the term joint efficiency is known as the ratio of the joint tensile strength to the tensile strength of the parent material. The matrix of welding parameters in Figure 5.12 illustrates the range of revolutionpitches that created those most favorable results. Apparently, joint efficiencies higher 85 % were achieved over a wide range of tool rotation speeds at revolutionpitches ranging from $0.25\,mm\,rev^{-1}$ to about $0.4\,mm\,rev^{-1}$. In terms of productivity it is worth mentioning that this criterion was also reached for a high welding speed of $500\,mm\,min^{-1}$.

The optimal tensile properties were found for a tool rotation speed of $800\,rev\,min^{-1}$ and a welding speed of $200\,mm\,min^{-1}$ ($0.25\,mm\,rev^{-1}$), resulting in an ultimate tensile strength of 1240 MPa and a fracture elongation of 13 %. That equaled a joint efficiency of 90 % according to strength and about 50 % of the fracture elongation of the parent metal. A comparison of the stress-strain curve of an optimized parameters weld to that of the parent material is given in Figure 5.13. For the optimized parameter set fracture occured in HAZ on RS, as for all samples exceeding 85 % joint efficiency (Figure 5.14). All other samples fractured in the region of the stir zone (SZ) with or without previous necking in HAZ-RS or SZ. Fracture or necking on the advancing side (AS) has not been observed in any case. Figure 5.15 illustrates the systematic fracture behavior for different heat input. Low heat input welds (a) fractured in the center of SZ without necking, welds with medium heat input (b) fractured in HAZ-RS after necking, and high heat input welds (c) fractured in SZ with previous necking on RS.

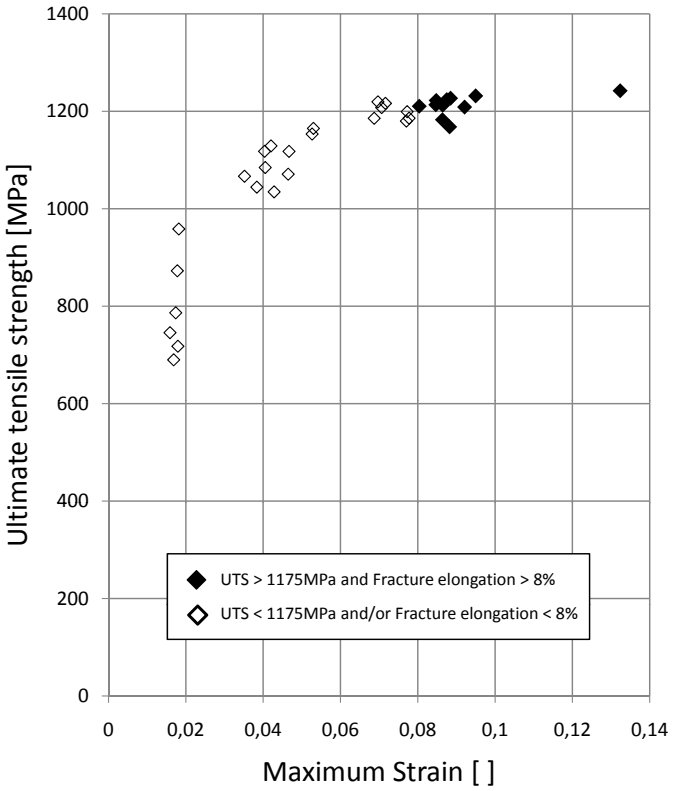

Figure 5.11: Summary of the tensile properties of all parameter sets

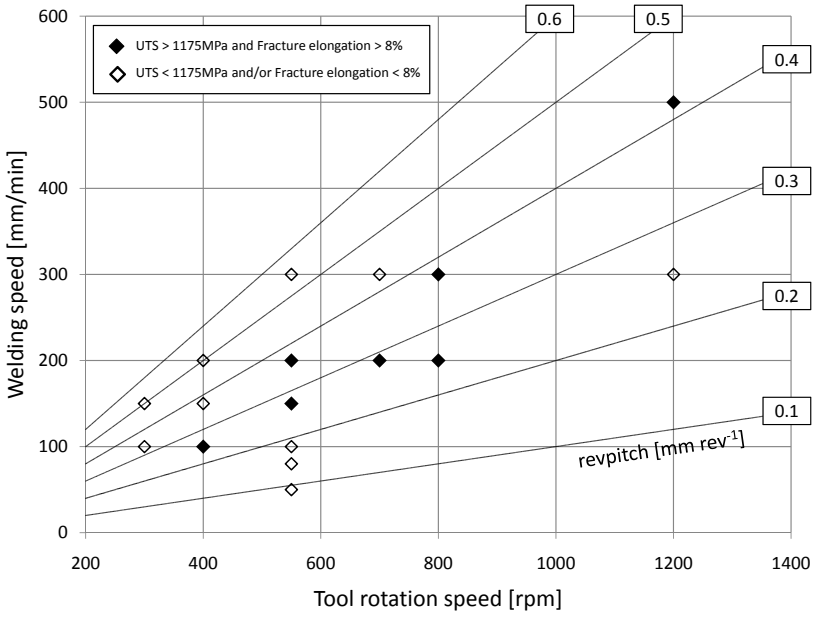

Figure 5.12: Matrix of welding parameters and revolutionpitches

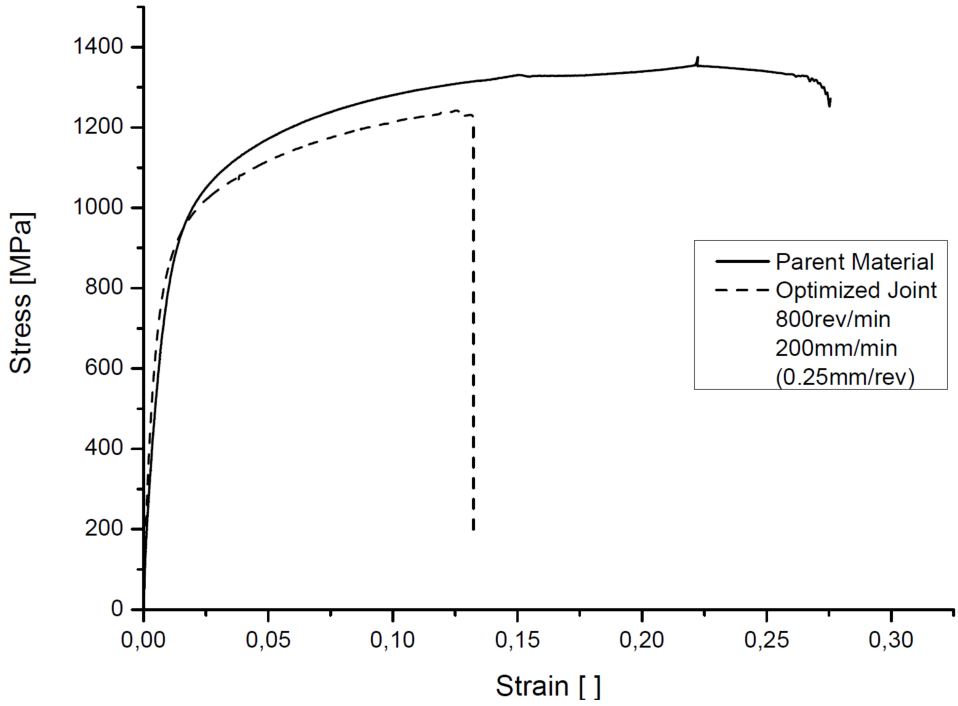

Figure 5.13: Tensile properties of an optimized joint compared to the parent material

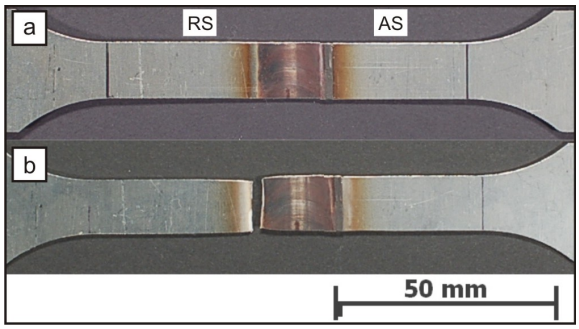

Fracture in HAZ-RS ($UTS > 1175\,MPa$, fracture elongation $> 8\,\%$)

Figure 5.14: Tensile test sample. (a) before testing; (b) fractured sample

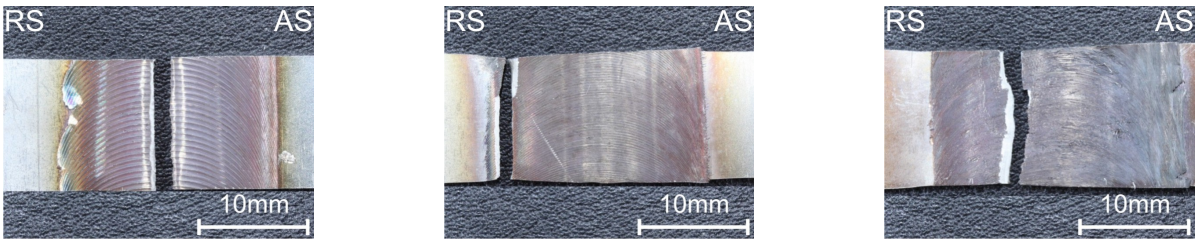

(a) $0.55\,mm\,rev^{-1}$ (b) $0.25\,mm\,rev^{-1}$ (c) $0.09\,mm\,rev^{-1}$

Figure 5.15: Systematic fracture behavior for different revolutionpitches

5.3.2 Hardness Measurements

The primary purpose of hardness testing was the creation of hardness patterns across the weld seam in order to identify possible changes in hardness in different weld zones. Moreover, it was aimed for a systematic connection between the hardness profile and the revolutionpitch.

Figure 5.16 illustrates the hardness measuring approach. Measurements were carried out across the whole weld seam with a resolution of about $200\,\mu m$. Linear measurements were feasible in parent material, heat affected zone, and in the main part of thermo-mechanically affected zone. Due to the mixing of the layers in stir zone, however, the measurements in this region had to be carried out in appropriate regions of either SUS301 or SUS402J2.

The hardness of the parent material equaled about $315\,HV0.1$ in layers of SUS301 and $550\,HV0.1$ in layers of SUS420J2. Figure 5.17 shows the hardness profile across the weld in middle layers of both austenitic SUS301 and martensitic SUS420J2 for the optimized parameters with a revolutionpitch of $0.25\,mm\,rev^{-1}$ resulting from a tool rotation speed of $800\,rev\,min^{-1}$ and a welding speed of $200\,mm\,min^{-1}$.

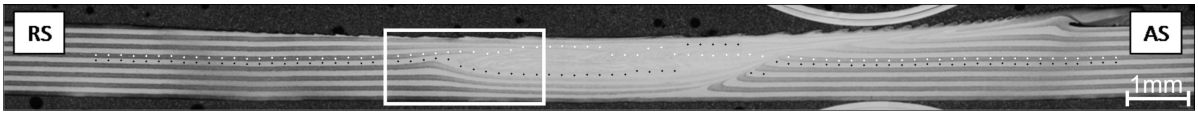

(a) Overview

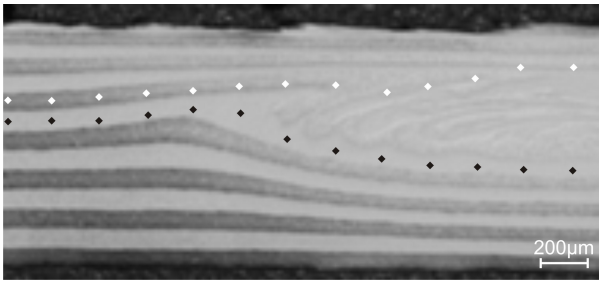

(b) Detailed view of TMAZ/SZ on RS
White diamonds...SUS301
Black diamonds...SUS420J2

Figure 5.16: Illustration of the hardness measurement approach

For the austenitic layer no significant deviation from the hardness level of the parent material could be detected. A slight decrease in hardness towards the weld center with a minimum of 259 $HV0.1$ was observed, no differences between the advancing side and retreating side were noticed. The maximum measured hardness in austenitic zones equaled 321 $HV0.1$.

The hardness profile in the martensitic layer, in contrast, showed strong deviations from the hardness of the parent material. Beside the weld seam, the hardness of the parent material was reached, whereas in the heat affected zone (HAZ) a well pronounced hardness drop could be detected on both the advancing and retreating side. The minimum measured hardness was similar on both sides equaling 339 $HV0.1$ on AS and 354 $HV0.1$ on RS, and also the width of HAZ did not differ significantly from one side to the other. However, asymmetry was observed, that is, the HAZ on RS was closer to the weld center than the HAZ on AS. In the thermomechanically affected zone (TMAZ) the hardness rose steadily from HAZ towards SZ on both sides, whereas the increase was more steady and quick on AS in any case. The maximum hardness was measured within the stir zone (SZ) equaling a value of 687 $HV0.1$.

In Figure 5.18 a comparison of the hardness profiles in martensitic layers for minimum and maximum heat input as well as for the optimized parameters is given. A rather systematic behavior could be observed when comparing the profiles. Apparently, the HAZ was shifted further away from the weld center with increasing heat input, whereas in any case the HAZ on RS was closer to the center than on AS. This asymmetry could be explained by comparing the hardness profile in Figure 5.18 to the temperature cycles in Figure 5.5. The hardness profile for highest heat input together with the correlating temperature cycles (Figure 5.5 d) pointed out that the critical temperatures that led to the formation of the soft HAZ must have been around $750°C$, since these temperatures were measured in HAZ on AS at $10\,mm$ distance from the weld center. In any other case those high temperatures could not be observed. Thus, all the other heat affected zones were shifted towards the weld center, to locations where the critical temperatures could be reached. Consequentially, the HAZ on RS for the lowest heat input was the one closest to the weld center, and the HAZ on AS for the highest heat input was the one farthest away from the weld center. Furthermore, it could be noticed that the average hardness in SZ for highest heat input was only 575 $HV0.1$ compared to 650 $HV0.1$ for lower heat input. It was considered that a lower cooling rate for high heat input welds was responsible for this circumstance.

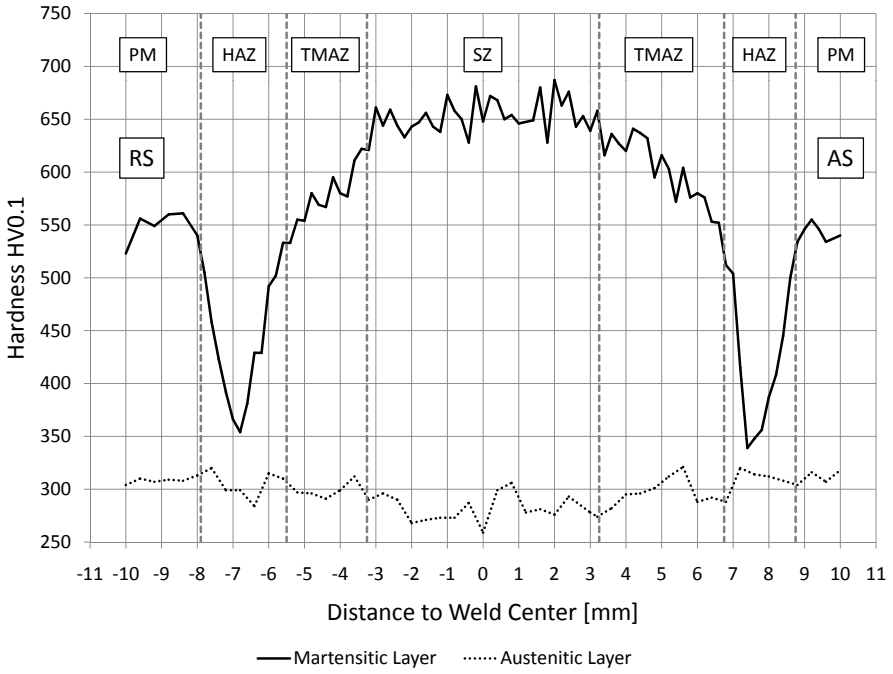

Figure 5.17: Hardness profile across the weld seam for optimized parameters

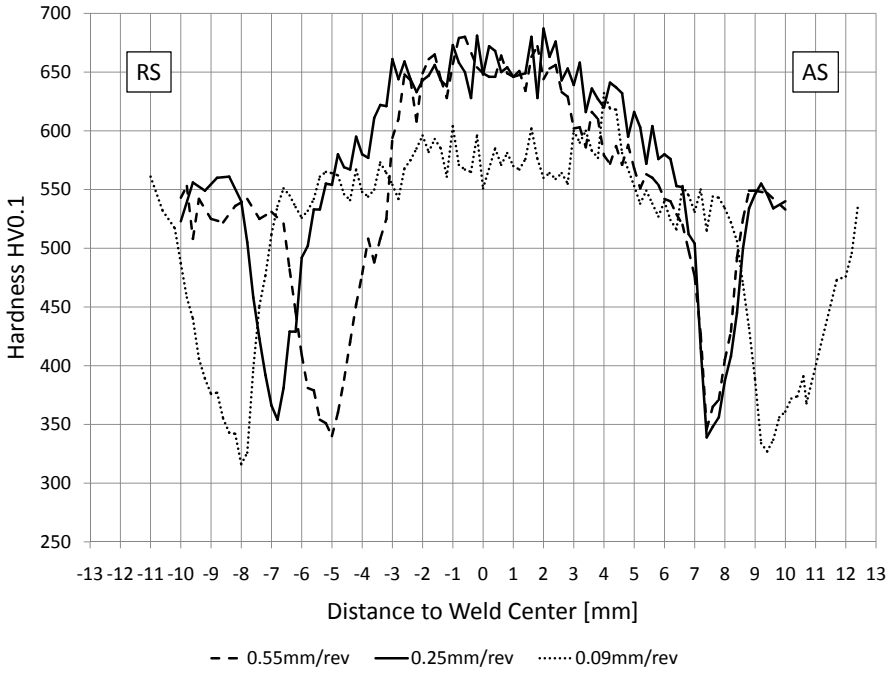

Figure 5.18: Hardness profiles in SUS420J2 for different heat input

5.4 Metallography

In this section the results of different metallographic investigations are presented. Based on previous results in this study the systematic approach of differentiation according to the revolutionpitch was continued. Accordingly, investigations on the fracture behavior and on the microstructure were carried out for low heat input welds ($0.55\,mm\,rev^{-1}$), high heat input welds ($0.09\,mm\,rev^{-1}$), as well as for welds with optimized parameters ($0.25\,mm\,rev^{-1}$). In addition, very detailed analyses were conducted for an optimized parameters weld in order to assess the microstructural response to the welding process in different weld regions.

5.4.1 Low Heat Input Welds

In Figure 5.19 an electro-chemically etched optical macrograph of a low heat input weld with a revolutionpitch of $0.55\,mm\,rev^{-1}$ is given. As in all cross section figures of this study the right side refers to AS and the left side refers to RS. It is shown that due to low heat input, the deterioration of the layered structure was limited to a narrow region within SZ, while the laminated composition was sustained in all other weld regions. However, a large number of weld defects has been observed in and around SZ, as highlighted in the macrograph, including pores and incomplete consolidation at the root. Figure 5.20 shows detailed SEM and EBSD images of the occurring defects, whereas the left column (a) shows images of the retreating side of SZ, the center column (b) demonstrates defects at the root, and the right column (c) refers to the advancing side of SZ. Pores, amongst which the largest ones had a diameter of more than $10\,\mu m$ emerged both on RS and AS in SZ in regions close to the pin edges, presumably caused by inadquate plastification due to insufficient heat input. The most pronounced pores are illustrated by EBSD images, whereas green grains refer to fcc-structure and red grains refer to bcc-structure, respectively. The presence of pores in SZ of low heat input welds has also been reported in previous studies.[34] Moreover, as demonstrated in the center column of Figure 5.20, the root was not fully consolidated which was also considered as a result from insufficent plastification.

Figures 5.21, 5.22, and 5.23 demonstrate the fracture behavior of low heat input welds. Typically, tensile specimen of welds with high revolutionpitches, as shown in the macro photo in Figure 5.21, fractured in the weld center at rather low stress levels and with only limited elongation. Furthermore, virtually no necking was noticed. From the SEM images of the fracture surface in Figure 5.22 it could be deduced that weld defects occurred all along the weld seam. Since pores were also observed in the weld cross section (Figure 5.20), it was considered that the illustrated pores were running on circular paths around the tool probe as it proceeded along the weld. However, since fracture occurred

directly in the center of SZ without necking, as illustrated in the fracture path in Figure 5.23, the phenomenon of brittle fracture for low heat input welds was attributed to the presence of weld defects in the weld center, whereas it was assumed that fracture initiated from the incomplete root.

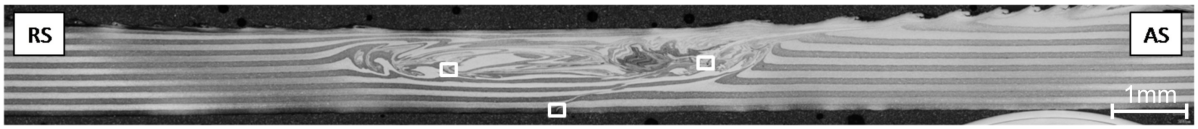

Figure 5.19: Low heat input weld optical macrograph

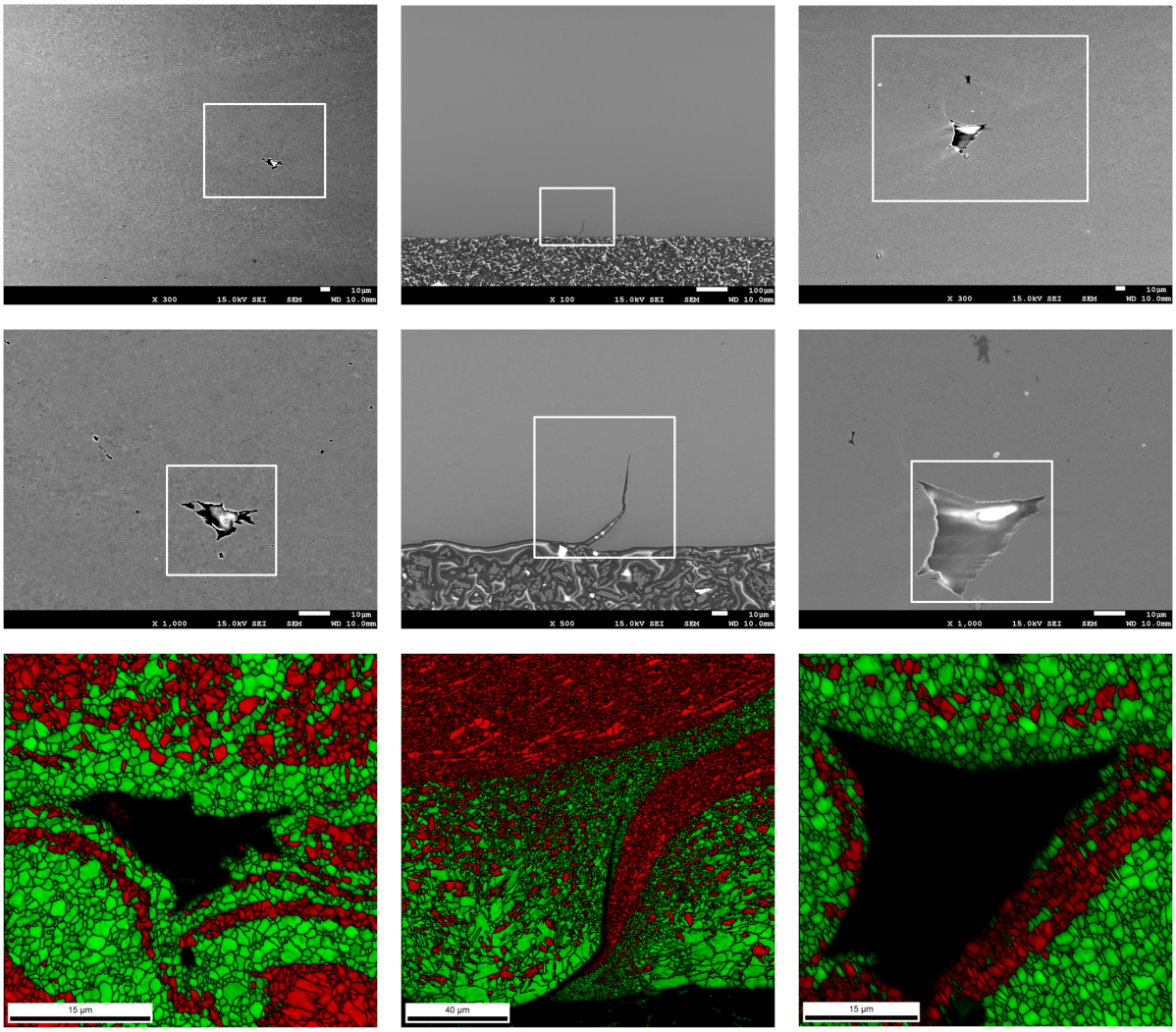

(a) Pores in SZ on RS (b) Incomplete root (c) Pores in SZ on AS

Figure 5.20: SEM and EBSD images of weld defects in a low heat input weld

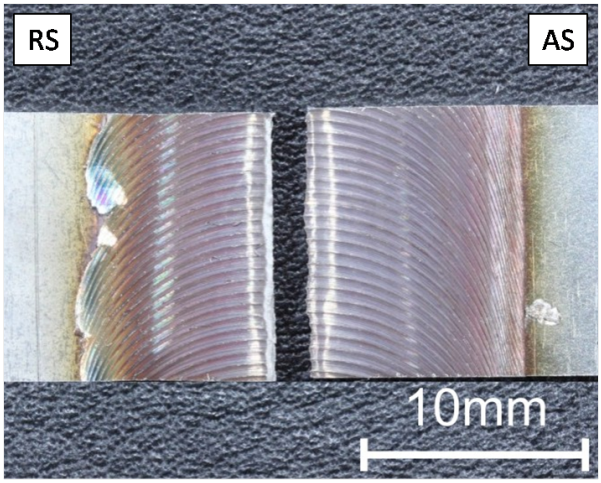

Figure 5.21: Fractured tensile specimen of a low heat input weld

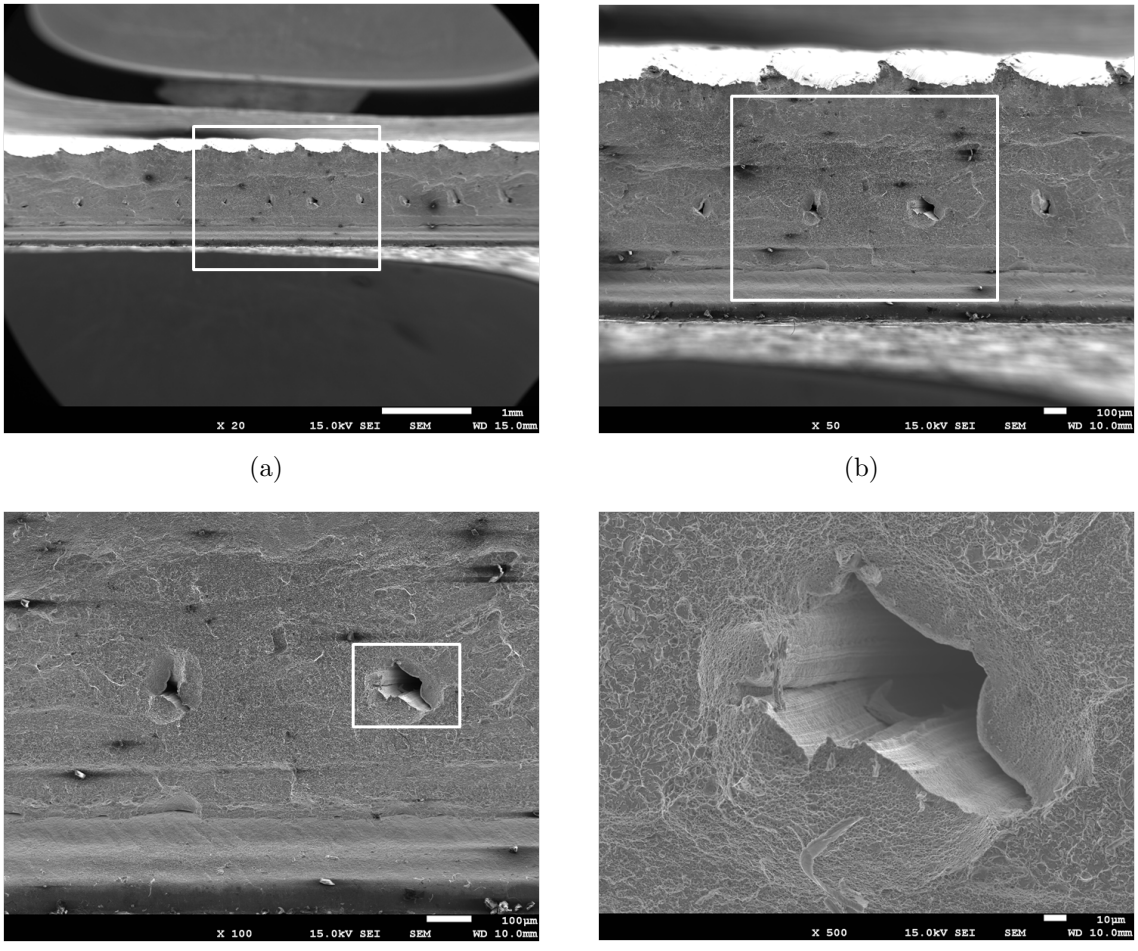

(a) (b)

(c) (d)

Figure 5.22: Fracture surface in SZ of a low heat input weld

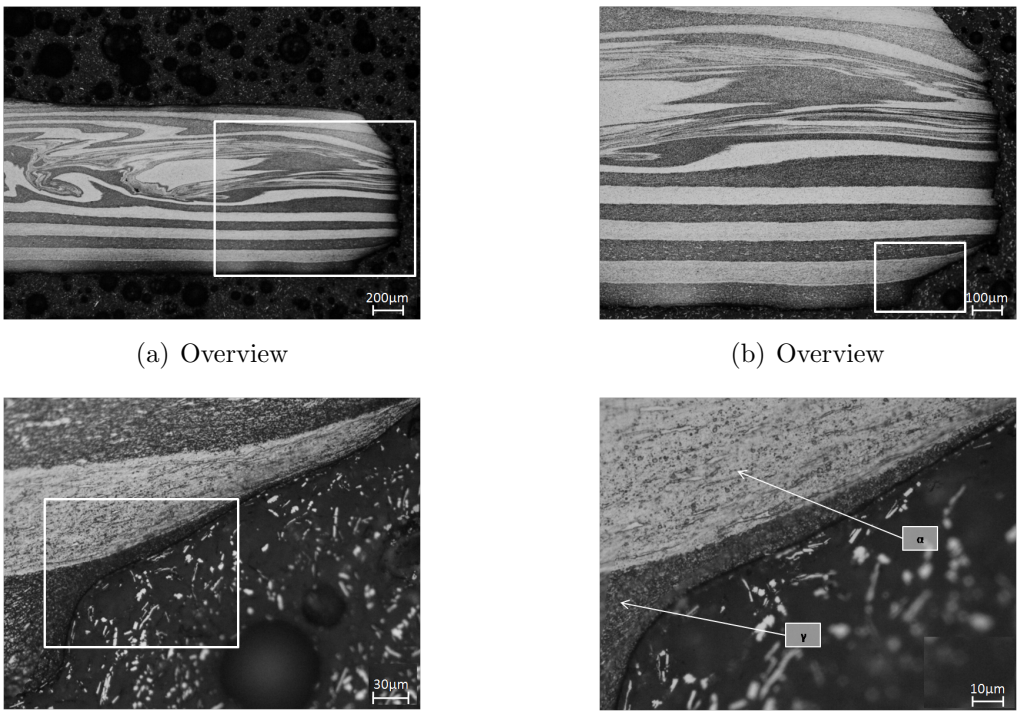

(a) Overview

(b) Overview

(c) Incomplete root

(d) Incomplete root

Figure 5.23: Fracture path of a low heat input weld

5.4.2 High Heat Input Welds

Figure 5.24 shows the cross section of a high heat input weld with a revolutionpitch of $0.09\,mm\,rev^{-1}$ in electro-chemically etched condition. A comparison of this cross section to the one of the low heat input weld in Figure 5.19 pointed out differences in the size and shape of SZ due to varied heat input. Numerically expressed, the width of SZ in the middle of the welded sheets equaled only $5.9\,mm$ for a revolutionpitch of $0.55\,mm\,rev^{-1}$, while SZ was widened to $11.4\,mm$ for a revolutionpitch of $0.09\,mm\,rev^{-1}$. Consequentially, the deterioration of the layered structure was much more pronounced for welds with high heat input, as evidenced from Figure 5.24. In addition to structural impairment, another unfavorable effect emerged by decreasing the revolutionpitch. Due to high heat input, softened material was pushed away from the weld center leading to considerable thinning of the weld cross section. This behavior was only observed on a low scale for higher revolutionpitches. In figures, the minimum thickness for a revolutionpitch of $0.55\,mm\,rev^{-1}$ equaled $1.13\,mm$ compared to a much lower value of $1.02\,mm$ for a revolutionpitch of $0.09\,mm\,rev^{-1}$. As a consquence, under same tensile load this reduction in thickness would lead to an increase in tensile stress of about $10\,\%$.

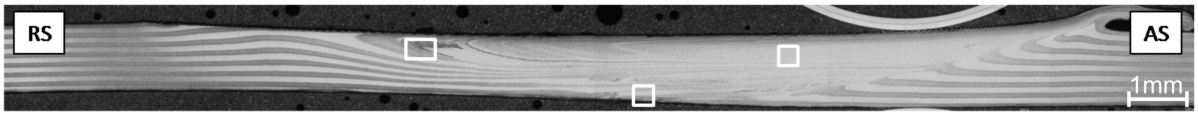

Figure 5.24: High heat input weld optical macrograph

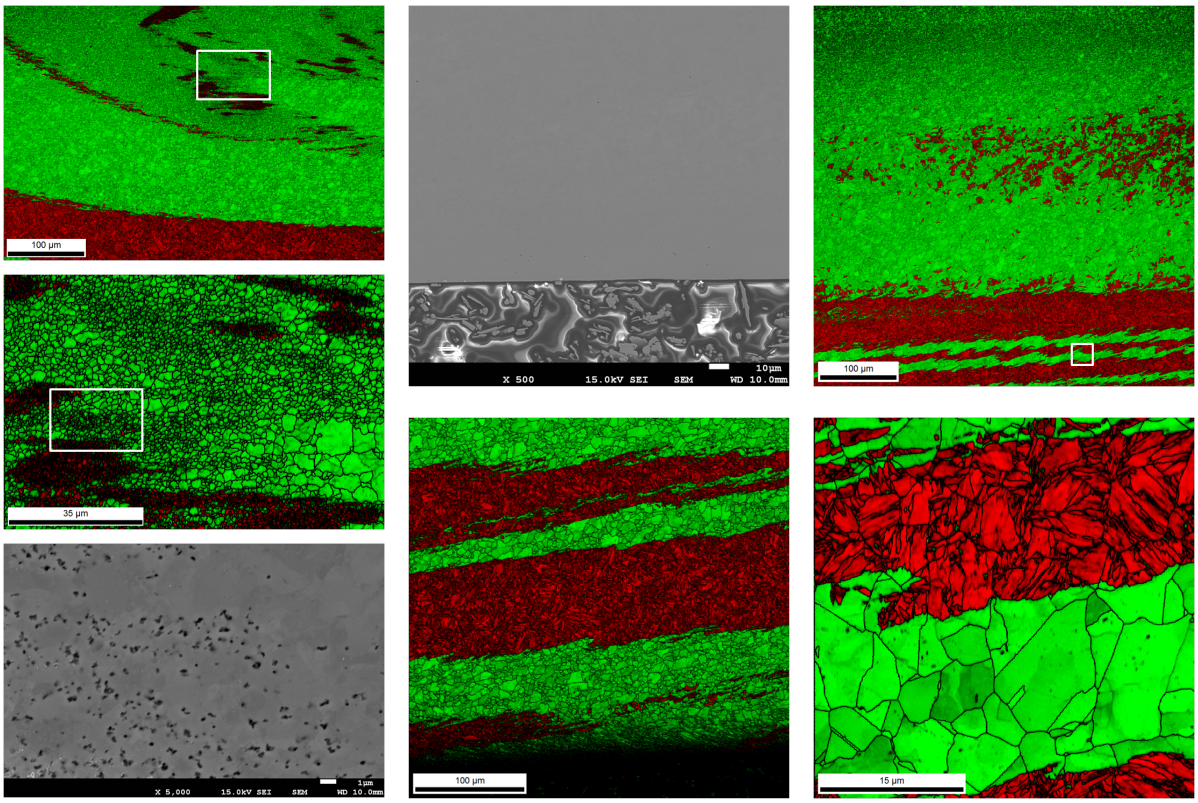

(a) Pores in SZ (b) Complete root (c) SZ center

Figure 5.25: SEM and EBSD images of a high heat input weld

Figure 5.25 gives detailed insight in the microstructural response to high heat input by means of SEM and EBSD. In regions of highly distorted layers in upper zones of the weld a large number of pores with a diameter smaller $1\,\mu m$ was detected, as illustrated in the left column (a). Since this behavior was only observed for welds with a very low revolutionpitch, it was attributed to the intense stirring at very high temperatures in regions close to the tool shoulder. The middle column (b) represents the region around the former edges of the welded sheets. Unlike for a revolutionpitch of $0.55\,mm\,rev^{-1}$, where the root was clearly not fully consolidated, no indications of incomplete welding were detected for a revolutionpich of $0.09\,mm\,rev^{-1}$. Rather, even in regions close to the root highly deformed layers were observed. The right column (c) shows the microstructure in the center of SZ. Apparently, in some regions the layered structure was completely

destroyed resulting in large zones of fcc-grains (green) with only little fragments of former bcc-layers (red). In other zones of the weld center the layered structure was still identifiable but high deterioration was recognized all over SZ.

The fracture behavior of a weld with a revolutionpitch of $0.09\,mm\,rev^{-1}$ is demonstrated in Figures 5.26, 5.27, and 5.28. Typically for high heat input welds fracture occurred in SZ, whereas previous necking was observed on RS of the weld seam, as illustrated in the macro photo in Figure 5.26. Figure 5.27 shows SEM images of the fracture surface at different magnifications. Due to a high degree of plastification no pores or other weld defects were detected. Instead it was observed, that even for high degrees of deterioration the martensitic layers showed distinct ductility. This ductile behavior was also observed in highly mixed regions, as illustrated in Figure 5.27 (f). This consideration was evidenced from the optical micrographs of a fractured tensile specimen in Figure 5.28 showing a fracture zone deformed under 45°, which is very typical for ductile behavior. As for all electro-chemically etched samples the darker regions represent SUS301 and the lighter regions represent SUS420J2. Apparently, the fracture path in transverse direction proceeded directly through a region of highly distorted layers.

As a consequence, fracture at modest strength levels for high heat input welds was attributed to the coincidence of two phenomenons, namely structural impairment resulting from deterioration of the layers and reduction of the weld cross section within SZ, whereas the latter one was considered most influential.

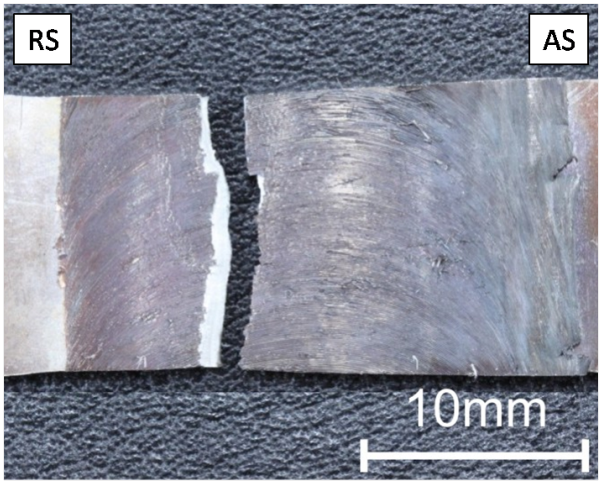

Figure 5.26: Fractured tensile specimen of a high heat input weld

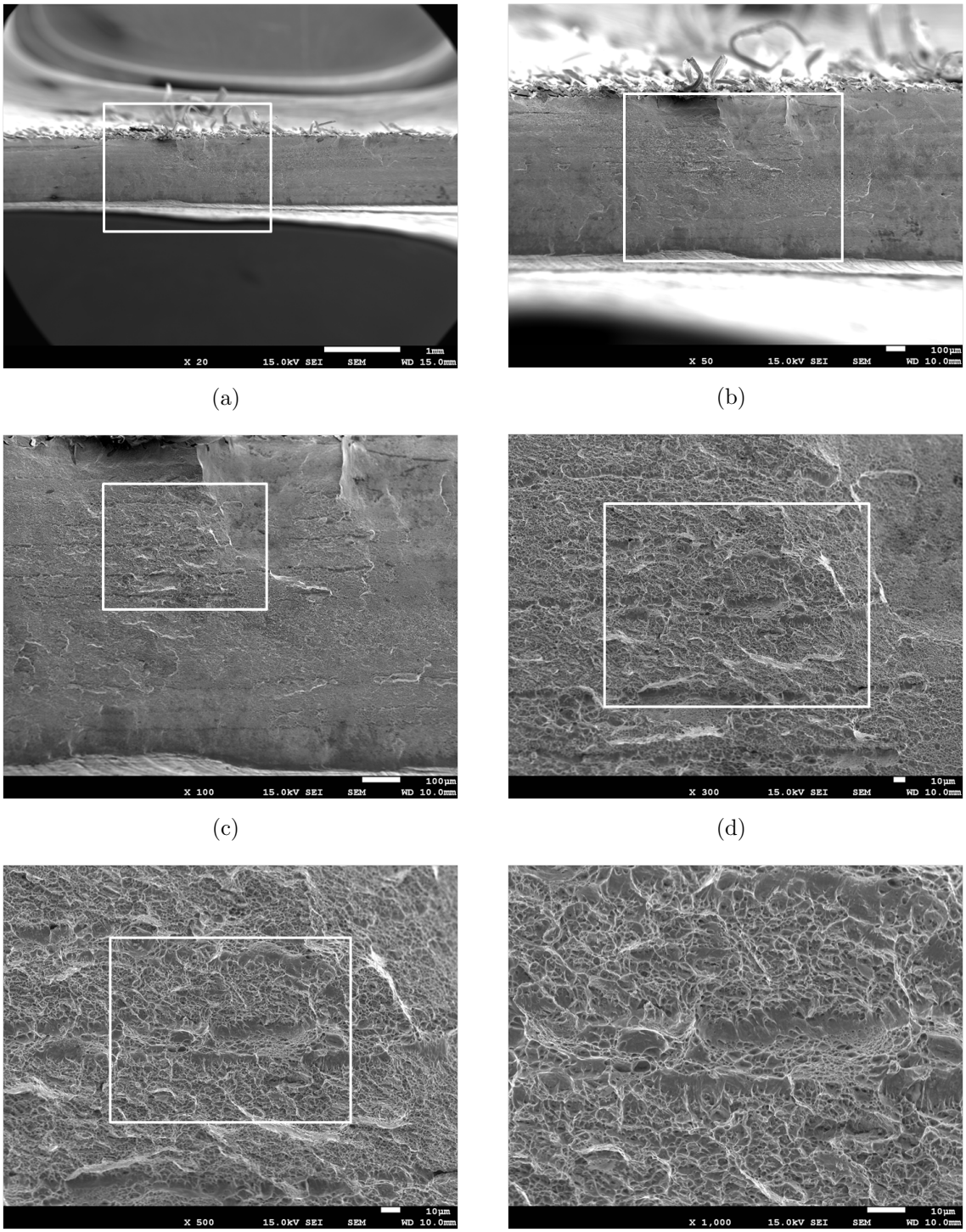

(a) (b)

(c) (d)

(e) (f)

Figure 5.27: Fracture surface in SZ of a high heat input weld

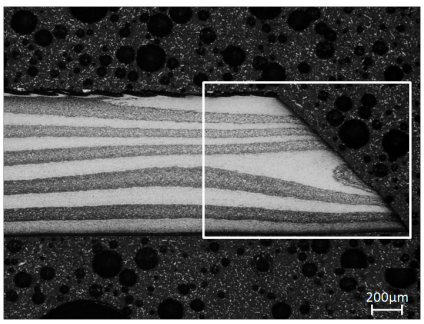

(a) Overview

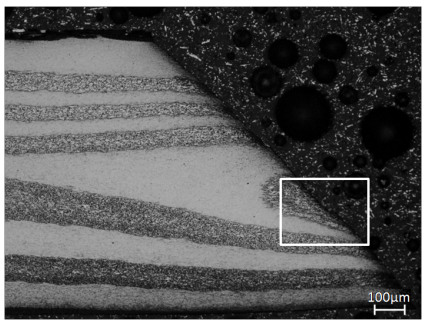

(b) Overview

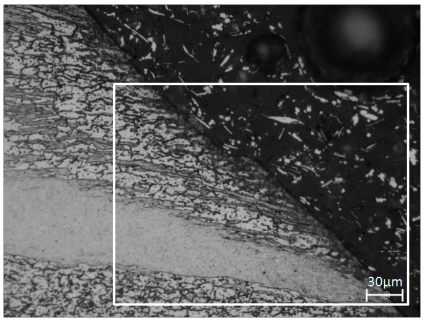

(c) Mixed region

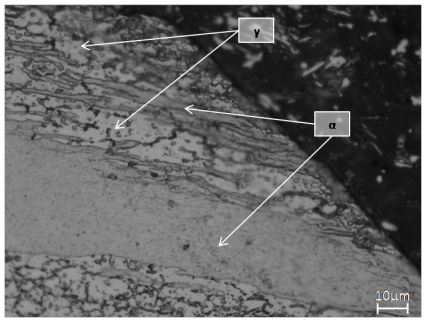

(d) Mixed region

Figure 5.28: Fracture path in SZ of a high heat input weld

5.4.3 Optimized Parameters Welds

Figure 5.29 shows an optical macrograph of the weld cross section of an optimized parameters weld with a revolutionpitch of $0.25\,mm\,rev^{-1}$ resulting from a tool rotation speed of $800\,rev\,min^{-1}$ and a welding speed of $200\,mm\,min^{-1}$. While for low heat input welds a large number of weld defects was detected, and for high heat input welds structural impairment in combination with extensive thinning was observed, neither of those unfavorable effects occurred for the optimized parameter set. In SZ no pores were detected and also the root could be considered fully consolidated, as only a few in weld direction uncontinuous pores with a diameter smaller $1\,\mu m$ reminded of the former edges of the steel sheets, as illustrated in Figure 5.30. As desired, the deterioration of the layers was limited to the center of SZ, whereas the laminated structure was sustained in all other regions, even at bottom layers in SZ. This consideration is evidenced in Figure 5.31 by means of EBSD, where in the lowest layer only green fcc-grains with few remaining red grains of deformation induced martensite were observed. For an optimized weld the width of SZ equaled $6.0\,mm$ in the middle layer, which is only marginally larger than $5.9\,mm$ for the low heat input weld. However, the plastified area was obviously wide enough to avoid the formation of pores within SZ. Certainly the process-related thinning in regions below the tool could not be fully prevented. The sheet thickness steadily

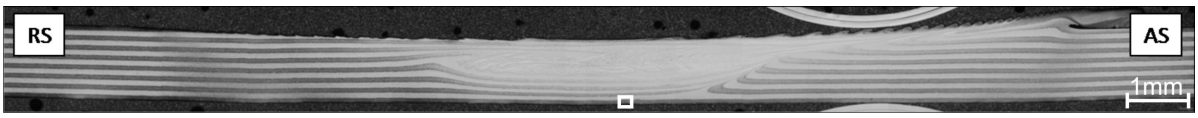

Figure 5.29: Optical macrograph of an optimized weld

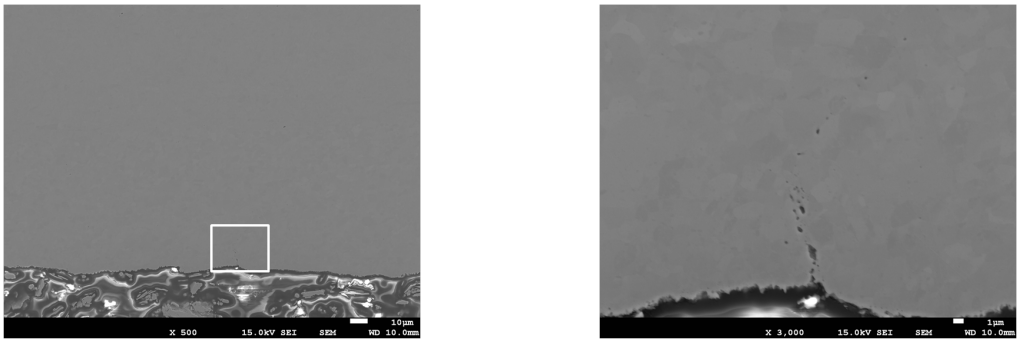

(a) SEM overview (b) SEM detail

Figure 5.30: SEM images of the fully consolidated root

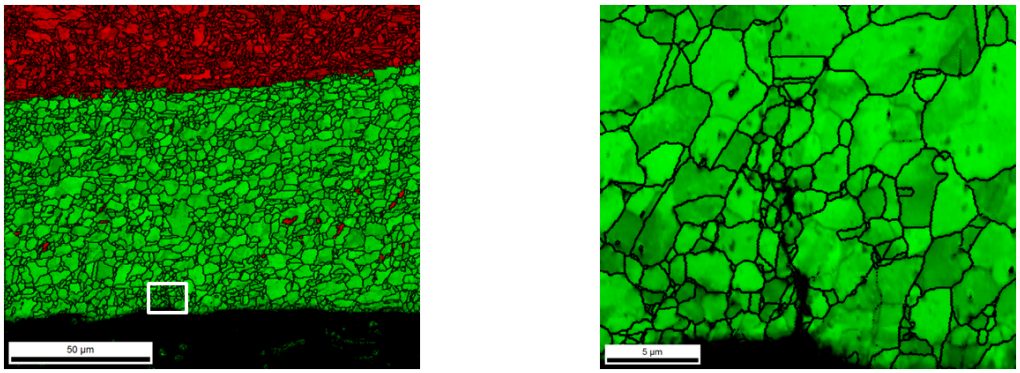

(a) EBSD overview (b) EBSD detail

Figure 5.31: EBSD images of the fully consolidated root

decreased from a value of about 1.2 mm in PM as approaching the weld center, equaling a minimum value of 1.09 mm in SZ. Accordingly, the thinning effect was averagely pronounced compared to high and low heat input welds. As a consequence of those observations it could be summarized as follows: The most favorable tensile properties were achieved if the heat input was just high enough to avoid pores on the one hand and guarantee full consolidation of the root on the other hand. Thereby the structural impairment and the thinning effect were reduced to a possible minimum.

5.4.3.1 Parent Material

Generally, in PM no microstructural modifications are expected due to a lack of both high temperatures and plastic deformation. This behavior was also observed in the present study where neither in SUS301 layers nor in layers of SUS420J2 microstructural changes were noticed. Figure 5.32 shows the microstructure in PM by means of EBSD. Similar to the base material the SUS301 layers showed a mainly austenitic microstructure (green) with grain boundary precipitates, and deformation induced martensite in a typical content range of 20 to 35 % (red). The SUS420J2 layers showed a martensitic/ferritic microstructure (red). Accordingly, the temperatures reached within PM must have been below the critical temperatures of about $750°C$ that led to the formation of the weak HAZ. Indeed, by comparing the temperature cycle in Figure 5.5 (c) to the hardness profile in Figure 5.17 it could be deduced that the maximum temperatures measured within PM close to HAZ reached about $500°C$ for a revpitch of $0.25\,mm\,rev^{-1}$.

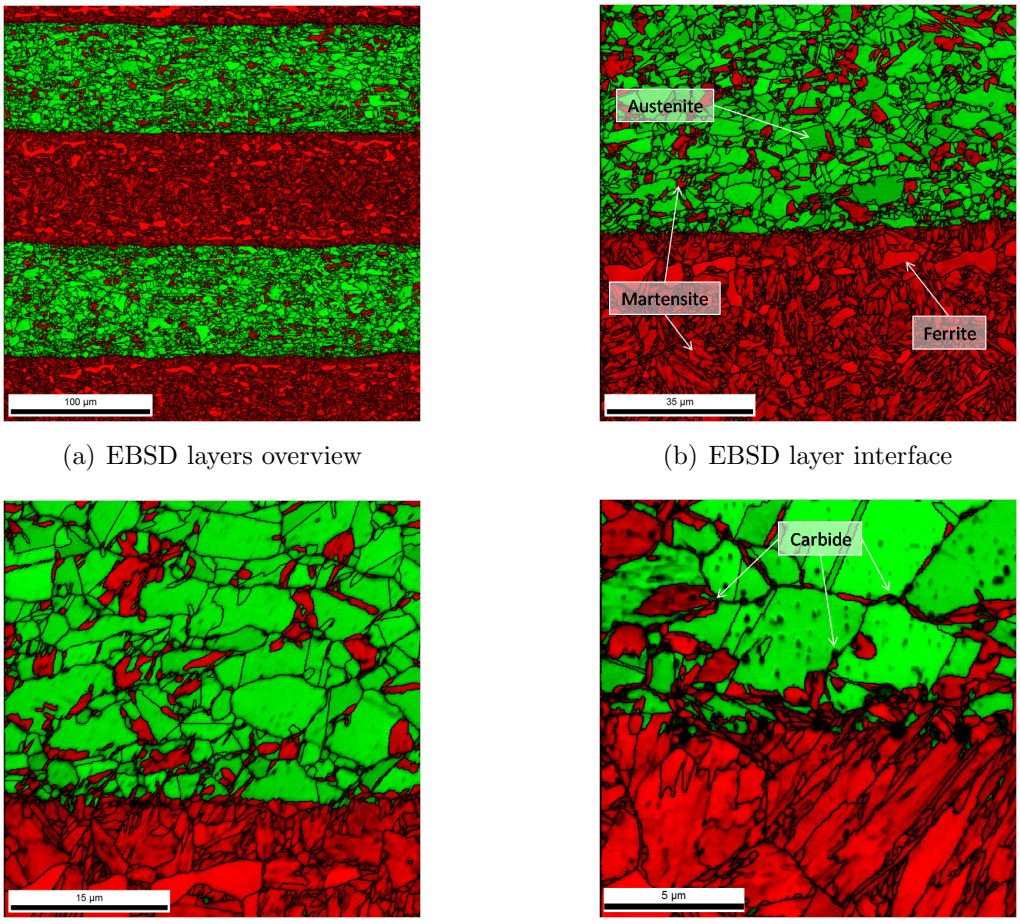

(a) EBSD layers overview

(b) EBSD layer interface

(c) EBSD interface detail

(d) EBSD interface detail

Figure 5.32: Microstructure characterization in PM

5.4.3.2 Heat Affected Zone

Unlike in PM, where no changes in microstructure were noticed, modifications were certainly expectected within HAZ, particularly in layers of SUS420J2 due to the very pronounced hardness drop in martensitic regions. Figure 5.33 shows a microstructural overview and detailed EBSD images of the interface between SUS301 layers (mainly green) and SUS420J2 layers (red) within HAZ. From the micrographs no major microstructural modifications were observed in layers of SUS301. Similar to PM, the layers showed a mainly austenitic microstructure with $M_{23}C_6$ grain boundary precipitates, and also the amount of deformation induced martensite remained in the typical range of 20 to 35 %. These microstructural similarities showed good correlation to the hardness measurement, where no significant deviation from the hardness level of the base material was noticed for SUS301 layers in HAZ.

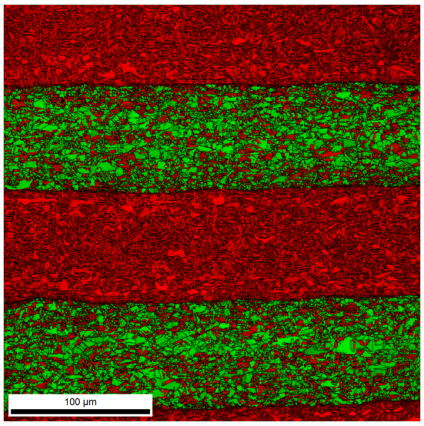

(a) EBSD layers overview

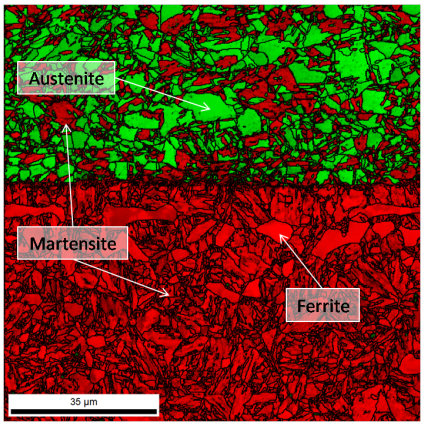

(b) EBSD layer interface

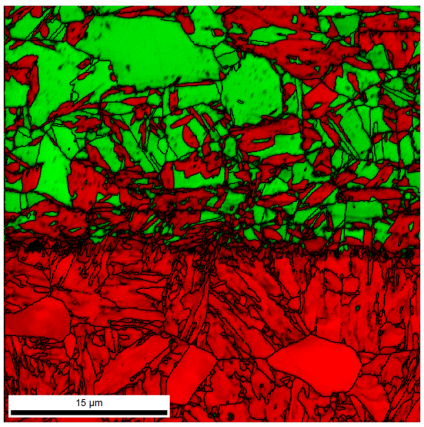

(c) EBSD interface detail

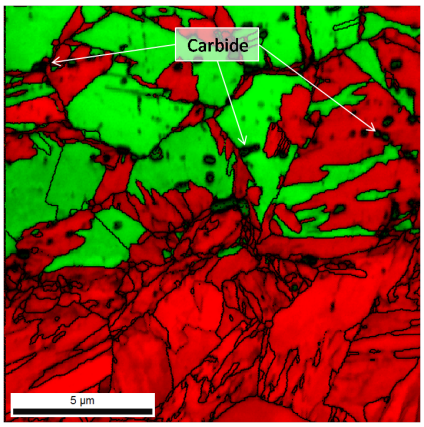

(d) EBSD interface detail

Figure 5.33: Microstructure characterization in HAZ

However, surprisingly no microstructural changes were noticed in SUS420J2 layers from the EBSD images of the interface. Even at rather high magnifications a comparison of the alpha layers in HAZ and PM did not show any striking differences, as shown in Figures 5.34 and 5.35. In both figures the left side refers to the α-layer as observed in PM, whereas the right side demonstrates the α-layer in HAZ. As illustrated, the SUS420J2 showed a similar martensitic/ferritic microstructure in PM (a) as well as in HAZ (b), even though the hardness values differed significantly from one weld region to the other. Since no microstructural explanation for the hardness drop was found with EBSD, the problem needed to be investigated by different metallurgical methods.

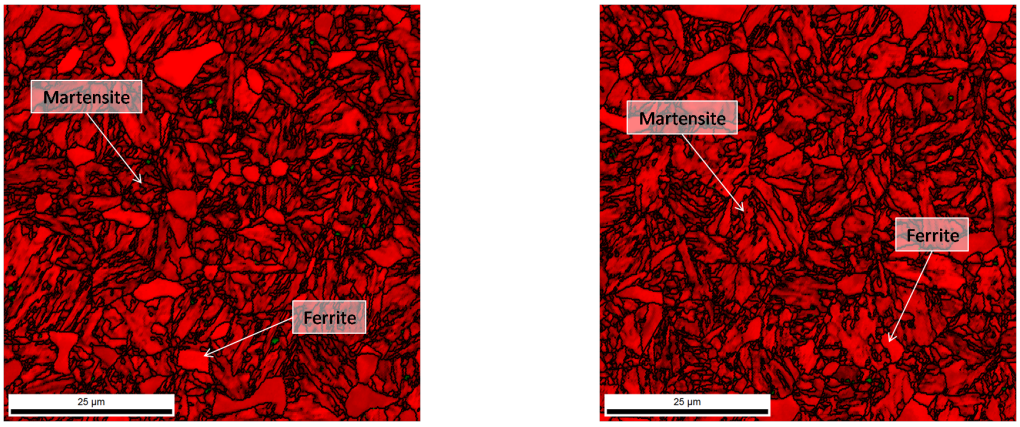

(a) α-layer in PM (b) α-layer in HAZ

Figure 5.34: Comparison of EBSD images of SUS420J2 in PM and HAZ

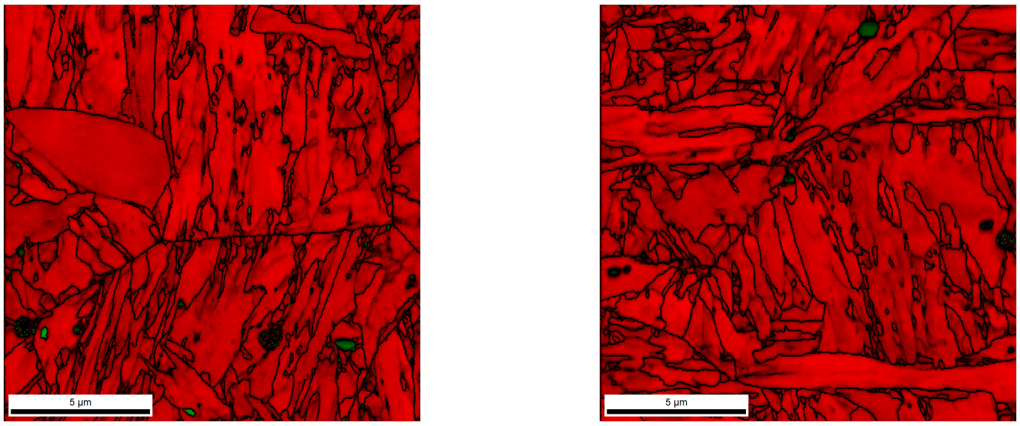

(a) α-layer in PM (b) α-layer in HAZ

Figure 5.35: Detailed EBSD images of SUS420J2 in PM and HAZ

Another approach that was followed in order to identify possible microstructural modifications within HAZ was etching. Figure 5.36 shows electro-chemically etched optical micrographs of the α-layers in PM (a) and in HAZ (b). While the SUS420J2 layers showed the characteristic martensitic/ferritic microstructure in PM, a rather different appearance was observed in HAZ. Apparently, the etching attack was much stronger at the grain boundaries in HAZ than it was in PM. Typically very pronounced grain boundaries are an indication for the presence of grain boundary precipitates. Since no precipitates could be observed from EBSD images, it was assumed that if particles existed their size would be in a very small diameter range.

As the next step therefore, transmission electron microscopy was used, since TEM is known for its ability to visualize particles even in nanometer range. Indeed, by using TEM it was possible to detect a large number of precipitates within HAZ of α-layers. The outcome of the TEM investigations at magnifications ranging from 30 000 x to 100 000 x is demonstrated in Figures 5.37 and 5.38. The dark spots in the images represent precipitates, whereas the light regions represent grains. Evidently, the particles were aligned at the grain boundaries which complies quite well with the considerations derived from the LOM images. At 100 000 x magnification (Figure 5.38) it was even possible to detect rather small precipitates at the martensitic grain boundaries. The size of the particles ranged from about 10 to 80 nm. According to common literature the precipitates were most likely identified as $M_{23}C_6$ carbides.

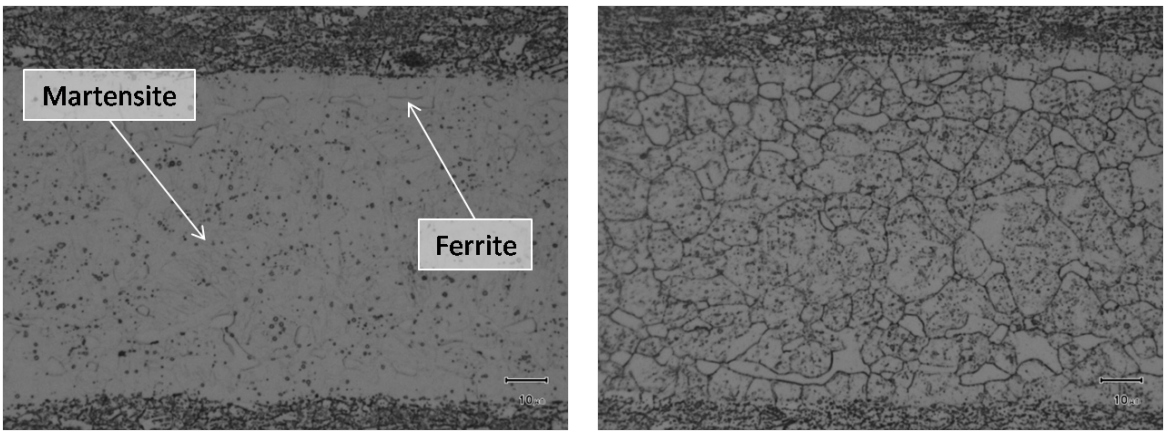

(a) α-layer in PM (b) α-layer in HAZ

Figure 5.36: Comparison of optical micrographs of SUS420J2 in PM and HAZ

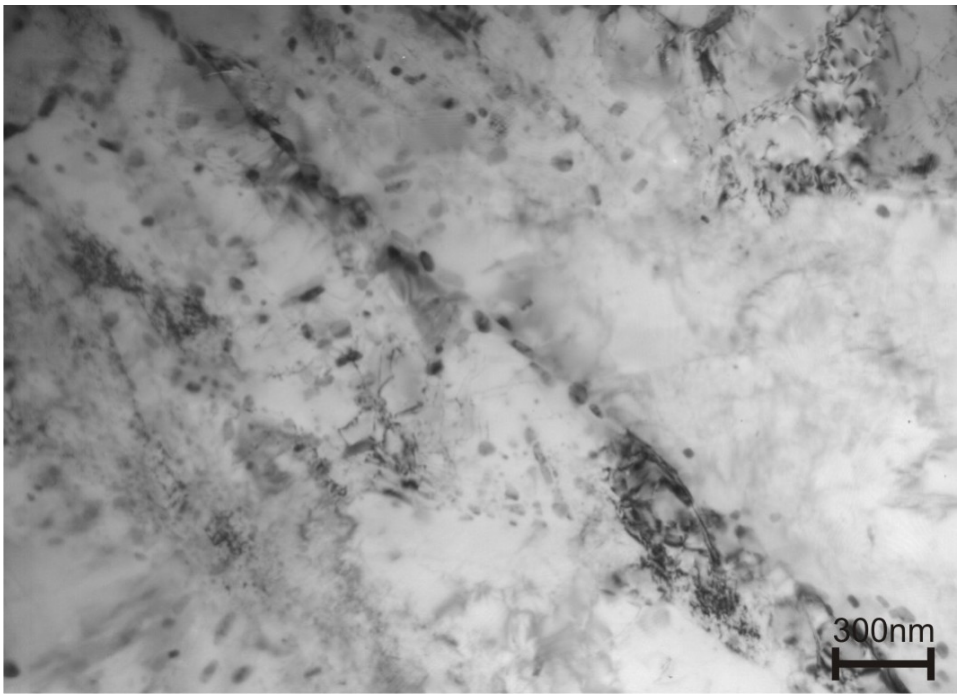

(a) 30 000 x

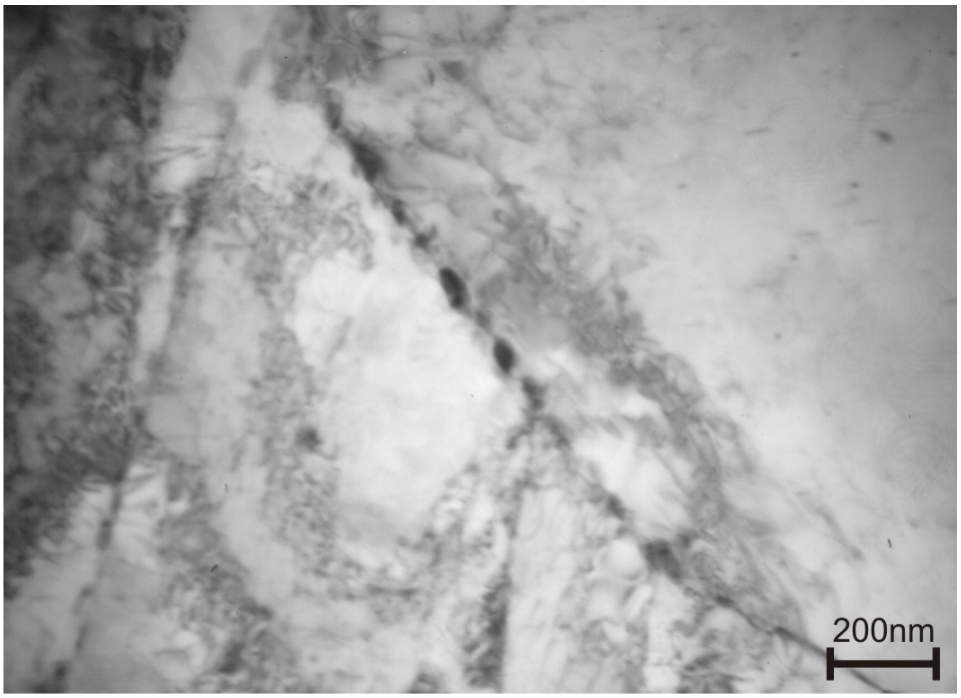

(b) 50 000 x

Figure 5.37: TEM images of grain boundary precipitates in HAZ of an α-layer

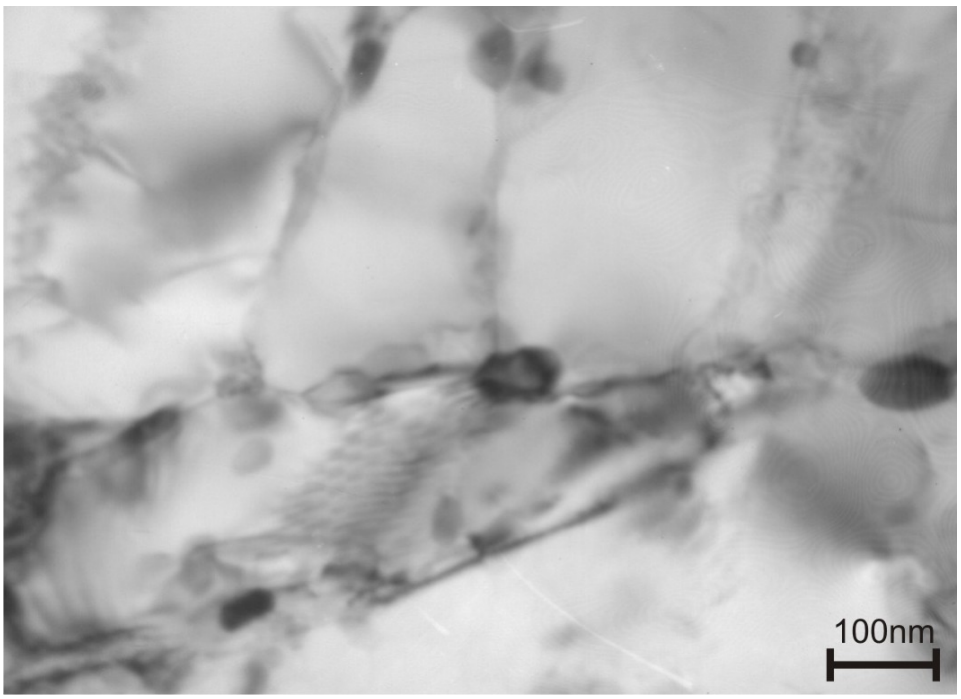

Figure 5.38: High magnification TEM image of precipitates in HAZ of an α-layer

Owing to the outcome of the microstructural investigations in HAZ, the hardness drop in α-layers apparently originated from the formation of grain boundary precipitates and presumably from recovery effects within the martensitic microstructure due to exposure to elevated temperatures in a region of $750°C$, slightly below A_{c1}. According to common terminology, the lath type microstructure in SUS420J2 layers within HAZ is therefore referred to as tempered martensite.

5.4.3.3 Thermomechanically Affected Zone

The thermomechanically affected zone is bounded by HAZ on the outer side and SZ on the inner side. TMAZ is characterized by exposure to both high temperatures and plastic deformation, whereas the impact certainly increases as approaching SZ. Owing to the hardness profile of the optimized weld (Figure 5.17) it was expected that the microstructure in α-layers changed significantly within TMAZ as the hardness increased from a level of about $550\,HV0.1$ close to HAZ to a high value of $630\,HV0.1$ close to SZ. Since the hardness increase was rather steady, it was considered that the microstructural changes from HAZ towards SZ were also steady. Therefore the investigations in TMAZ were restricted to an outer section close to HAZ on the one hand, and an in inner area close to SZ on the other hand. According to the hardness pattern in austenitic layers only minor modifications were expected in layers of SUS301.

Microstructure in TMAZ close to HAZ

Figure 5.39 shows the microstructure in TMAZ in a region close to HAZ. From the overview EBSD image (a) no deterioration of the layers was observed. Consequentially, the impact of plastic deformation in this region was regarded as negligible. Similar to PM and HAZ, the microstructure in SUS301 layers did not show any considerable differences to that of the austenitic layers in base material, thus having similar hardness. Accordingly, the temperatures in this region were not high enough to cause significant recrystallization since the proportions of deformation induced martensite and $M_{23}C_6$ precipitates did not differ remarkably from that of HAZ.

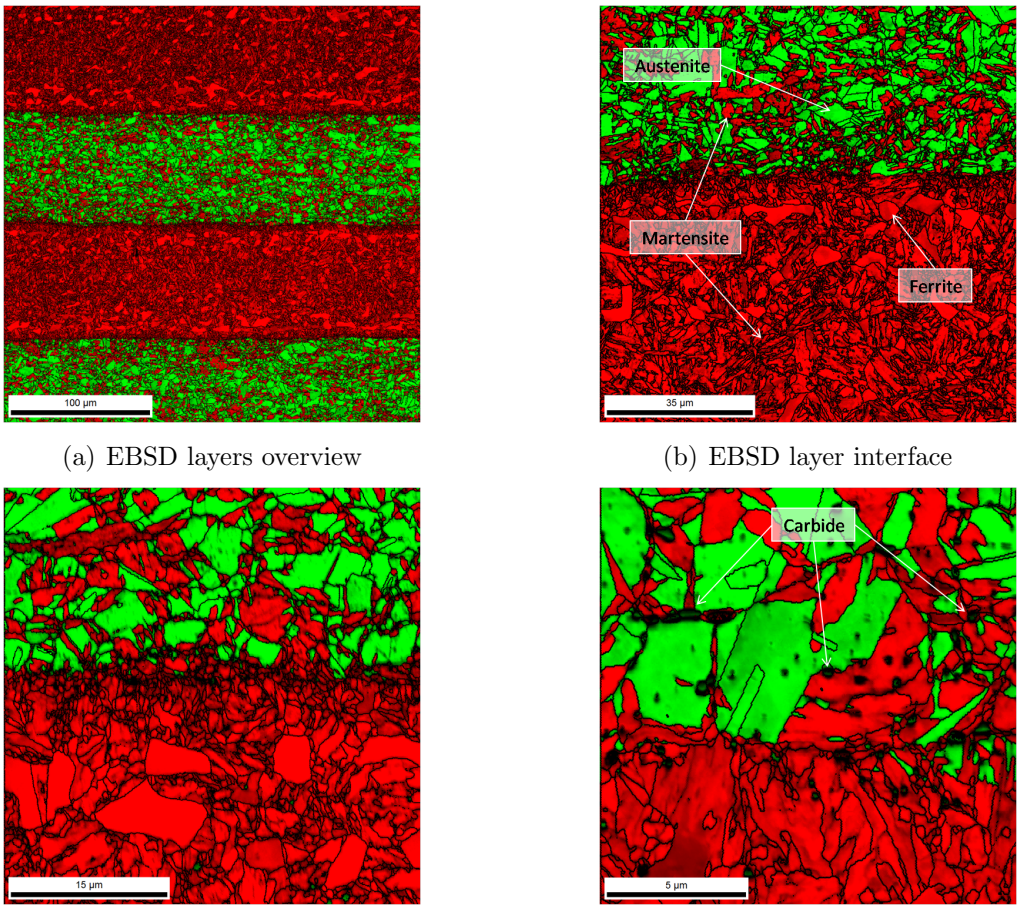

(a) EBSD layers overview

(b) EBSD layer interface

(c) EBSD interface detail

(d) EBSD interface detail

Figure 5.39: Microstructure characterization in TMAZ close to HAZ

In SUS420J2 layers a microstructure consisting of martensite and ferrite with proportions similar to PM was observed, as illustrated from the EBSD images of the layer interface in Figure 5.39. However, despite all similarities, the microstructural compositions in PM and TMAZ originated from a completely different thermal history. While in PM no exposure to elevated temperatures was recognized, the material underwent a temperature

cycle with peak temperatures exceeding A_{c1} in TMAZ. The latter consideration resulted from following observations: The minimum hardness in TMAZ was at the level of PM. Accordingly, no tempering effect in martensite had occurred, which led to the conclusion that the critical temperature for the formation of the hardness drop slightly below A_{c1} must have been exceeded, as the temperature increased by approaching the weld center. As a consequence, partial austenitization of the grains in SUS402J2 occured. Since only small portions transformed into austenite and subsequently into fresh martensite during cooling from this temperature, the microstructural appearance in TMAZ in regions close to HAZ was similar to PM. Due to the steady increase in hardness it was concluded that the amount of fresh martensite increased as approaching SZ. Moreover, it was deduced that the fresh martensite had a higher hardness than the martensite in PM as a consequence of a higher cooling rate. No indications for the presence of grain boundary precipitates similar to HAZ were noticed.

Microstructure in TMAZ close to SZ

In Figure 5.40 the microstructure in TMAZ in a region close to SZ is given. While further away from the weld center no plastic deformation was observed, the layers were clearly deteriorated near SZ. The SUS301 layers showed a fully austenitic microstructure with only few precipitates at the grain boundaries. No strain induced martensite was recognized in this region. This circumstance was explained by the impact of high temperatures and plastic deformation which resulted in an almost fully recrystallized microstructure. Accordingly, for the SUS301 layers in TMAZ it could be summarized as follows: The microstructure steadily changed from precipitation-rich austenitic/martensitic in a region close to HAZ into precipitation-poor 100 % austenitic in a region close to SZ caused by increasing temperature and plastic deformation as approaching the weld center. Consequentially, the slight decrease in hardness towards SZ in SUS301 observed in Figure 5.17 could be explained by the dissolution of the strengthening components.

Beside SUS301 also the microstructure in SUS420J2 modified in TMAZ as getting closer to SZ. As illustrated in Figure 5.40, the red α-layers showed a microstructure mainly composed of martensite with remarkably reduced ferrite content compared to the layers in TMAZ close to HAZ (Figures 5.39 and 5.40 c). The remaining ferrite was identified by the lighter red color and the more roundish bulky shape. Consequentially, a large proportion of the microstructure must have transformed to austenite which subsequently transformed to martensite during cooling. Therefore, the high hardness in this region was attributed to the formation of a large amount of fresh martensite. In summary, the hardness increase from a level of about $550\,HV0.1$ close to HAZ to a high value of $630\,HV0.1$ close to SZ could be explained by a steady increase of the proportion of fresh martensite in the microstructure of SUS420J2 due to an increase in temperature as approaching the weld center.

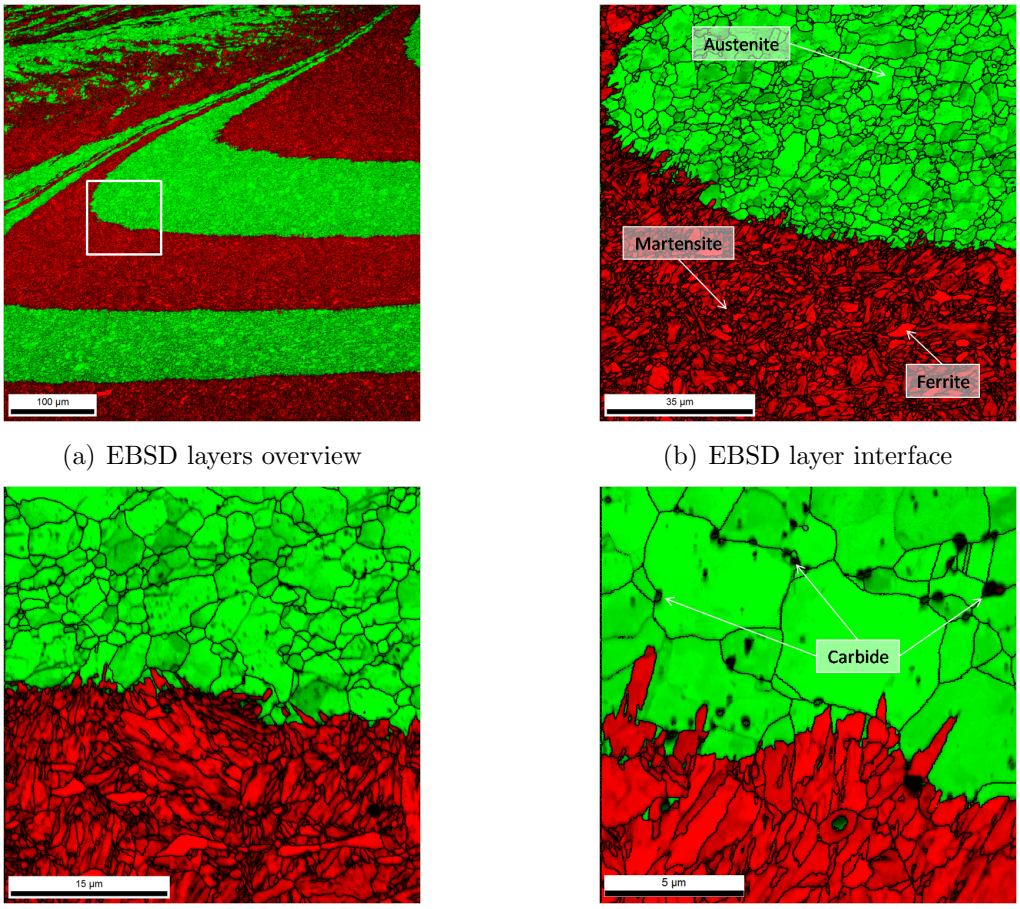

(a) EBSD layers overview

(b) EBSD layer interface

(c) EBSD interface detail

(d) EBSD interface detail

Figure 5.40: Microstructure characterization in TMAZ close to SZ

5.4.3.4 Stir Zone

While in PM, HAZ, and in a large part of TMAZ no or only little plastic deformation was observed, the microstructure within SZ was characterized by a tremendous degree of deformation. This observation is demonstrated in Figure 5.41, which shows an electrochemically etched optical micrograph as well as an EBSD image of the center of an optimized weld. While the layered structure was still recognizable in the lower region of the weld center, the deformation in the center of SZ reached a level of partial layer destruction caused by the direct interaction of the multilayered material with the tool probe during the FSW-process. As a consequence of the massive impact of plastic deformation in combination with friction generated between the surface of the steel sheets and the rotating tool shoulder, very high temperatures were expected to be reached in SZ.

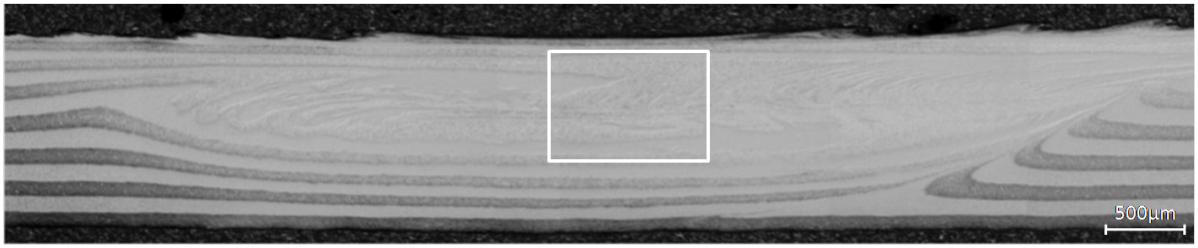

(a) Optical micrograph

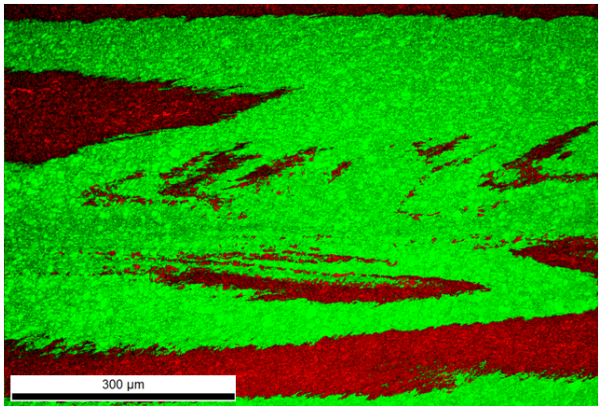

(b) EBSD image

Figure 5.41: Illustration of the structural impairment in the weld center

Figure 5.42 shows detailed EBSD images of the center of SZ. The mentioned layer deterioration is most obvious in the overview EBSD image (a), as the green grains indicate fcc-structure, while the red grains refer to bcc-structure. Even though the layers were partially destroyed, the distribution of fcc and bcc grains was still not random. More importantly, due to the solid state welding process no melting occurred at the weld center, thus no unfavorable dendritic structure of a rather undefined alloy occurred. Instead, the microstructure within SZ, as illustrated in Figure 5.42, was characterized as follows.

In zones of SUS301 a dynamically recrystallized microstructure consisting of 100 % austenite could be identified, whereas no indications of the presence of any deformation induced martensite were noticed. Figure 5.43 shows the interface between α- and γ-regions in SZ at high magnifications. Apparently, no $M_{23}C_6$ precipitates occurred. As a consequence of these observations, the microstructure in former layers of SUS301 was classified as fully recrystallized due to the combined impact of high temperature and intense plastic deformation. Furthermore, the fact that the minimum hardness of 259 $HV0.1$ was measured within SZ could be explained by the absence of any strengthening components such as precipitates or strain induced martensite.

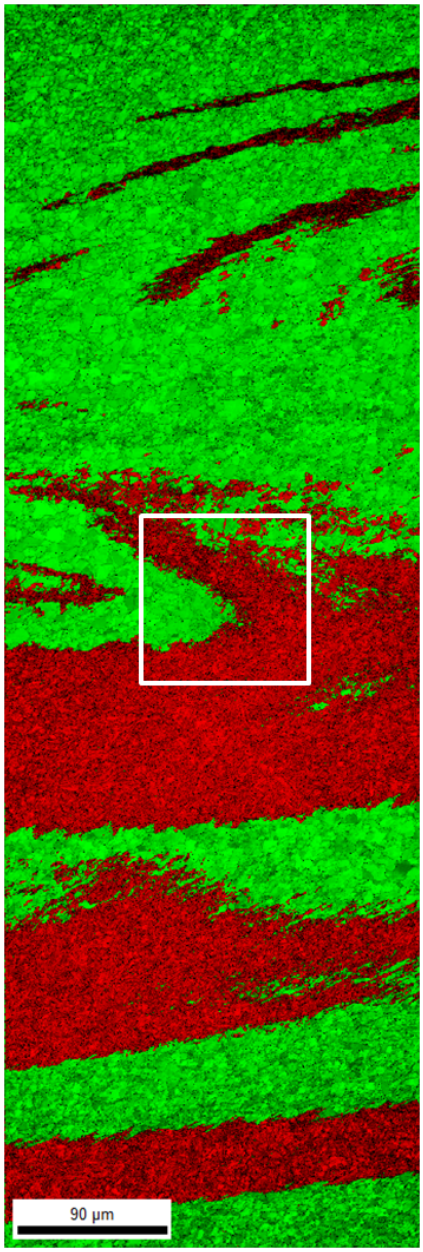

(a) Overview image

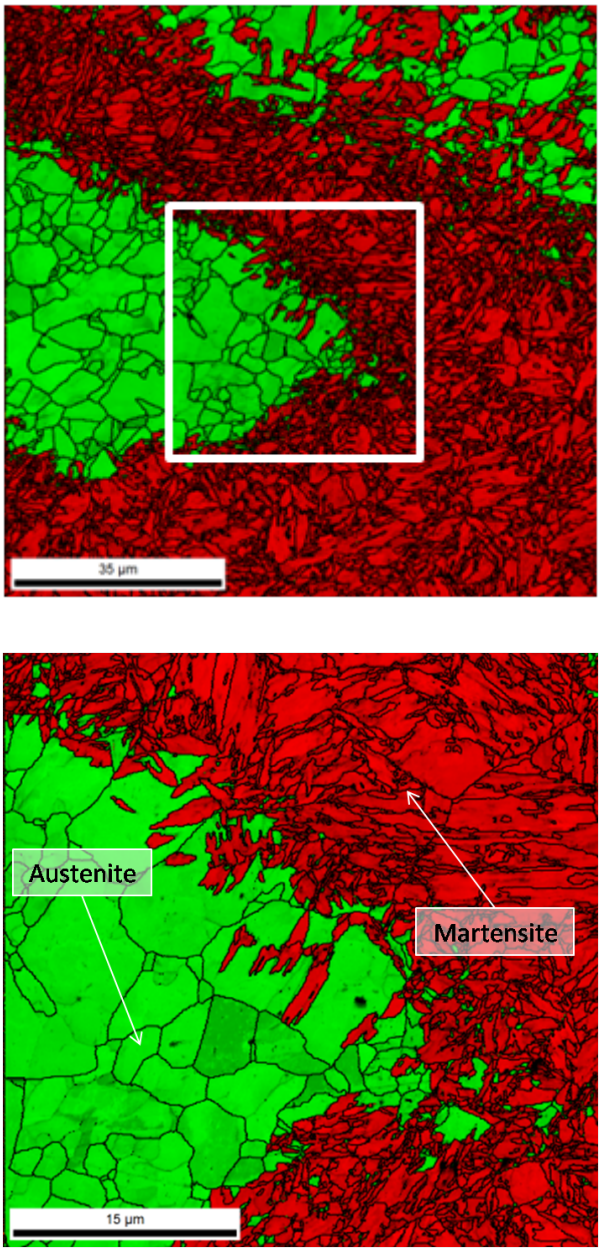

(b) Detail images

Figure 5.42: EBSD images of SZ center

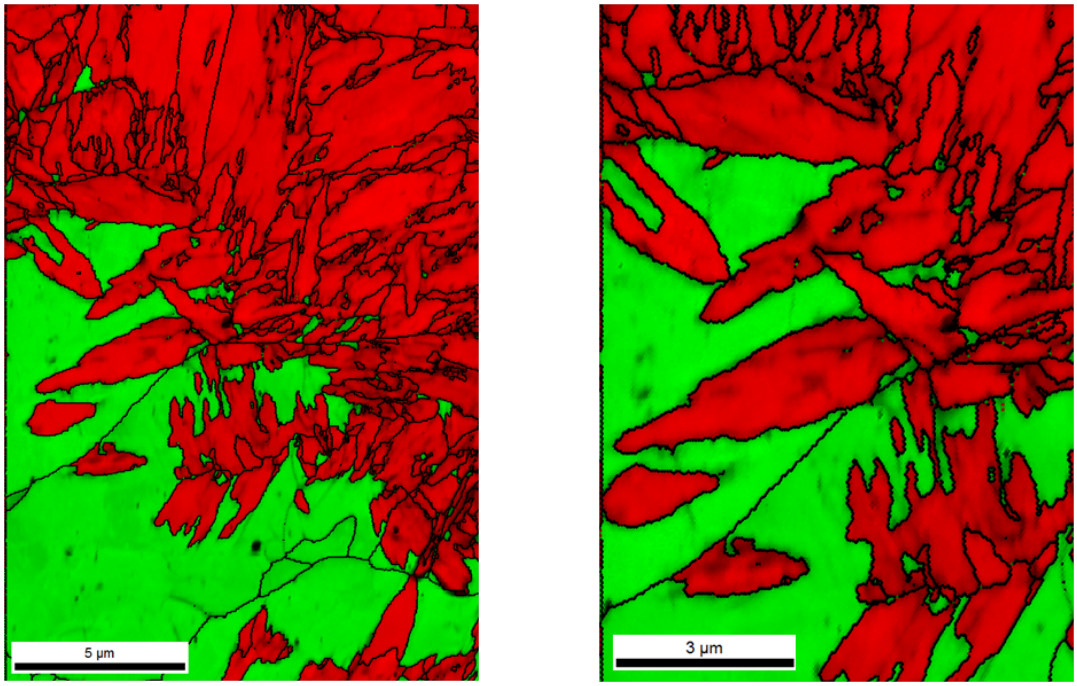

(a) EBSD α/γ-interface

(b) EBSD interface detail

Figure 5.43: EBSD images of the interface between α and γ in SZ

The former SUS420J2 layers showed a fully martensitic microstructure, as illustrated in Figures 5.42 and 5.43. Due to the high temperatures within SZ all the martensitic and ferritic grains transformed to austenite followed by a transition to martensite during cooling. Owing to that, the high hardness in α-zones within SZ originated from the formation of a microstructure consisting of 100 % fresh martensite.

5.4.3.5 Fracture Behavior

Figure 5.44 shows the macro photo of a fractured tensile specimen of an optimized weld. As for all parameter sets exceeding a joint efficiency of 85 %, fracture occurred at high strength levels in HAZ on RS after necking. Figure 5.45 gives SEM images of the fracture surface. Since in HAZ no structural impairment occurred, the layered structure was clearly identifiable. Furthermore, the fracture surface did not show any indications of sudden fracture and was evenly deformed. Delamination was sparsly observed, as only a few rather small break-ups were identified at the layer interfaces. In order to classify the fracture behavior of the single component steels, detailed SEM images of the single layers are given in Figure 5.46.

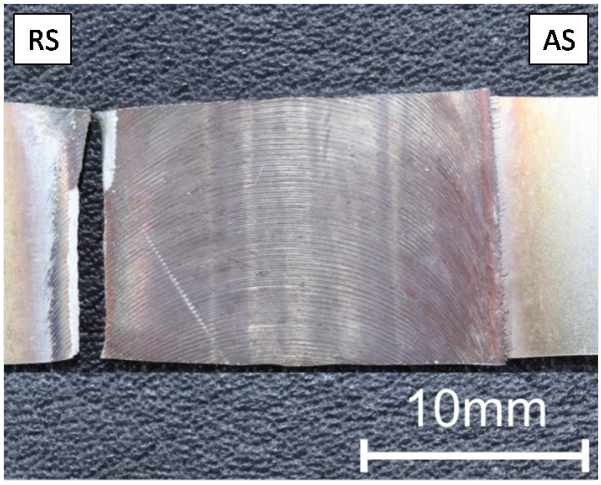

Figure 5.44: Fractured tensile specimen of an optimized weld

As expected, the SUS301 layers (Figure 5.46 a) showed a very ductile fracture behavior, which was not attributed to the laminated structure of the compound but to the natural behavior of this specific austenitic steel grade. However, also the layers of SUS420J2 showed a mainly ductile fracture behavior, which was clearly not expected for this kind of material in monolithic state. Consequentially, the ductile fracture behavior of the martensitic layers was attributed to the structural support in the hot rolled laminate. These observations showed good correlation to the ductile fracture behavior of the base material.[16,17]

Figure 5.47 demonstrates the fracture path in transverse direction by means of optical microscopy. As from the SEM images also from LOM figures no indications of brittle behavior were noticed. Instead, the cross section showed a deformed fracture surface indicating ductile shear rather than brittle cleavage. Moreover, no delaminations at the layer interfaces or tunnel cracks within single layers were observed. At higher magnifications the microstructure of the brighter α-layers in the fracture zone could be identified as tempered martensite, as the grain boundaries were quite pronounced.

According to mentioned observations from hardness testing and microstructural investigations, it could be clearly deduced that fracture occurred in HAZ due to the formation of a soft, tempered martensitic microstructure in SUS420J2 layers. As explained, HAZ on RS was closer to the weld center than on AS in any case. Since process related thinning always occurs and increases as approaching the weld center, the local reduction of the weld cross section in HAZ on RS was more pronounced than in HAZ on AS resulting in higher local stresses leading to preferred fracture in HAZ-RS.

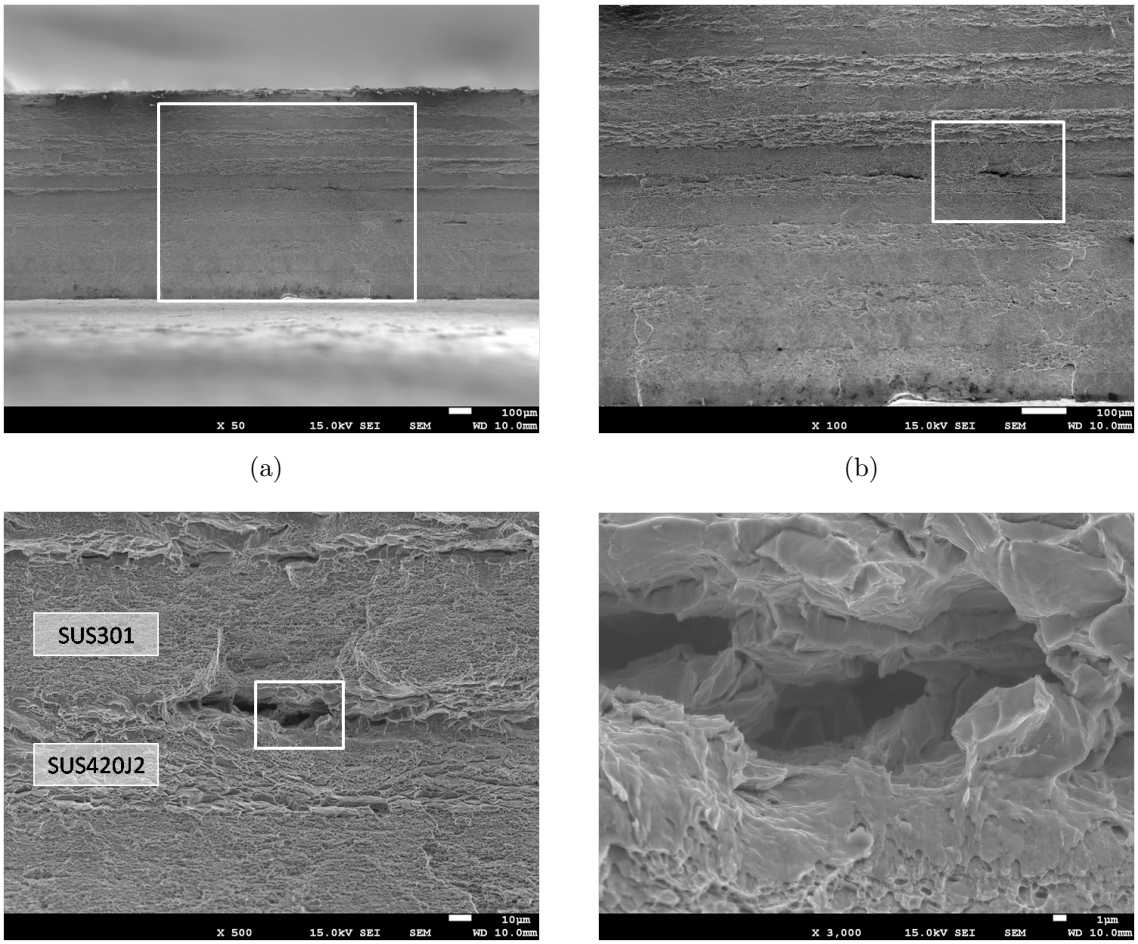

(a) (b)

(c) (d)

Figure 5.45: Fracture surface in HAZ-RS of an optimized parameters weld

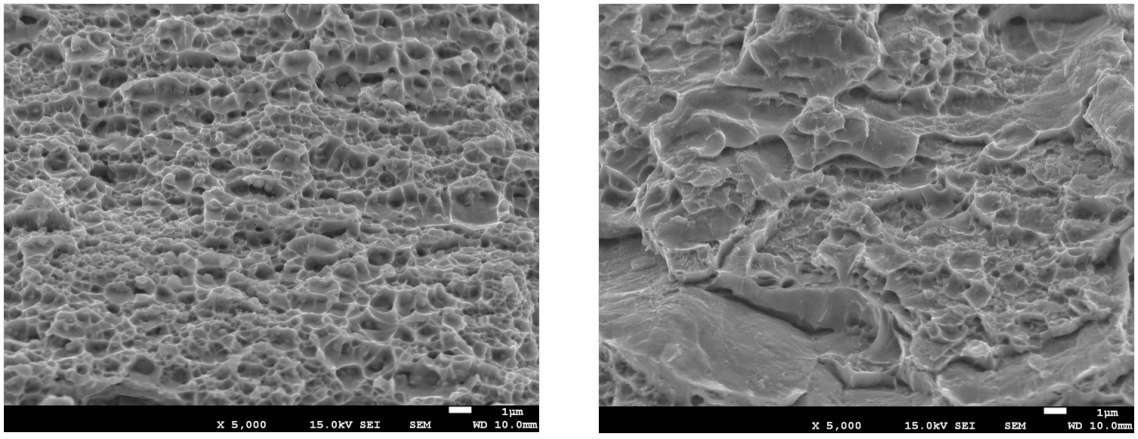

(a) SUS301 layer (b) SUS420J2 layer

Figure 5.46: Fracture surface of the single layers

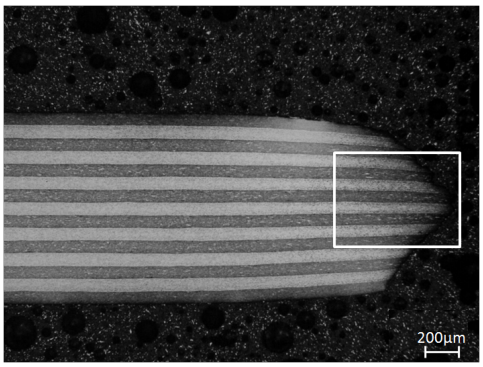

(a) Overview

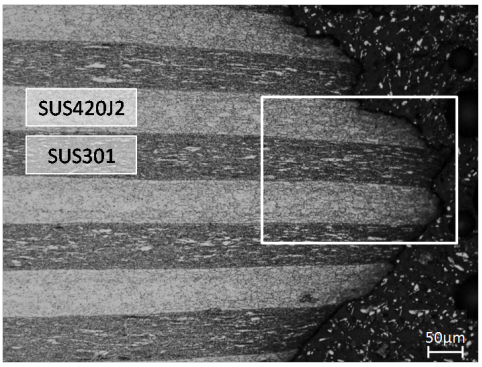

(b) Overview

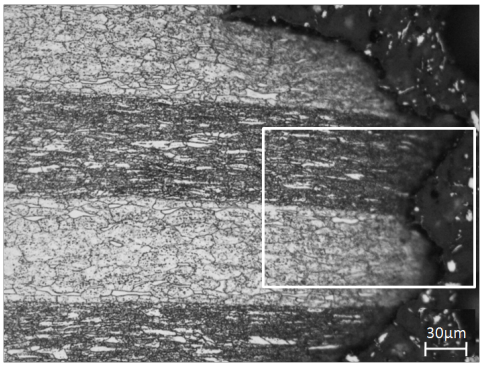

(c) Layer interface

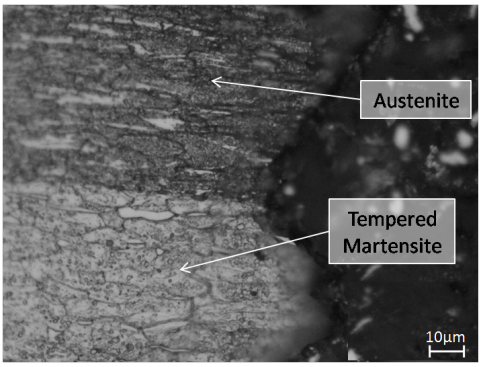

(d) Interface detail

Figure 5.47: Fracture path in HAZ-RS of an optimized parameters weld

5.5 Post Weld Heat Treatment

The purpose of the post weld heat treatment (PWHT) was the removal of the local weakness of the martensitic layers in HAZ by applying a heat treatment consisting of holding at $1000°C$ for 2 minutes followed by air cooling. The outcome of the PWHT and a comparison of the mechanical properties of samples in both PWHT condition and as-welded condition are presented in this section. Furthermore, microstructural modifications and the influence of the PWHT on the fracture behavior are explained.

5.5.1 Mechanical Properties

Figure 5.48 shows a comparison of the hardness patterns across the weld for a revolutionpitch of $0.27\,mm\,rev^{-1}$ in both as-welded and PWHT condition. As desired, the hardness drop in the martensitic layer was removed during PWHT leading to a remarkably higher minimum hardness in HAZ of $508\,HV0.1$ compared to $322\,HV0.1$ in as-welded condition. Furthermore, the increase in hardness towards the weld center was reduced by PWHT resulting in a lower maximum hardness within SZ of only $607\,HV0.1$ compared to $668\,HV0.1$ in as-welded condition. In austenitic layers no significant difference between PWHT sample and as-welded sample was observed even though in general the hardness seemed to be slightly higher in as-welded condition.

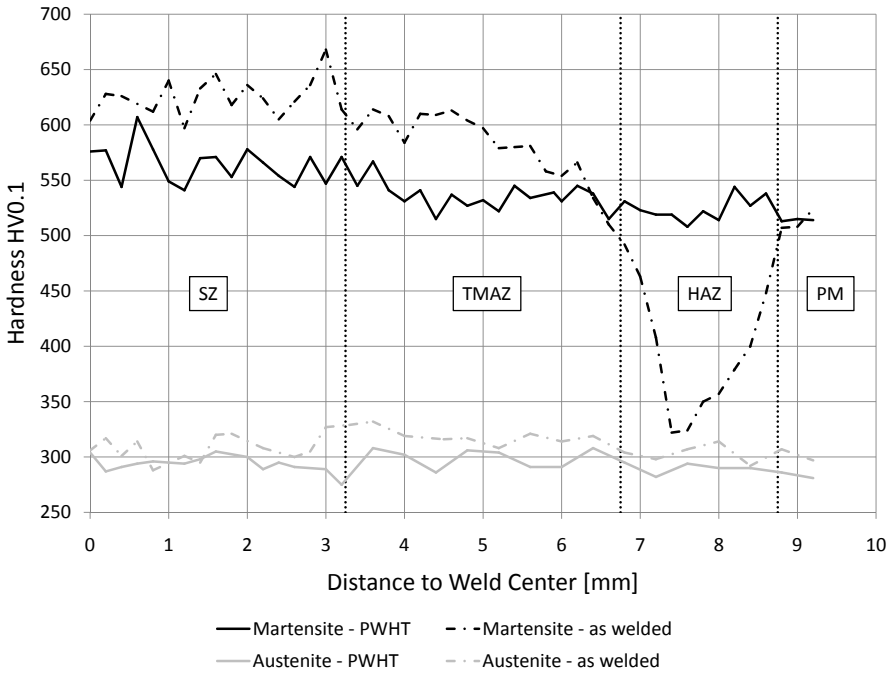

Figure 5.48: Hardness profile across the weld seam in as-welded and PWHT condition

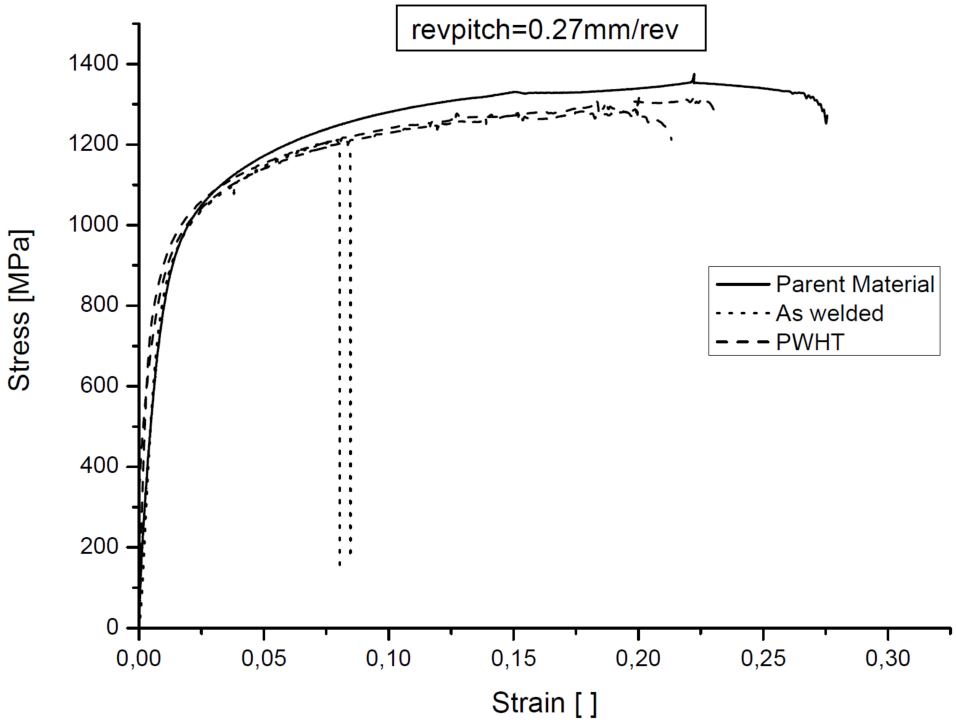

Figure 5.49: Influence of the PWHT on the tensile properties

Condition	$Revpitch[mm\,rev^{-1}]$	UTS [MPa]	Max. elongation [%]
As-welded	0.27	1210	8
PWHT	0.27	1310	22
Parent material	-	1370	26

Table 5.4: Tensile properties in as-welded and PWHT condition

In table 5.4 a summary of the tensile properties of welds with a revolutionpitch of $0.27\,mm\,rev^{-1}$ in as-welded and PWHT condition as well as the tensile properties of the parent material are given. Figure 5.49 shows the corresponding stress-strain curves. Apparently, by applying PWHT a tremendous improvement of the tensile properties was achieved. The ultimate tensile strength (UTS) could be enhanced to $1310\,MPa$ which corresponds to a joint efficiency of more than 95 % and an increase of about 8 % compared to the as-welded condition. Moreover, the maximum elongation was improved significantly to 22 % equaling almost 85 % of the parent material. This corresponds to an improvement of 275 % in fracture elongation compared to the as-welded condition.

5.5.2 Fracture Behavior

While for samples with a revolutionpitch of $0.27\,mm\,rev^{-1}$ fracture occurred in HAZ on RS in as-welded condition, PWHT samples fractured either in PM well away from the weld or in SZ, as illustrated in Figure 5.50. Accordingly, it was considered that after removing the soft HAZ, the potentially weakest part of the weld, and therewith the strength determining factor was SZ. However, it was demonstrated that with appropriate welding parameters, the strength level of SZ was similar to that of the parent metal resulting in almost identical mechanical properties. Due to the large fracture elongation that was reached, a very ductile fracture behavior was expected for PWHT samples in both austenitic and martensitic layers.

Figures 5.50 (b) and 5.51 illustrate the fracture behavior of a PWHT sample in case of fracture occurred in PM. It was observed that multiple necking occurred in and around the fracture zone, as evidenced from the macro photo and the optical microsection in Figure 5.51 (d). Furthermore, similar to previous studies [18] partial delamination was observed in several layer interfaces, as illustrated in the SEM images of the fracture surface and the optical micrographs of the fracture cross section in Figure 5.51. From the high magnification SEM image (c) of the fracture surface a clear ductile fracture pattern was observed in both austenitic and martensitic layers, as the upper layer represents SUS420J2 and the lower layer represents SUS301.

The behavior in case of fracture occurred in SZ is demonstrated in Figures 5.50 (c) and 5.52. The macro photo shows that fracture occurred in SZ after considerable necking. In contrast to the case of fracture in PM, no significant delamination was observed, as demonstrated in the SEM images and optical micrographs in Figure 5.52. Instead, the figures show a strongly mixed area located directly in the center of the fracture path. As a consequence, it was assumed that the strength of the layer interfaces might have been increased by FSW, whereas the compound was debilitated due to structural impairment. However, in the present case the combination of those phenomenons might have led to an overall strength of SZ that was in the range of the parent material. Certainly, further investigations on this specific topic are necessary.

As a summary of the mentioned observations, the fracture behavior for PWHT samples was classified as distinctively ductile in both cases of fracture in PM and fracture in SZ.

(a) Overview of fractured samples

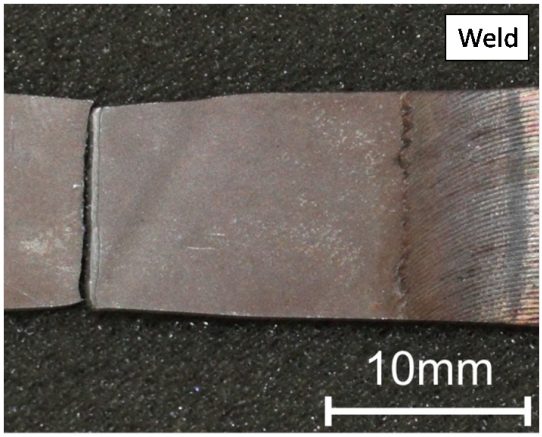

(b) Fracture in PM

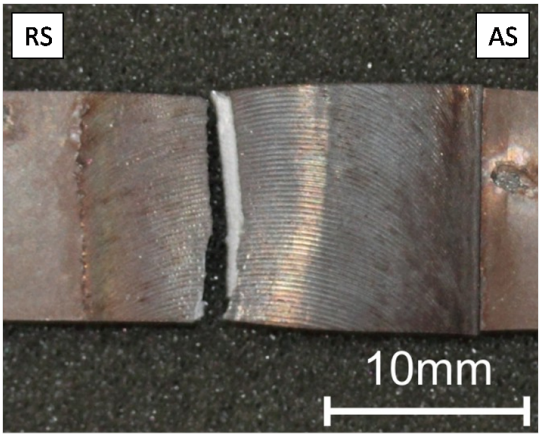

(c) Fracture in SZ

Figure 5.50: Fractured PWHT tensile specimen

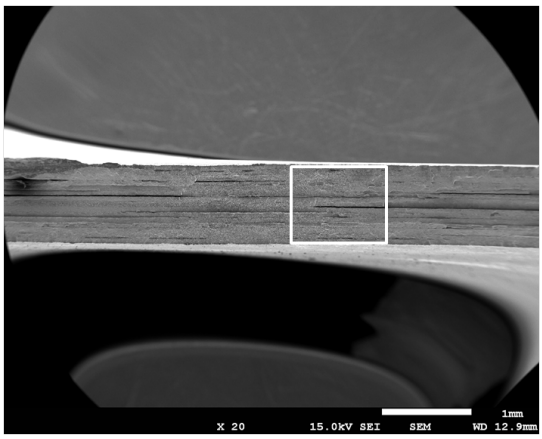

(a) SEM image

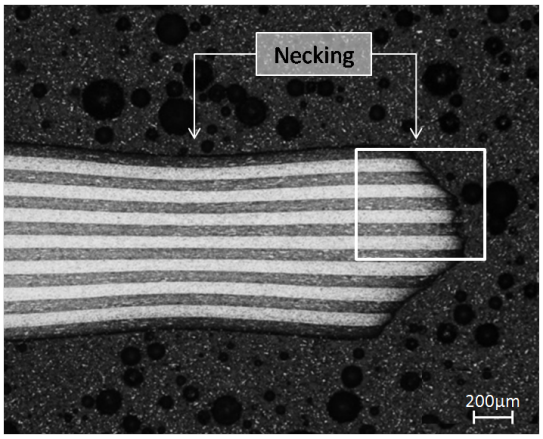

(d) LOM Overview

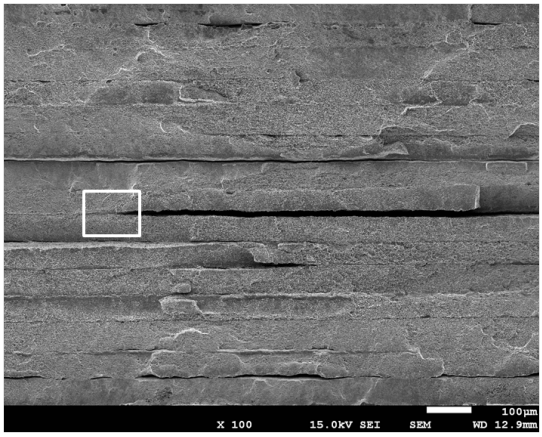

(b) SEM image

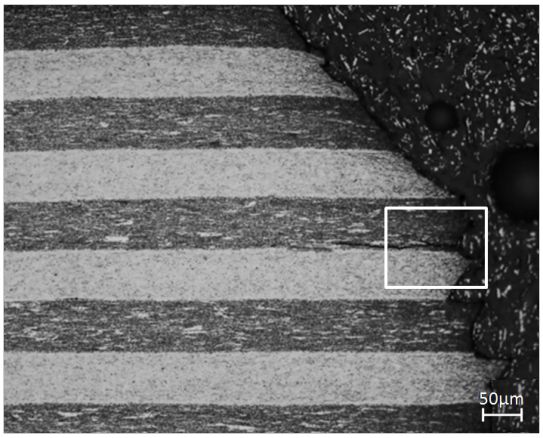

(e) LOM Layer interface

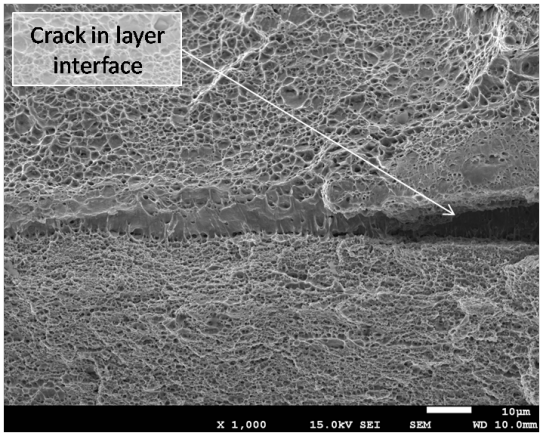

(c) SEM image

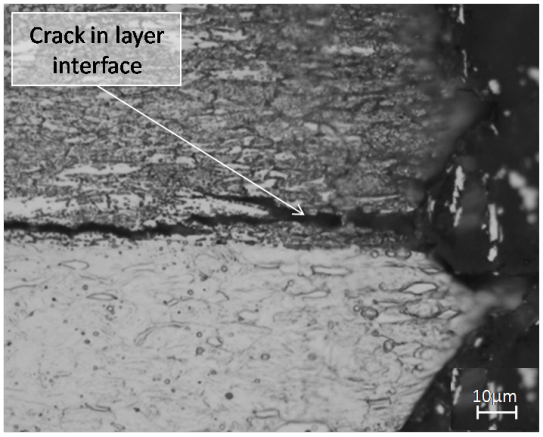

(f) LOM Interface detail

Figure 5.51: Fracture behavior of a PWHT sample. Fracture occurred in PM

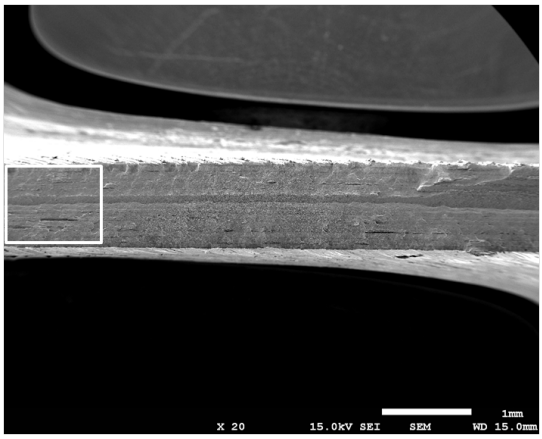

(a) SEM image

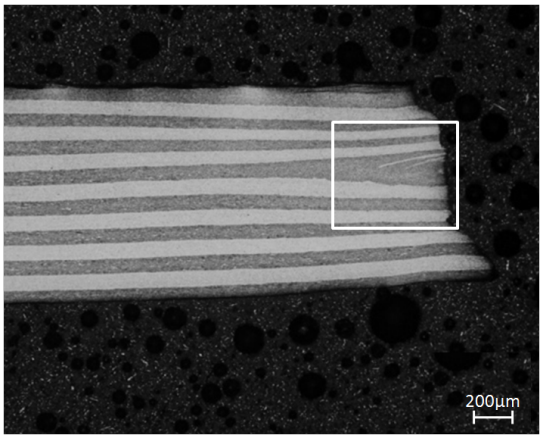

(d) LOM Overview

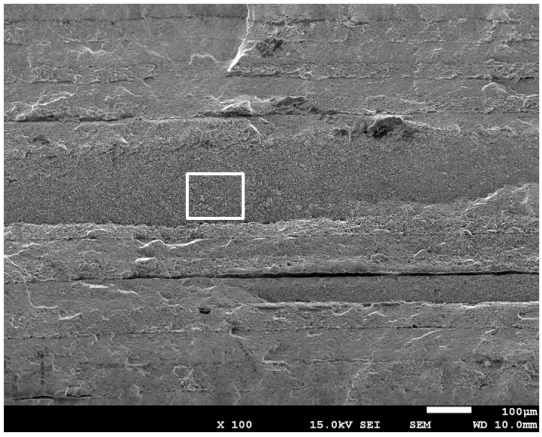

(b) SEM image

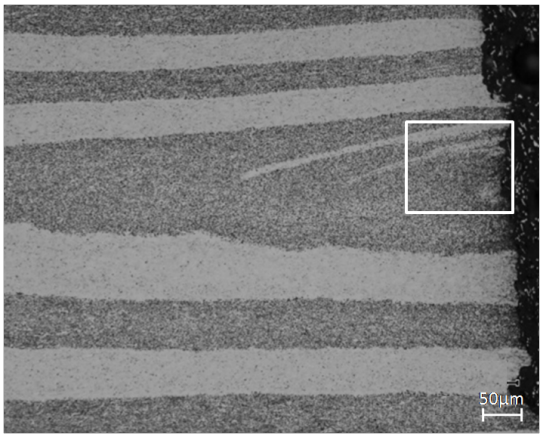

(e) LOM Layer interface

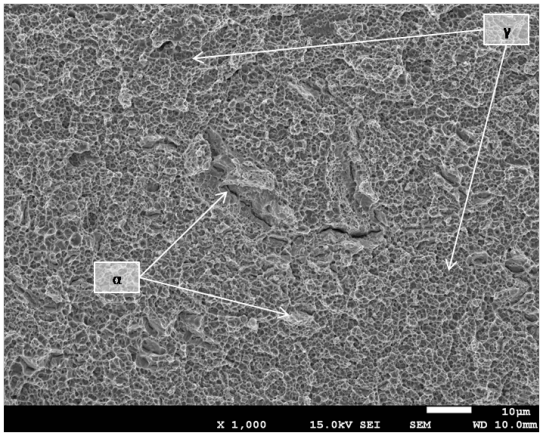

(c) SEM image

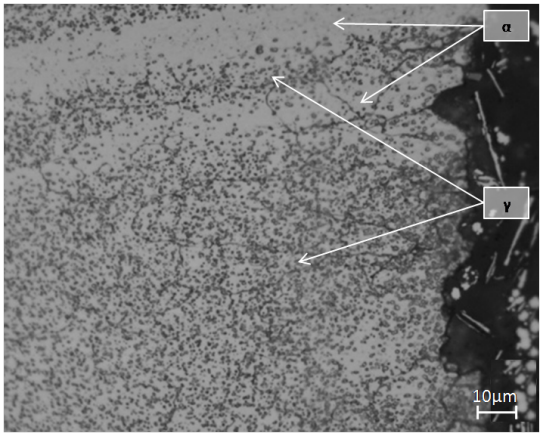

(f) LOM Interface detail

Figure 5.52: Fracture behavior of a PWHT sample. Fracture occurred in SZ

5.5.3 Metallography

The microstructure in HAZ was investigated for both as-welded and PWHT samples by means of EBSD and LOM in order to assess the influence of the heat treatment.

Figure 5.53 shows a comparison of the microstructure in SUS301 layers in HAZ for both mentioned conditions. Apparently, the amount of deformation induced martensite was reduced from about 32 % to 17 % by applying PWHT. The slight reduction in hardness in austenitic layers may be attributed to this circumstance.

However, the microstructural modifications in layers of SUS420J2 were considered as more important and therefore were investigated more in detail. Figures 5.54 and 5.55 show electro-chemically etched optical micrographs and EBSD images of α-layers in both as-welded (a) and PWHT (b) condition. In as-welded condition the microstructure consisted of a HAZ-typical tempered martensitic/ferritic microstructure with a large number of grain boundary precipitates. During PWHT when holding at $1000°C$, however, the $M_{23}C_6$ precipitates were dissolved, the tempered martensite transformed into austenite, while the ferrite remained stable. During subsequent air cooling, the austenite retransformed into martensite, the ferrite still remained stable, but the reprecipitation of carbides was ommitted due to sufficiently rapid cooling. Consequentially, the HAZ after air cooling showed a microstructure similar to that of the SUS420J2 layers in the parent material consisting of martensite and ferrite. Therefore the hardness values in HAZ in PWHT condition were similar to PM, whereas in as-welded condition the HAZ-typical hardness drop was noticed. The reduction in hardness in the martensitic areas within TMAZ and SZ in PWHT condition compared to as-welded condition (Figure 5.48) was considered a consequence of the lower cooling rate during air cooling compared to the cooling rate during the FSW-process.

Finally it could be summarized, that the enhanced mechanical properties of samples in PWHT condition resulted from the removal of the soft HAZ in layers of SUS420J2 caused by the creation of a microstructure similar to that of PM.

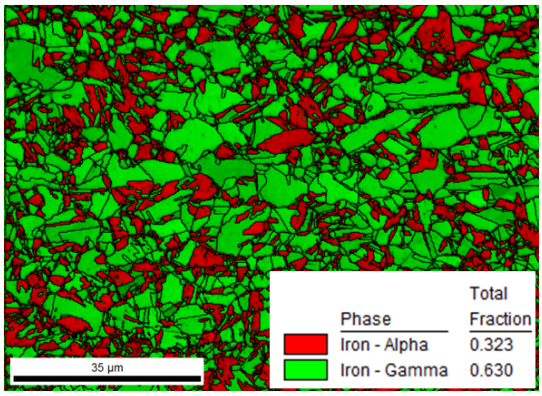

(a) EBSD image. As-welded condition

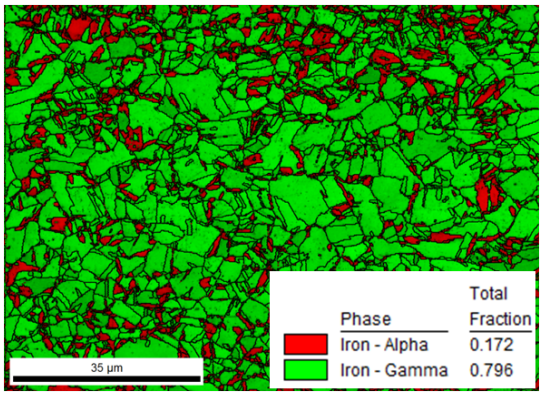

(b) EBSD image. PWHT condition

Figure 5.53: Microstructure in HAZ of an SUS301 layer with/without PWHT

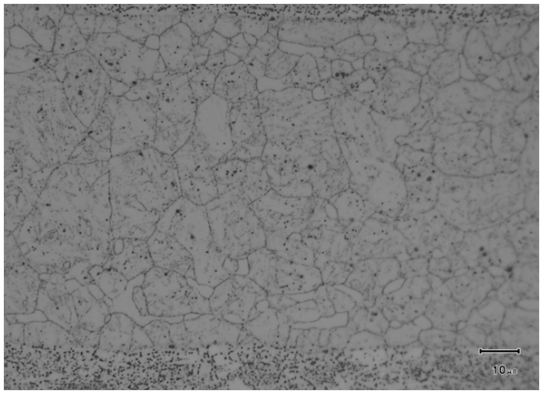

(a) As-welded condition

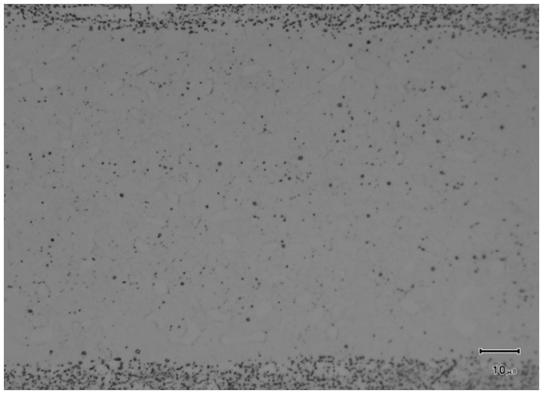

(b) PWHT condition

Figure 5.54: Micrographs of HAZ of a SUS420J2 layer with/without PWHT

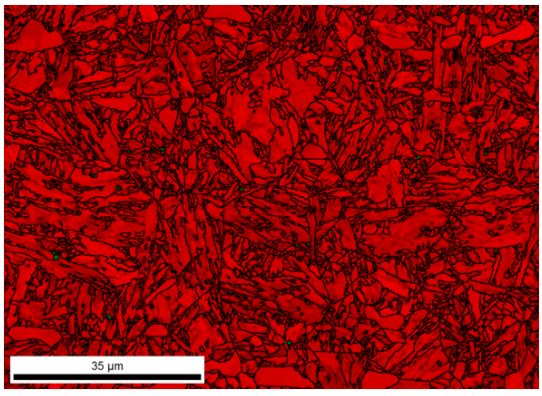

(a) EBSD image. As-welded condition

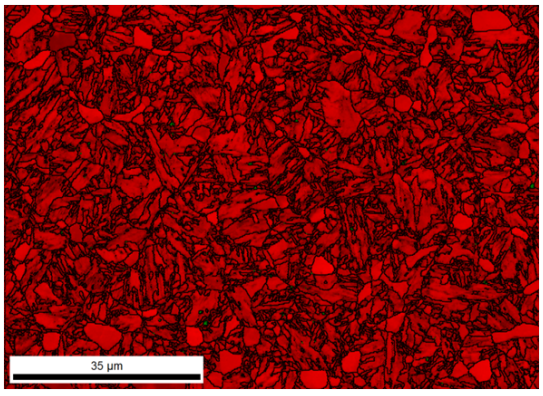

(b) EBSD image. PWHT condition

Figure 5.55: Microstructure in HAZ of a SUS420J2 layer with/without PWHT

6 Summary

High strength multilayered steel sheets consisting of 15 alternating layers of SUS301 austenitic stainless steel (8 layers) and SUS420J2 martensitic stainless steel (7 layers) with an initial thickness of 1.2 mm were welded in butt configuration using friction stir welding. Temperature measurement was carried out, the mechanical properties were assessed, and the microstructure was analyzed using LOM, SEM, EBSD, and TEM. Furthermore, the influence of a post weld heat treatment (PWHT) on the weld properties was evaluated. The results can be summarized as follows.

1. Friction stir welding of high strength multilayered steel sheets was accomplished successfully with a tool consisting of a sintered matrix of 92 % tungsten carbide and 8 % cobalt. With appropriate welding parameters sound welds with a fully consolidated root could be produced.

2. The temperatures at the same distance from the weld center measured on top of the welded sheets were in general higher on AS than on RS. The maximum temperature was measured for the lowest revolutionpitch at 10 mm distance from the weld center on AS equaling around 750°C.

3. Welds with optimized tensile properties were created at a tool rotation speed of 800 $mm\,rev^{-1}$ and a welding speed of 200 $mm\,min^{-1}$ resulting in an ultimate tensile strength of 1240 MPa and a maximum elongation of 13 %. This corresponds to a joint efficiency of 90 % according to strength.

4. The hardness across the weld seam did not change significantly for layers of SUS301. For layers of SUS420J2 the hardness profile showed a pronounced hardness drop in HAZ and a steady increase of hardness towards the weld center, whereas the maximum hardness in SZ significantly exceeded that of PM. Asymmetry was observed, that is, HAZ on RS was systematically closer to the weld center than HAZ on AS. The critical temperature for the formation of the weak HAZ was in the region of 750°C, slightly below A_{c1}.

5. Low heat input welds showed pores in SZ and an unconsolidated root which led to fracture at low strength levels directly within SZ. High heat input welds showed maximum deterioration in the laminated structure combined with considerable thinning, which resulted in modest tensile properties and fracture in SZ. Welds

with optimized parameters fractured in HAZ on RS due to softening effects in HAZ. Fracture occurred on RS due to more pronounced thinning compared to AS leading to higher local stresses.

6. The SUS301 layers showed a microstructure consisting of mainly austenite, some deformation induced martensite, and a large number of chromium-rich precipitates in PM and HAZ. In TMAZ, as approaching SZ, the microstructure changed in a way that the proportions of strain induced martensite and precipitates decreased, whereas the proportion of austenite increased. Within SZ an entirely austenitic microstructure was created due to full recrystallization.

7. The SUS420J2 layers showed a microstructure consisting of mainly martensite and some ferrite in PM, and tempered martensite with grain boundary precipitates and some ferrite in HAZ. In TMAZ, as approaching SZ, the microstructure changed in a way that the proportion of ferrite decreased, whereas the proportion of fresh martensite increased. Within SZ a fully martensitic microstructure was created due to full austenitization followed by rapid cooling.

8. By applying PWHT the soft HAZ was removed. For welds with a strong SZ a joint efficiency of 95 % according to strength and a fracture elongation of 85 % of the parent material could be achieved. In those cases fracture occurred either within SZ or in PM after considerable necking.

7 Outlook

In this study high strength multilayered steel sheets were successfully welded for the first time. It was shown that friction stir welding is a very suitable process for joining this kind of material by producing welds with mechanical properties similar to that of the base material. Furthermore, a lot of new information concerning the FSW-process and the behavior of the material in such a process were gathered during this project. However, there is still a lot of potential output remaining since a lot of additional data were gained during this work. Due to the availability of a large amount of EBSD data for example, detailed crystallographic investigations such as texture analyses in different weld regions could be performed in order to visualize the deformation behavior and thereby gain deeper understanding of the process and the material itself. In this study only individual measurements were carried out but in terms of reproducability it is recommended to use statistical methods such as Design of Experiments (DoE) as a next step in the process optimization. The additional use of a simulation could help to understand the unusually large differences in peak temperature between the advancing and retreating side of the weld for example.

Further investigations could be carried out to clarify uncertain observations. With computer tomography (CT) it would be possible to detect pores in the welds which might me interesting in order to investigate the evolution of weld defects more in detail. A different approach in tensile testing in which the flashes, ridges and roughnesses on the top and bottom surfaces of the samples are milled off would show the mechanical properties and fracture behavior of the material without any geometric influences such as notch effects. Furthermore, due to the fact that the steel compound consisted of two different types of stainless steels, it would be interesting to investigate the influence of the FSW-process on the corrosion behavior of the sheets. Finally, comparative studies with different welding methods should be carried out in the same weld configuration as in this work.

At the moment, an additional study is in progress which focuses on the comparison of the mechanical properties and the microstructure of overlap joints accomplished with laser welding, resistance spot welding, and friction stir welding. The progress of the work is not very advanced yet, though some mechanical properties have been evaluated so far. From the status quo it could be deduced, that concerning tensile strength friction

stir welding outperformed the other welding methods by a factor of about 3.5. Certainly, similar results are to be expected for welds in butt configuration, though no comparative results from different welding methods are available yet. The results of the lap welding experiments will also be presented somewhere as a result of the cooperation between the Institute for Materials Science and Welding at Graz University of Technology and the Departement of Materials Engineering at The University of Tokyo.

As already mentioned in this study, multilayered steel has great potential when it comes to lightweight design in automotive industries due to its high energy absorbtion capacity which allows a tremendous reduction in sheet thicknesses compared to conventional steels. As car manufacturers nowadays are faced with stricter and stricter requirements concerning fuel consumption, CO_2 emission, and crash safety, they are forced to use different materials in order to comply with required standards. Due to the great eligibility of the multilayered steel for mentioned restrictions and the fact that no successful welding with other methods was reported so far, an industrial application of friction stir welding of multilayered steel has realistic chances for implementation in the near future.

Certainly, some process related barriers for an industrial application of FSW of steel are present at the moment. For example FSW robot grippers are heavier than grippers for conventional welding methods due to the need for rigid base plates in FSW. As a consequence, more expensive industrial robots with higher payloads need to be used which makes the process cost inefficient.

Currently the major problem of friction stir welding steel is clearly the absence of cost efficient tools. Accordingly, a lot of scientific effort needs to be put in this field. However, as a consequence of a possible implementation of FSW of multilayered steel in the huge market of automotive engineering, it was considered that large and powerful companies would push the technology forward by participating in the development of more cost efficient tools. As a result of this improvement negative aspects such as process related disadvantages should be overcompensated.

List of Figures

2.1 Timeline of action: March - November 2011 3

3.1 Iron-chromium equilibrium phase diagram [1] 6
3.2 Influence of carbon on the expansion of the gamma loop [3] 6
3.3 Carbide formation in Fe-Cr system at constant C content [4] 7
3.4 Influence of nickel on the expansion of the gamma loop [2] 8
3.5 Pseudobinary section of the Fe-Cr-Ni system at 70 % Fe [3] 9
3.6 Schaeffler diagram.[4] ① SUS301, ② SUS420J2 9
3.7 Pseudobinary phase diagram. Fe-18Cr-8Ni alloy with varying C-content [6] 11
3.8 Influence of deformation on the austenite-to-martensite transformation [8] 12
3.9 Pseudobinary phase diagram. Fe-13Cr alloy with varying C-content [3] . 14
3.10 CCT diagram for an Fe-13Cr alloy with 0.35 % C [11] 14
3.11 Multilayered steel composite [22] 17
3.12 Overview of the mechanical properties of different steel types [23] 17
3.13 Schematic illustration of the FSW process [29] 18
3.14 Microstructural regions in a friction stir weld [25] 20
3.15 Sketch of the most important welding parameters 21
3.16 Weld quality as a function of the revolutionpitch [34] 22
3.17 Sketch of the most important FSW-tool features [29] 25
3.18 Different tool shoulder geometries [29] 26
3.19 Different tool probe designs [39] 27
3.20 Friction stir welded Airbus central wing box [44] 29
3.21 Temperature dependence of strength of Al-alloys and steels [45] 29

4.1 Production process of multilayered steel 32
4.2 Microstructure in multilayered steel consisting of SUS301 and SUS420J2 33
4.3 Structure in SUS301 33
4.4 Structure in SUS420J2 33
4.5 EDS line scan through Cr-rich precipitates in an α-layer 34
4.6 Microstructure of the interface between SUS301 and SUS420J2 34
4.7 EDS line scan across the interface through a Cr-rich precipitate 34
4.8 Deformation behavior of multilayered steel (MS) compared to DP 590 . . 35
4.9 MTS FSW machine 36

4.10 Water cooled head . . . 36
4.11 Mechanical clamping . . . 37
4.12 FSW process setup . . . 37
4.13 Sketch of the WC-Co FSW-tool . . . 38
4.14 Sintered tungsten carbide - cobalt FSW-tool . . . 38
4.15 Welding configuration . . . 39
4.16 Sampling setup . . . 39
4.17 Schematic sketch of a TEM sample . . . 44
4.18 Temperature profile during PWHT . . . 44

5.1 First FSW experiments . . . 46
5.2 Optimized FSW process . . . 46
5.3 Macrograph of a weld cross section after process optimization . . . 47
5.4 Overview of the used backing plates . . . 47
5.5 Influence of the revolutionpitch on the temperature distribution . . . 49
5.6 Peak temperatures plottet over revolutionpitches. $F_z = 19\,kN$ . . . 49
5.7 Influence of the revolutionpitch on the tensile properties . . . 51
5.8 Influence of the down force on the tensile properties . . . 52
5.9 Weld cross section. $Revpitch = 0.5\,mm\,rev^{-1}$, $F_z = 19\,kN$ . . . 53
5.10 Weld cross section. $Revpitch = 0.5\,mm\,rev^{-1}$, $F_z = 24\,kN$ . . . 53
5.11 Summary of the tensile properties of all parameter sets . . . 54
5.12 Matrix of welding parameters and revolutionpitches . . . 54
5.13 Tensile properties of an optimized joint compared to the parent material 55
5.14 Tensile test sample. (a) before testing; (b) fractured sample . . . 55
5.15 Systematic fracture behavior for different revolutionpitches . . . 55
5.16 Illustration of the hardness measurement approach . . . 56
5.17 Hardness profile across the weld seam for optimized parameters . . . 58
5.18 Hardness profiles in SUS420J2 for different heat input . . . 58
5.19 Low heat input weld optical macrograph . . . 60
5.20 SEM and EBSD images of weld defects in a low heat input weld . . . 60
5.21 Fractured tensile specimen of a low heat input weld . . . 61
5.22 Fracture surface in SZ of a low heat input weld . . . 61
5.23 Fracture path of a low heat input weld . . . 62
5.24 High heat input weld optical macrograph . . . 63
5.25 SEM and EBSD images of a high heat input weld . . . 63
5.26 Fractured tensile specimen of a high heat input weld . . . 64
5.27 Fracture surface in SZ of a high heat input weld . . . 65
5.28 Fracture path in SZ of a high heat input weld . . . 66
5.29 Optical macrograph of an optimized weld . . . 67
5.30 SEM images of the fully consolidated root . . . 67

5.31 EBSD images of the fully consolidated root 67
5.32 Microstructure characterization in PM 68
5.33 Microstructure characterization in HAZ 69
5.34 Comparison of EBSD images of SUS420J2 in PM and HAZ 70
5.35 Detailed EBSD images of SUS420J2 in PM and HAZ 70
5.36 Comparison of optical micrographs of SUS420J2 in PM and HAZ 71
5.37 TEM images of grain boundary precipitates in HAZ of an α-layer 72
5.38 High magnification TEM image of precipitates in HAZ of an α-layer . . . 73
5.39 Microstructure characterization in TMAZ close to HAZ 74
5.40 Microstructure characterization in TMAZ close to SZ 76
5.41 Illustration of the structural impairment in the weld center 77
5.42 EBSD images of SZ center 78
5.43 EBSD images of the interface between α and γ in SZ 79
5.44 Fractured tensile specimen of an optimized weld 80
5.45 Fracture surface in HAZ-RS of an optimized parameters weld 81
5.46 Fracture surface of the single layers 81
5.47 Fracture path in HAZ-RS of an optimized parameters weld 82
5.48 Hardness profile across the weld seam in as-welded and PWHT condition 83
5.49 Influence of the PWHT on the tensile properties 84
5.50 Fractured PWHT tensile specimen 86
5.51 Fracture behavior of a PWHT sample. Fracture occurred in PM 87
5.52 Fracture behavior of a PWHT sample. Fracture occurred in SZ 88
5.53 Microstructure in HAZ of an SUS301 layer with/without PWHT 90
5.54 Micrographs of HAZ of a SUS420J2 layer with/without PWHT 90
5.55 Microstructure in HAZ of a SUS420J2 layer with/without PWHT 90

List of Tables

3.1 Standard chemical composition of SUS301 [5] 10
3.2 Standard chemical composition of SUS420J2 [5] 13

4.1 Chemical composition of the constituent steels 31
4.2 Tensile properties of SUS301, SUS420J2 and multilayered steel 35
4.3 Welding parameters overview 40

5.1 Maximum temperatures at different revolutionpitches. $F_z = 19\,kN$ 48
5.2 Maximum temperatures at different forces. $Revpitch = 0.5\,mm\,rev^{-1}$ . . 50
5.3 Maximum temperatures at different forces. $Revpitch = 0.25\,mm\,rev^{-1}$ . . 50
5.4 Tensile properties in as-welded and PWHT condition 84

Bibliography

[1] J. R. Davis, ed., *ASM Specialty Handbook Stainless Steels*. Ohio, USA: ASM International, 1994.

[2] A. O'Brien and C. Guzman, eds., *Welding Handbook*. American Welding Society (AWS), 9 ed., 2011.

[3] J. C. Lippold and D. J. Kotecki, *Welding Metallurgy and Weldability of Stainless Steels*. Hoboken, New Jersey: John Wiley & Sons, Inc., 2005.

[4] H. K. D. H. Bhadeshia and R. W. K. Honeycombe, *Steels Microstructure and Properties*. Elsevier Ltd., 3 ed., 2006.

[5] *Key to steel*. Marbach, Germany: Verlag Stahlschlüssel Wegst GmbH, 22 ed., 2010.

[6] A. J. Sedriks, *Stress-Corrosion Cracking of Stainless Steels*, ch. 4 in Stress-Corrosion Cracking, pp. 91–130. Ohio, USA: ASM International, 1992.

[7] J. Davis, ed., *Alloy Digest Sourcebook: Stainless Steels*. Ohio, USA: ASM International, 2000.

[8] U. Krupp, C. West, and H.-J. Christ, "Deformation-induced martensite formation during cyclic deformation of metastable austenitic steel: Influence of temperature and carbon content," *Materials Science and Engineering A*, vol. 481-482, pp. 713–717, 2008.

[9] H. Shaikh, *Stress Corrosion Cracking of Austenitic Stainless Steel Weldments*, ch. 7 in Corrosion of Austenitic Stainless Steels, pp. 166–189. England: Woodhead Publishing Limited, 2002.

[10] R. W. Messler, *Principles of Welding*. John Wiley & Sons, Inc., 1999.

[11] "Böhler M330 VMR data sheet." http://www.bohler.at/deutsch/files/downloads/M330DE.pdf (retrieved: 2011-11-30).

[12] D. R. Lesuer, C. K. Syn, O. D. Sherby, J. Wadsworth, J. J. Lewandowski, and W. H. Hunt, "Mechanical behaviour of laminated metal composites," *International Materials Review*, vol. 41(5), pp. 169–197, 1996.

[13] C. K. Syn, D. R. Lesuer, J. Wolfenstein, and O. D. Sherby, "Layer thickness effect on ductile tensile fracture of ultrahigh carbon steel-brass laminates," *Metallurgical transactions A*, vol. 24A, pp. 1647–1653, 1993.

[14] F. Carreno, J. Chao, M. Pozuelo, and O. A. Ruano, "Microstructure and fracture properties of an ultrahigh carbon steel-mild steel laminated composite," *Scripta Materialia*, vol. 48(8), pp. 1135–1140, 2003.

[15] H. S. Liu, B. Zhang, and G. P. Zhang, "Microstructures and mechanical properties of Al/Mg alloy multilayered composites produced by accumulative roll bonding," *Journal of Materials Science and Technology*, vol. 27(1), pp. 15–21, 2011.

[16] J. Inoue, S. Nambu, Y. Ishimoto, and T. Koseki, "Fracture elongation of brittle/ductile multilayered steel composites with a strong interface," *Scripta Materialia*, vol. 59(10), pp. 1055–1058, 2008.

[17] S. Nambu, M. Michiuchi, Y. Ishimoto, K. Asakura, J. Inoue, and T. Koseki, "Transition in deformation behavior of martensitic steel during large deformation under uniaxial tensile loading," *Scripta Materialia*, vol. 60(4), pp. 221–224, 2009.

[18] S. Nambu, M. Michiuchi, J. Inoue, and T. Koseki, "Effect of interfacial bonding strength on tensile ductility of multilayered steel composites," *Composites Science and Technology*, vol. 69(11-12), pp. 1936–1941, 2009.

[19] P. Lhuissier, J. Inoue, and T. Koseki, "Strain field in a brittle/ductile multilayered steel composite," *Scripta Materialia*, vol. 64(10), pp. 970–973, 2011.

[20] L. Li, F. Yin, Y. Tanaka, S. Kishimoto, and K. Nagai, "Characteristics of the cold-rolling texture in a multi-layered material composed of SUS301 and SUS420J2 steels," *Materials Transactions*, vol. 51(5), pp. 911–917, 2010.

[21] M. A. Omar, *The Automotive Body Manufacturing Systems and Processes*. John Wiley & Sons, Inc., 2011.

[22] A. Mortensen and J. Llorca, "Metal matrix composites," *Annual review of materials research*, vol. 40, pp. 243–270, 2010.

[23] http://autospeed.com/cms/gallery/article.html?slideshow=0&a=109717&i=7 (retrieved: 2011-09-12).

[24] W. M. Thomas, E. D. Nicholas, J. C. Needham, M. G. Murch, P. Temple-Smith, and C. J. Dawes, "Friction stir butt welding," 1991. GB patent no. 9125978, International patent no. PCT/GB92/02203.

[25] R. Nandan, T. DebRoy, and H. K. D. H. Bhadeshia, "Recent advances in friction-stir welding - process, weldment structure and properties," *Progress in Materials Science*, vol. 53(7), pp. 980–1023, 2008.

[26] M. Fukumoto, T. Yasui, Y. Shimoda, M. Tsubaki, and T. Shinoda, "Butt welding between dissimilar metals by friction stirring," in 5^{th} *international symposium on friction stir welding*, (Metz, France), 2004.

[27] L. E. Murr, Y. Li, R. D. Flores, E. A. Trillo, and J. C. McClure, "Intercalation vortices and related microstructural features in the friction-stir welding of dissimilar metals," *Materials Research Innovations*, vol. 2(3), pp. 150–163, 1998.

[28] C. Schneider, T. Weinberger, J. Inoue, N. Enzinger, and T. Koseki, "Characterisation of interface of steel/magnesium FSW," *Science and Technology of Welding and Joining*, vol. 16(1), pp. 100–106, 2011.

[29] R. S. Mishra and Z. Y. Ma, "Friction stir welding and processing," *Materials Science and Engineering R*, vol. 50(1-2), pp. 1–78, 2005.

[30] R. S. Mishra and M. W. Mahoney, *Friction Stir Welding and Processing*. Ohio, USA: ASM International, 2007.

[31] W. M. Thomas, P. L. Threadgill, and E. D. Nicholas, "Feasibility of friction stir welding steel," *Science and Technology of Welding and Joining*, vol. 4 (6), pp. 365–372, 1999.

[32] P. L. Threadgill, "Terminology in friction stir welding," *Science and Technology of Welding and Joining*, vol. 12(4), pp. 357–360, 2007.

[33] M. Matsushita, Y. Kitani, R. Ikeda, M. Ono, H. Fujii, and Y.-D. Chung, "Development of friction stir welding of high strength steel sheet," *Science and Technology of Welding and Joining*, vol. 16(2), pp. 181–187, 2011.

[34] L. Dubourg, F.-O. Gagnon, F. Nadeau, L. St-Georges, and M. Jahazi, "Process window optimization for FSW of thin and thick sheet Al alloys using statistical methods," in 6^{th} *international symposium on friction stir welding*, (St Sauveur, Canada), 2006.

[35] T. Weinberger, N. Enzinger, and H. Cerjak, "Microstructural and mechanical characterisation of friction sitr welded 15-5 PH steel," *Science and Technology of Welding and Joining*, vol. 14(3), pp. 210–215, 2009.

[36] T. Weinberger, S. Khosa, B. Führer, and N. Enzinger, "Analysis of tool wear and failure mechanism during friction stir welding of steel," in 7^{th} *international symposium on friction stir welding*, (Awaji, Japan), 2008.

[37] M. P. Miles, T. W. Nelson, R. Steel, E. Olsen, and M. Gallagher, "Effect of friction stir welding conditions on properties and microstructures of high strength automotive steel," *Science and Technology of Welding and Joining*, vol. 14(3), pp. 228–232, 2009.

[38] A. P. Reynolds, W. Tang, T. Gnaupel-Herold, and H. Prask, "Strcture, properties, and residual stress of 304L stainless steel friciton stir welds," *Scripta Materialia*, vol. 48, pp. 1289–1294, 2003.

[39] C. B. Fuller, *Friction Stir Tooling: Tool Materials and Designs*, ch. 2 in Friction Stir Welding and Processing, pp. 7–35. Ohio, USA: ASM International, 2007.

[40] R. Rai, A. De, H. K. D. H. Bhadeshia, and T. DebRoy, "Review: friction stir welding tools," *Science and Technology of Welding and Joining*, vol. 16(4), pp. 325–341, 2011.

[41] A. Arora, A. De, and T. DebRoy, "Toward optimum friction stir welding tool shoulder diameter," *Scripta Materialia*, vol. 64(1), pp. 9–12, 2011.

[42] W. M. Thomas and E. D. Nicholas, "Friction stir welding for the transportation industries," *Materials & Design*, vol. 18(4-6), pp. 269–273, 1997.

[43] P. L. Threadgill, A. J. Leonard, H. R. Shercliff, and P. J. Withers, "Friction stir welding of aluminium alloys," *International Materials Reviews*, vol. 54(2), pp. 49–93, 2009.

[44] F. Marie, "Development of friction stir welding 7000 serie extrusions for central wing box application," in 3^{th} *international symposium on friction stir welding*, (Kobe, Japan), 2001.

[45] H. K. D. H. Bhadeshia and T. DebRoy, "Critical assessment: friction stir welding of steel," *Science and Technology of Welding and Joining*, vol. 14(3), pp. 193–196, 2009.

[46] W. J. Arbegast, *Application of Friction Stir Welding and Related Technologies*, ch. 13 in Friction Stir Welding and Processing, pp. 273–308. ASM International, 2007.

[47] S. Kou, *Welding Metallurgy*. Hoboken, New Jersey: John Wiley & Sons, Inc., 2. ed., 2003.

[48] C. Kolbeck, R. Pitonak, T. Weinberger, and R. Weissenbacher, "Reibrührschweißwerkzeug," June 2009. Patent AT 506 133 A1.

[49] "Metallic materials - tensile testing - part 1: Method of test at ambient temperature." EN 10002-1:2001.

[50] G. Petzow, *Metallographic etching*. Ohio, USA: Amercian society for metals, 1978.

[51] "MasterMet Colloidal Silica Suspension data sheet." http://www.buehler.com/productinfo/consumables/pdfs/FINAL_POLISHING.pdf (retrieved: 2011-09-17).

[52] O. Engler and V. Randle, *Introduction to Texture Analysis*. Taylor and Francis Group, 2. ed., 2010.

[53] V. Randle, *Electron Backscatter Diffraction in Materials Science*, ch. 2 in Electron Backscatter Diffraction in Materials Science, pp. 19–30. Kluwer Academic/Plenum Publisher, 2000.

[54] "Nicrofer 7126 data sheet." http://www.thyssenkrupp-vdm.com/fileadmin/Downloads/Datenblaetter/de/Nicrofer_7216_7216H_600_600H_d.pdf (retrieved: 2011-09-14).

[55] J.-H. Cho, D. E., and P. R. Dawson, "Modeling strain hardening and texture evolution in friction stir welding of stainless steel," *Materials Science and Engineering A*, vol. 398(1-2), pp. 146–163, 2005.

A. Friction Stir Butt Welding Tool

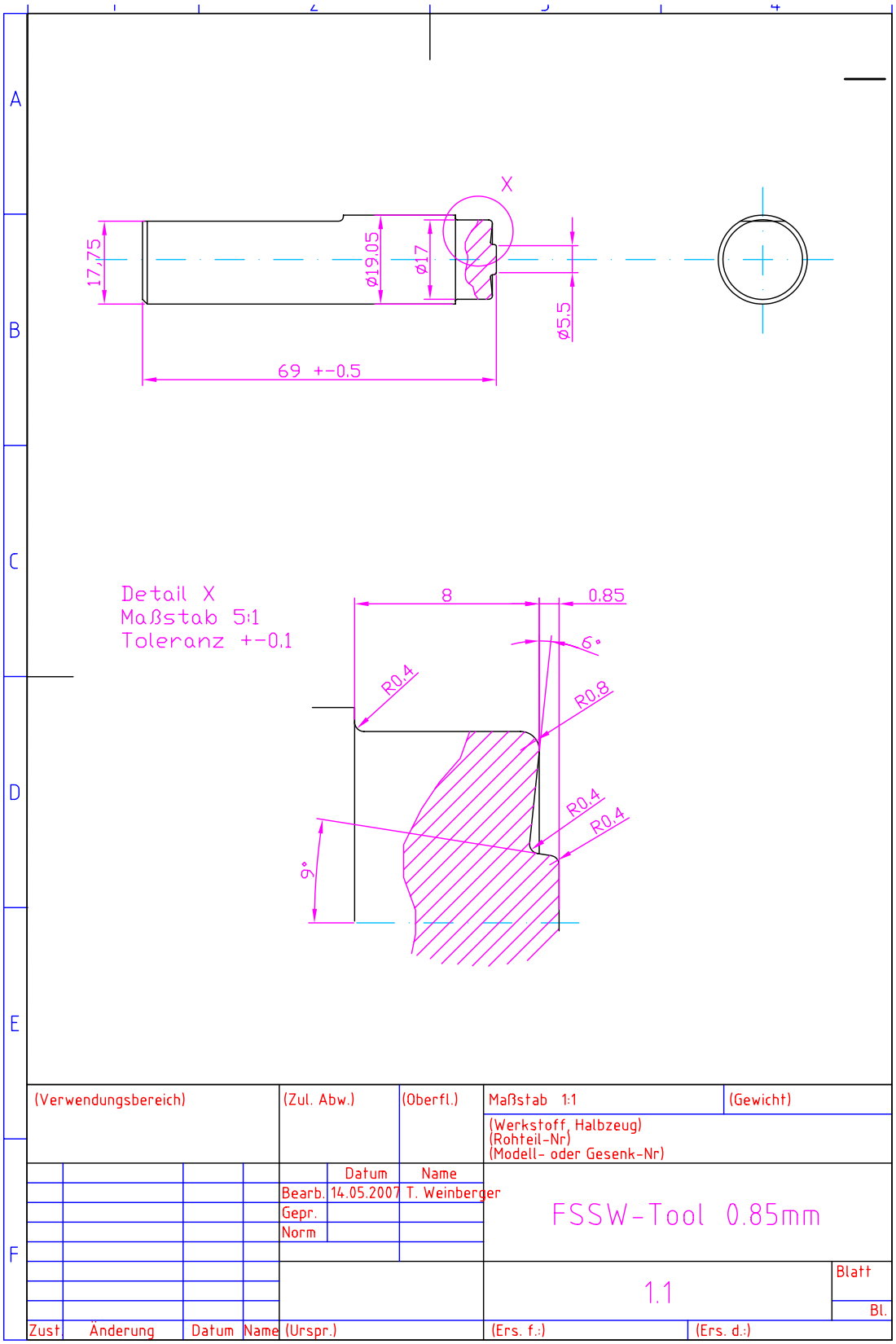

B. Overlap Welding Experiments

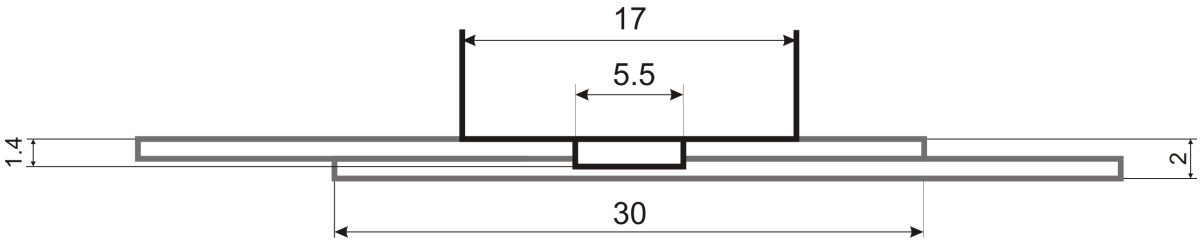

Overlap welding configuration

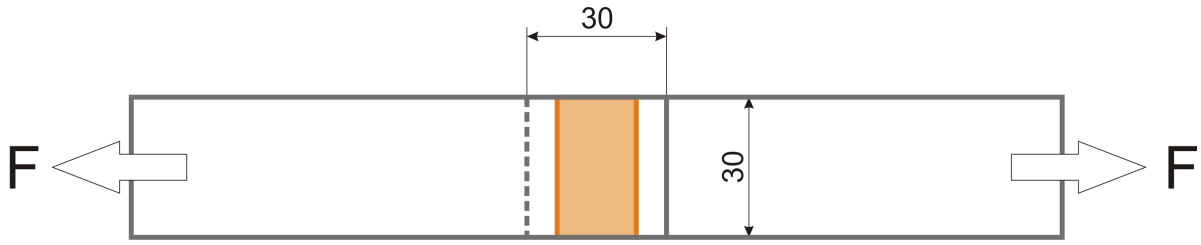

Overlap welding tensile test sample

Tilt angle [°]	Down Force [kN]	Spindle Speed [rpm]	Weld Speed [mm/min]
1.5	19	400	100 150
		550	100 150 200
	20	400	100 150 200

Summary of overlap welding parameters

C. Results of Tensile Tests of Overlap Welds

F_z $[kN]$	Spindle Speed $[rpm]$	Weld Speed $[mm/min]$	No.	Max. Force $[kN]$
19	400	100	I II III	38.2* 38.2* 38.1*
19	400	150	I II III	34.8 x x
19	550	100	I II III	36.7 37.5 37.7
19	550	150	I II III	35.8 37.9 37.8
19	550	200	I II III	35.6 39 38.8*
19	800	200	I II III	36.6 36 36.2
19	800	300	I II III	36.5 33.8* 33*
20	400	100	I II III	36 37.6 37.6
20	400	150	I II III	36.9 37 36.7
20	400	200	I II III	34.7 36.4 30.5

* invalid experiment, x sample not fractured